

MOLECULAR GAS IN NEARBY GALAXIES

MOLECULAR GAS IN NEARBY GALAXIES: STAR FORMATION,
MOLECULAR GAS AND HEATING IN THE ANTENNAE

By

MAXIMILIEN R. P. SCHIRM, B.Sc.

A Thesis

Submitted to the School of Graduate Studies

in Partial Fulfilment of the Requirements

for the Degree

Master of Science

McMaster University

©Copyright by Maximilien Schirm, September 2011

MASTER OF SCIENCE (2011)

McMaster University

(Physics and Astronomy)

Hamilton, Ontario

TITLE: Molecular Gas in Nearby Galaxies: Star Formation, Molecular Gas and Heating in the Antennae

AUTHOR: Maximilien Schirm, B.Sc. (University of Waterloo)

SUPERVISOR: Christine Wilson

NUMBER OF PAGES: xvii, 123

Abstract

The study of ongoing mergers is vital to understanding how intense star bursts are triggered, and how luminous infrared galaxies and ultra luminous infrared galaxies are formed. The Antennae (NGC 4038/39), at a distance of only 24.9 Mpc, represents the nearest example of a major merger between two gas rich spirals and provides us with a unique laboratory for studying molecular gas and star formation. I have obtained two fully sampled observations of the Antennae using the *Herschel* SPIRE Fourier Transform Spectrometer which I have supplemented with JCMT CO $J = 3 - 2$ observations. I detect CO, CI and NII emission throughout both the overlap region and the nucleus of NGC 4038. I measured the integrated intensity of the CO $J = 4 - 3$ to $8 - 7$ and find that the overlap region is brighter for all but the $J = 4 - 3$ line. I find that, in the nucleus of NGC 4038, the CO spectral line energy distribution peaks at the $4 - 3$ transition, while in the overlap region it peaks at the $3 - 2$ transition. I modelled the CO emission using the non-local thermal equilibrium radiative transfer code RADEX coupled with a Bayesian likelihood code. I find a warm ($T_{kin} > 600$ K) lower density ($n_{H_2} \sim 200 \text{ cm}^{-3}$) component of molecular gas in the nucleus of NGC 4038, and similarly in the overlap region ($T_{kin} > 600$ K, $n_{H_2} \sim 300 \text{ cm}^{-3}$) and find widespread evidence for multiple components of molecular gas throughout the system. These warm components in both regions correspond to $\lesssim 1\%$ of the total molecular gas. I find no evidence of x-ray dominated regions, cosmic rays or turbulent heating being the primary source of heating throughout the galaxy, while photodissociation regions or supernova and stellar winds *may* be the primary source of heating throughout the galaxy.

Acknowledgements

This thesis would not have been possible without the support and guidance of numerous individuals. In this section, I will do my best to acknowledge all those who contributed in either a direct or indirect manner. I apologize in advance to those who I have forgotten to acknowledge here.

I would first like to express my sincerest gratitude to Dr. Christine Wilson for providing me with this unique and amazing opportunity. She has been, and continues to be, a vast source of wisdom, knowledge, motivation, support and guidance throughout the past 2 years. Without her, I would never have discovered the amazing field of submillimeter astronomy, nor would I have ever had the opportunity to work with data from some of the most exciting millimetre and submillimeter instruments, including the Hershel SPIRE FTS.

I would also like to thank my committee members, Alison Sills and Dough Welch, for the numerous comments and the constructive criticism of this thesis.

I would also like to extend my gratitude to my collaborators in the Very Nearby Galaxy Survey, along with the entire SAG2 for accepting me as a member and for allowing me to use the FTS data to work on the Antennae. I would especially like to thank from this group Jason Glenn, Naseem Rangwala and Julia Kamenetzky.

I must also thank the ZSpec team for providing me with the likelihood code used throughout this thesis, and Phil Maloney for allowing me to use his version of RADEX. Particularly, this work would not have been possible without the help of Julia Kamenetzky, who provided me with the necessary help required to use both the likelihood code and Phil's version of RADEX.

The data reduction would not have been possible without Peter Imhof, Trevor Fulton, and the entire SPIRE ICC. The entire SPIRE ICC has been working tirelessly on not only optimizing and improving the data reduction process, but also on understanding the calibration of the SPIRE FTS.

I would like to recognize the support of my family. More specifically, I wish to thank my parents, Ron and Johanne Schirm, for not only their support throughout the past 2 years, but throughout my entire academic career. My appreciation towards my family does not end there, as my brother, sister, brother-in-law and Oma were all incredibly understanding throughout the past two years. I must thank my nephew for providing me with a distraction when a break was necessary, and for providing me with numerous "corrections", even though none of them remain in this final copy. Along with my family, I also need to thank Jenna Voisin for not only the support, but also for listening to me talk about my research, as boring as it must have been for her at times.

Finally, I would like to thank Christine's other students, namely Kazimierz Sliwa, Tara Parkin, and Jennifer Golding, for the numerous engaging discussions throughout the past 2 years, both research and non-research related.

To Karl Schirm

Table of Contents

Descriptive Notes	ii
Abstract	iii
Acknowledgements	iv
List of Figures	xi
List of Tables	xvii
Chapter 1 Introduction	1
1.1 Luminous Infrared Galaxies	3
1.2 NGC 4038/39	6
1.3 Radiative Transfer Models	10
1.3.1 Radiative transfer models in NGC4038/39	11
1.4 Herschel Space Observatory	12
1.5 Summary	14
Chapter 2 Data and Data Reduction	18
2.1 Observations	18
2.2 CO Integrated Intensity Maps	19
2.2.1 FTS beam correction	28
2.2.2 Jy/beam km/s to K km/s conversion	28
2.3 JCMT CO $J = 3 - 2$ Map	29

Chapter 3	Non-Local Thermal Equilibrium Analysis (RADEX)	36
3.1	RADEX	36
3.2	Likelihood analysis	37
3.2.1	Priors	38
3.3	Results	39
Chapter 4	Discussion	49
4.1	Line intensity maps	49
4.2	Radiative transfer analysis	50
4.3	Heating mechanism	52
4.3.1	X-ray dominated regions	53
4.3.2	Photodissociation regions	54
4.3.3	Cosmic rays	55
4.3.4	Mechanical heating	56
Chapter 5	Conclusion and Future Work	59
5.1	Conclusions	59
5.2	Future Work	62
Chapter A	Data Reduction	64
A.1	User defined parameters	65
A.2	Load observation context	65

A.3	Load calibration and auxiliary products	66
A.4	Process Level 0.5 observation	66
A.4.1	First level deglitching	67
A.4.2	Non-linearity and temperature drift correction	68
A.4.3	Clipping correction	69
A.4.4	Time domain phase correction	69
A.4.5	Add pointing information	70
A.4.6	Create interferogram	71
A.5	Process Level 1 Interferogram	72
A.5.1	Adjust optical path difference ranges	72
A.5.2	Interferogram baseline correction	72
A.5.3	Second level deglitching	75
A.5.4	Interferogram Phase Correction	77
A.6	Process Level 1 Spectra	79
A.6.1	Removal of out of band data	79
A.6.2	Correcting for instrument emission	81
A.6.3	Applying the extended source flux conversion	82
A.6.4	Removal of telescope emission	82
A.7	Level 2 Maps	83
A.7.1	Point source calibration	86

A.7.2	Level 2 map creation	87
A.7.3	Point source correction and level 2 map script	88
Chapter B Line Fitting		96
B.1	Description	96
B.2	Script	99

List of Figures

1.1	Hubble Space Telescope true-colour image of the Antennae (Credit: Brad Whitmore (STScI) and NASA) with the nuclei of NGC 4038 and NGC 4039, along with the overlap region and western loop labelled.	7
1.2	Arrangement of the bolometric array for the SLW (<i>top</i>) and SSW (<i>bottom</i>) (SPI, 2011c). The unvignetted detectors are those found within the red circles, (7 for the SLW, 19 for the SSW), and are the detectors used for science. In addition, 2 of the detectors in the SSW (F4 and D5) are dead and are no longer used for science.	15
1.3	Plot demonstrating the varying beam sizes of the SLW (<i>left</i>) and SSW (<i>right</i>) from Swinyard et al. (2010). Notice that the size of the SSW beam varies considerably less than that of the SLW beam.	16
2.1	Slice of the SLW data cube at ~ 458.7 GHz. The red box identifies the pixel representing the nucleus of NGC 4038, while the blue box identifies the pixel representing the overlap region. . . .	20
2.2	SLW spectrum for brightest region of nucleus of NGC 4038 corresponding to the red box in Figure 2.1. I have identified 5 CO lines and both [CI] lines. There are still lines to be identified in this spectrum.	21

2.3	SLW spectrum for brightest region of the overlap region corresponding to the blue box in Figure 2.1. I have identified 5 CO lines and both [CI] lines. There are still lines to be identified in this spectrum.	22
2.4	Slice of the SSW data cube at ~ 1453.4 GHz. The red box identifies the pixel representing the nucleus of NGC 4038, while the blue box identifies the pixel representing the overlap region.	23
2.5	SSW spectrum for brightest region of nucleus of NGC 4038 corresponding to the red box in Figure 2.4. Only the [NII] line at ~ 1460 GHz has been identified so far; however there are numerous potential candidates for other lines throughout the spectrum.	24
2.6	SSW spectrum for brightest region of the overlap region corresponding to the blue box in Figure 2.4. Only the [NII] line at ~ 1460 GHz has been identified so far; however there are numerous potential candidates for other lines throughout the spectrum.	25
2.7	Line fits for the nucleus of NGC 4038 (<i>left</i>) and overlap region (<i>right</i>). The fits are for the (from top to bottom) the $J = 4 - 3$ transition, the CO $J = 7 - 6$ and [CI] $J = 2 - 1$ doublet, and the CO $J = 8 - 7$ transition.	27
2.8	Integrated intensity map for CO $J = 4 - 3$ in units of K km/s.	30
2.9	Integrated intensity map for CO $J = 5 - 4$ in units of K km/s.	31

2.10	Integrated intensity map for CO $J = 6 - 5$ in units of K km/s. . .	32
2.11	Integrated intensity map for CO $J = 7 - 6$ in units of K km/s. . .	33
2.12	Integrated intensity map for CO $J = 8 - 7$ in units of K km/s. . .	34
2.13	Integrated intensity map for CO $J = 4 - 3$ in units of K km/s. Note that the Declination is on the x-axis, and the Right Ascension is on the y-axis.	35
3.1	CO spectral line energy distributions for nucleus of NGC 4038 (<i>top</i>) and overlap region (<i>bottom</i>). The calculations were performed with the CO $J = 4 - 3$ to $8 - 7$ lines (<i>left</i>) and the CO $J = 3 - 2$ to $8 - 7$ lines (<i>right</i>). The solid red line is the CO SLED as calculated by RADEX from the 1DMax parameters, while the blue dashed line is as calculated by RADEX from the 4DMax parameters. The 4DMax solution provides a superior fit as it accounts for the degeneracy of $N(\text{CO})$ and Φ_A	43
3.2	Normalized likelihood distributions for the nucleus of NGC 4038 for the kinetic temperature (<i>top left</i>), gas density (<i>top right</i>), CO column density (<i>bottom left</i>) and source filling factor (<i>bottom</i> <i>right</i>). The CO emission lines measured from the FTS SLW and the JCMT ($J = 3 - 2$ to $8 - 7$) were included in these calculations.	44

3.3	Normalized likelihood distributions for the overlap region of the Antennae for the kinetic temperature (<i>top left</i>), gas density (<i>top right</i>), CO column density (<i>bottom left</i>) and source filling factor (<i>bottom right</i>). The CO emission lines measured from the FTS SLW and the JCMT ($J = 3 - 2$ to $8 - 7$) were included in these calculations.	45
-----	--	----

3.4	Normalized 1-D (<i>right</i>) and 2-D (<i>left</i>) likelihood distributions for the nucleus of NGC 4038. The 2-D contour plots are for the kinetic temperature and gas density (<i>top left</i>), and filling factor and CO column density (<i>bottom left</i>). The 1-D distributions are for the pressure (<i>top right</i>) and beam average column density (<i>bottom right</i>). The dotted lines in the 2-D contour plots correspond to the pressure (<i>top left</i>) and the beam average column density (<i>bottom left</i>). The CO emission lines measured from the FTS SLW and the JCMT ($J = 3 - 2$ to $8 - 7$) were included in these calculations.	46
-----	--	----

3.5	Normalized 1-D (<i>right</i>) and 2-D (<i>left</i>) likelihood distributions for the overlap region. The 2-D contour plots are for the kinetic temperature and gas density (<i>top left</i>), and filling factor and CO column density (<i>bottom left</i>). The 1-D distributions are for the pressure (<i>top right</i>) and beam average column density (<i>bottom right</i>). The dotted lines in the 2-D contour plots correspond to the pressure (<i>top left</i>) and the beam average column density (<i>bottom left</i>). The CO emission lines measured from the FTS SLW and the JCMT ($J = 3 - 2$ to $8 - 7$) were included in these calculations.	47
-----	---	----

A.1	Example interferogram taken from the reduction of the observation of the nucleus of NGC 4038. This interferogram has had no corrections applied to it. Note that the centre burst is not located in the centre of the interferogram, and that the baseline is non-zero.	73
-----	---	----

A.2	Zoom in around centre burst of the same interferogram in figure A.1.	74
-----	--	----

A.3	Spectrometer Detector Interferogram before (<i>blue line</i>) and after (<i>red line</i>) interferogram baseline correction. The interferograms are from the reduction of the nucleus of NGC 4038.	76
-----	--	----

A.4	Zoom in on centre burst of Spectrometer Detector Interferogram before (<i>blue line</i>) and after (<i>red line</i>) interferogram phase correction. The interferograms are from the reduction of the nucleus of NGC 4038. Notice that in this particular case, very little phase correction is required.	78
A.5	Example of an initial level 1 unapodized spectra. This spectrometer detector spectrum has not yet had any corrections applied. Notice that the spectrum extends far beyond the bandwidth of the SLW (14.6 cm to 33.3 cm)	80
A.6	SDS prior to the removal of the telescope emission. Most of the signal is the blackbody emission from the telescopes primary mirror.	84
A.7	Representative final level 1 spectrum from the reduction of the nucleus of NGC 4038 after subtraction of the telescope emission.	85

List of Tables

3.1	Parameters used to calculate priors	40
3.2	RADEX model grid parameters	40
3.3	Measured line intensities and measurement uncertainties	41
3.4	Nucleus of NGC 4038: CO $J = 4 - 3$ to $8 - 7$	48
3.5	Nucleus of NGC 4038: CO $J = 3 - 2$ to $8 - 7$	48
3.6	Overlap region: CO $J = 4 - 3$ to $8 - 7$	48
3.7	Overlap region: CO $J = 3 - 2$ to $8 - 7$	48
A.1	Co-aligned detectors	86

Chapter 1

Introduction

Galaxies come in all shapes and sizes, from the smallest companion dwarf galaxy to the largest brightest cluster galaxy. While the physical characteristics from galaxy type to galaxy type can vary considerably, all galaxies are comprised of the same major ingredients in varying quantities: stars, gas, dust and dark matter. Three of these four ingredients can be broken down further into their varying types and classifications. Stars are typically classified by their luminosity and temperature, from the dim, cool M stars to the bright, hot O stars. Dust, on the other hand, is characterized by its temperature, varying from cool dust (~ 20 K) to warm and hot dust (~ 45 K) (Calzetti et al., 2000). Finally, there is the gas, which comes in three states: ionized, atomic and molecular.

The molecular gas provides the primary fuel for star formation (Young & Scoville, 1991), with the majority of star formation occurring in giant molecular clouds (GMCs, Solomon et al. 1979). Studying molecular gas is fundamental to understanding star formation in all galaxies, along with the overall evolution of the galaxy (Young & Scoville, 1991). Molecular gas consists primarily of H_2 , which is difficult to observe directly because it emits its electric

quadrupole rotational transitions in the infrared (Young & Scoville, 1991). We can, however, observe the molecular gas via the molecular gas tracers such as CO (Young & Scoville, 1991) and [CI] (Papadopoulos et al., 2004), and in dense molecular gas ($n(\text{H}_2) \geq 10^4 \text{ cm}^{-3}$), HCN (Papadopoulos, 2007) and HCO^+ (Graciá-Carpio et al., 2006). Many of these tracers are excited by collisions with H_2 , and the molecular abundance of the tracer is required to calculate the total molecular gas mass. Both CO and [CI] emit primarily in the submillimeter wavelength range; unfortunately, atmospheric interference makes it very difficult to observe a larger portion of the submillimeter range using ground based instrumentation. Of the CO rotational transitions, only the $J = 1 - 0$, $J = 2 - 1$, $J = 3 - 2$, $J = 4 - 3$, $J = 6 - 5$ and $J = 7 - 6$ (e.g see Papadopoulos et al. 2010 or Ward et al. 2003) transitions have been observed from the ground in nearby galaxies and few galaxies have been observed above $J = 3 - 2$. Even with these limited transitions, studying physical properties of cold molecular regions in nearby galaxies has been possible through radiative transfer modelling of CO (e.g. see Ward et al. 2003 or Bayet et al. 2006).

The star formation rate (SFR) is the rate at which molecular gas is converted into stars. In GMCs, the SFR can be determined by the infrared (IR) emission from warm dust heated by the embedded OB stars (Mooney & Solomon, 1988). $\text{H}\alpha$ and UV emission also both trace the SFR; $\text{H}\alpha$ emission results from recombination in ionized regions produced by young, massive stars, while the photospheres of O and B stars emit primarily in the UV range (Lee et al., 2009). A different measure of star formation in galaxies is the Star Formation Efficiency (SFE), which is defined as the SFR divide by the molecular, or in some cases the total or [HI], gas mass (Leroy et al., 2008). It provides

a measure of how rapidly the total molecular gas is being converted into stars. In GMCs and on larger scales in galaxies, the SFE is typically measured via either $L_{\text{IR}}/L_{\text{CO}}$ (Gao & Solomon, 2004) or $L_{\text{IR}}/L_{\text{HCN}}$ (Graciá-Carpio et al., 2008).

A power-law relation exists between the SFR and total gas mass known as the Kennicutt-Schmidt (KS) law (Kennicutt, 1998). In galaxies, the KS law is a simple relation between the IR luminosity and CO $J = 1 - 0$ luminosity: $L_{\text{IR}} \propto L_{\text{CO}}^{1.4-1.7}$ (Gao & Solomon, 2004). This suggests that the SFE scales as $L_{\text{CO}}^{0.4-0.7}$. In dense gas, assuming a KS law $L_{\text{IR}} = L_{\text{HCN}}^N$, the value of N is dependent upon the IR luminosity (Graciá-Carpio et al., 2008). The relation varies from $N \sim 0.80 - 0.95$ in normal galaxies to $N \sim 1.1 - 1.2$ in IR bright galaxies ($L_{\text{FIR}} > 10^{11} L_{\odot}$), indicating a higher SFE in the IR bright galaxies. Since IR-pumping can enhance HCN emission in IR-bright galaxies (Carroll & Goldsmith, 1981), the value of N , and consequently the SFE, may even be higher in these types of galaxies.

1.1 Luminous Infrared Galaxies

Luminous Infrared Galaxies (LIRGs) are a class of galaxies which emit most of their energy at infrared wavelengths ($L_{\text{IR}} > 10^{11} L_{\odot}$) (Sanders & Mirabel, 1996) while Ultra-Luminous Infrared Galaxies (ULIRGs) emit even more energy in the infrared ($L_{\text{IR}} > 10^{12} L_{\odot}$) (Sanders & Mirabel, 1996). This increased IR emission originates from dust heated by enhanced star formation activity in the galaxy (Cluver et al., 2010). Furthermore, both LIRGs and ULIRGs show enhanced star formation efficiency (SFE), defined as $L_{\text{IR}}/L_{\text{CO}}$ or, in the

case of dense gas, L_{IR}/L_{HCN} . In LIRGs, the SFE can be enhanced by up to $\sim 2 - 3$ times that of normal galaxies (Graciá-Carpio et al., 2008), while in ULIRGs it is even greater, up to $\sim 4 - 10$ times or more that of normal galaxies (Genzel et al., 2010), up to a maximum value of $\sim 500L_{\odot}/M_{\odot}$ (Papadopoulos et al., 2010). Furthermore, the HCN-to-CO fraction is significantly higher in ULIRGs than in other galaxies, indicating a higher dense molecular gas fraction (Solomon et al., 1992).

The enhanced SFR and SFE is typically seen in the form of "starbursts" in GMCs throughout the LIRG (Sanders & Mirabel, 1996). These starbursts are short, violent periods of star formation lasting typically on the order of ~ 10 Myr (Meurer, 2000) and are likely triggered by strong gravitational interactions or mergers (Hibbard, 1997). In the case of mergers, this is caused by the redistribution of material throughout the two merging galaxies (Toomre & Toomre, 1972), leading to reservoirs of molecular gas ideal for star formation. Joseph & Wright (1985) suggest that all merging galaxies undergo a period of "super starbursts", where $\gtrsim 10^9 M_{\odot}$ of stars are formed in bursts of $\sim 10^8$ years (Gehrz et al., 1983).

LIRGs with $L_{IR} > 3 \times 10^{11} L_{\odot}$ are almost exclusively found to be the product of merging galaxies (Hibbard, 1997), while almost all ULIRGs are found to be systems of galaxies in an advanced merging state (Sanders & Mirabel, 1996; Rangwala et al., 2011). Studies of the molecular gas in these galaxies provide information on ongoing and recent star formation, but do not tell the whole story of how the SFR and SFE are enhanced. Study of ongoing

mergers is vital to understanding the history of ULIRGs and LIRGs, and more specifically of the molecular gas and star formation in these galaxies.

Ongoing galactic mergers are a peculiar type of object. While each nucleus is observationally distinguishable and, especially in early mergers, retains characteristics of the original galaxy, mergers tend to show extended tidal features due to gravitational interactions between the merging galaxies (Toomre & Toomre, 1972). These same gravitational interactions cause the molecular gas to be compressed, which culminates in enhanced star formation (Hibbard, 1997). This enhanced star formation is representative of the incredible starbursts observed throughout merging systems (Larson & Tinsley, 1978; Cutri & McAlary, 1985; Hibbard, 1997), which may culminate in the aforementioned super starbursts in the denser regions of molecular gas (Joseph & Wright, 1985).

Mergers, therefore, are a very unique laboratory for studying star formation, and how star formation and starbursts are triggered in interacting systems. In fact, understanding how starbursts are triggered in merging galaxies is paramount to our understanding of similar events in all galaxies, including LIRGs, ULIRGs and starburst galaxies (Zhang et al., 2010). Beyond starbursts, if we are to believe the hierarchical evolution of galaxies (Steinmetz & Navarro, 2002), the study of ongoing mergers is necessary for understanding the overall evolution of galaxies, from the youngest of spirals to the oldest of ellipticals.

1.2 NGC 4038/39

The Antennae (NGC 4038/39, Arp 244) was first discovered by Herschel (1785). At a distance of only 24.9 Mpc (Mould et al., 2000) the Antennae represents the nearest example of a major merger between two gas rich spirals. It may also be the youngest known example of such a merger (Gao et al., 2001), and thus provides us with a unique opportunity to study star formation and molecular gas in early mergers. While having an FIR luminosity of $\sim 10^{11} M_{\odot}$, it is likely that the Antennae will eventually culminate in a ULIRG (Gao et al., 2001; Schulz et al., 2007). Its name comes from the long tidal tails caused by strong tidal interactions between the two galaxies. Early observations of the system detailed its incredibly complex structure (Duncan, 1923; Perrine, 1922), characterized primarily by its 3 brightest regions: the nuclei of NGC 4038 and NGC 4039, respectively, along with a third aptly named "overlap" region (Stanford et al., 1990), where the galactic disks are believed to overlap. Beyond these three bright regions, there is a fourth region near the nucleus of NGC 4038 known as the "western loop" (see Figure 1.1). Interestingly, the peak emission in all of the CO, mid-infrared (MIR), far-infrared (FIR), submillimeter, and radio 6 and 20 cm continuum occurs in the overlap region (Zhu et al., 2003), suggesting that the bulk of the star formation activity is occurring there.

Stars and star clusters are found throughout the Antennae, with most of the clusters being found in the two nuclei, the overlap region and the western loop (Whitmore & Schweizer, 1995; Whitmore et al., 1999). In total, there are between 800 and 8000 young star clusters throughout the Antennae, with

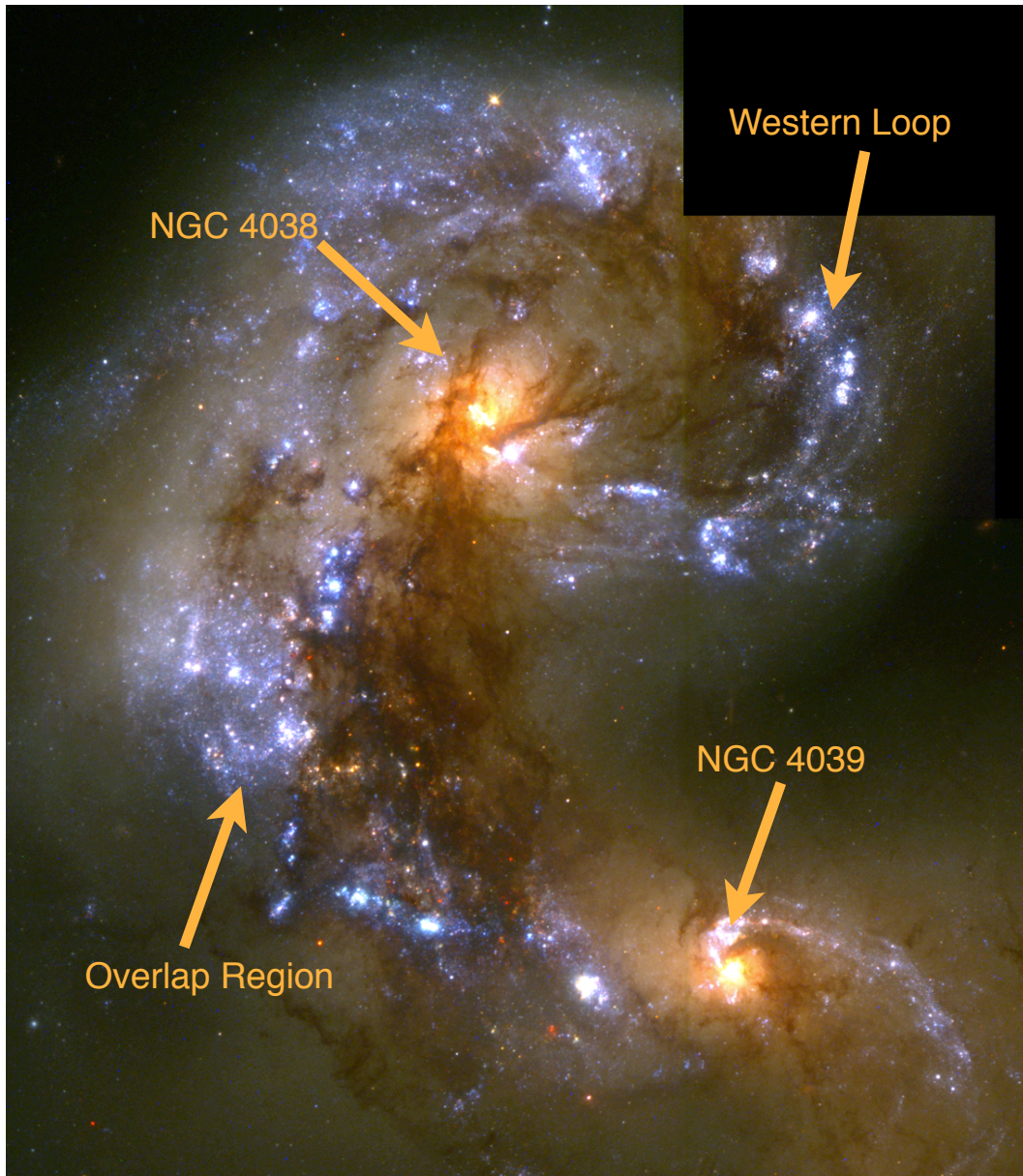


Figure 1.1: Hubble Space Telescope true-colour image of the Antennae (Credit: Brad Whitmore (STScI) and NASA) with the nuclei of NGC 4038 and NGC 4039, along with the overlap region and western loop labelled.

the youngest of these clusters ($\lesssim 5$ Myr) located in the "overlap" region, indicating ongoing star formation. Another young population of star clusters (5 – 10 Myr) exists in the western loop, with a more intermediate age population (~ 100 Myr) in a region north of the "overlap" region and east of NGC 4038. All of these populations are younger than those found in both nuclei, suggesting that there is no significant ongoing star cluster formation in these two regions.

Zhang et al. (2010) delved deeper into the star formation history of the Antennae by including high resolution *Spitzer* $24\ \mu\text{m}$ dust emission data with previous GALEX, HST and 2MASS images, ranging from the far-ultraviolet (FUV) to the $24\ \mu\text{m}$ emission. They compared the broadband spectral energy distributions (SEDs) for various star forming regions throughout the merging disks, confirming the results of Gao et al. (2001), that the star formation peaks in the "overlap" region and the western loop, with the western loop exhibiting characteristics of later stages of star formation than the overlap region. The most intense star formation is, however, occurring in the overlap region, heavily obscured by dust (Mirabel et al., 1998).

The molecular gas in the Antennae has been studied extensively via both interferometric (Stanford et al., 1990; Wilson et al., 2000, 2003; Petitpas et al., 2007) and single dish (Gao et al., 2001; Zhu et al., 2003; Bayet et al., 2006; Schulz et al., 2007) observations of various CO transitions. The high resolution of the interferometric CO $J = 1 - 0$ data allow individual molecular complexes to be identified across the entire merging system. While the bulk of the molecular gas found outside the two nuclei is located in 5 Super Giant

Molecular Complexes (SGMCs) in the overlap region (Wilson et al., 2000), there are an additional ~ 100 SGMCs scattered throughout the entire system (Wilson et al., 2003). While the interferometric maps are at very high resolution, they are unable to recover all of the CO flux, and are unsuitable for radiative transfer modelling. They do, however, provide detail observations of the distribution of molecular gas throughout the galaxy. The 5 SGMCs in the overlap region have a total molecular mass of $\sim 1.8 \times 10^9 M_{\odot}$, as opposed to the SGMCs in the nucleus of NGC 4038 ($\sim 1.5 \times 10^9 M_{\odot}$) and NGC 4039 ($\sim 5.0 \times 10^8 M_{\odot}$). Therefore most of the star forming fuel is found in the overlap region, correlating well with the observations of young star clusters.

While interferometric maps do well to map the GMCs throughout the system, it is the single dish observations which allow us to measure the total CO flux. Single dish observations of ^{12}CO have been performed for the $J = 1 - 0$ (Gao et al., 2001; Zhu et al., 2003; Schulz et al., 2007), $J = 2 - 1$ (Bayet et al., 2006; Schulz et al., 2007), $J = 3 - 2$ (Zhu et al., 2003; Bayet et al., 2006; Schulz et al., 2007), $J = 4 - 3$ (Bayet et al., 2006), $J = 6 - 5$ (Bayet et al., 2006) and $J = 7 - 6$ (Bayet et al., 2006) transitions, while the much weaker emitting isotopologue ^{13}CO has been observed in the $J = 2 - 1$ (Zhu et al., 2003) and $J = 3 - 2$ (Zhu et al., 2003; Bayet et al., 2006) transitions. Using $J = 1 - 0$ data, Gao et al. (2001) determined that the total molecular gas in the galaxy is $1.5 \times 10^{10} M_{\odot}$, leading to a relatively low global SFE of $4.2 L_{\odot}/M_{\odot}$. Zhu et al. (2003), using CO $J = 1 - 0$ from the Nobeyama 45 m single-dish map, determined that the overlap region itself yields a molecular gas mass of $\sim 4 \times 10^9 M_{\odot}$, more than twice the amount determined by the interferometric maps.

1.3 Radiative Transfer Models

Radiative transfer modelling of spectral lines is a powerful tool for determining the physical and chemical characteristics of molecular gas (e.g. see van der Tak et al. 2007). This modelling is typically performed in conjunction with single dish observations of various molecular species as the entire flux is recovered in these observations (e.g. see Zhu et al. 2003 or Bayet et al. 2006). While various different radiative transfer models exist, we use the publicly available non-local thermal equilibrium (LTE) radiative transfer code RADEX from van der Tak et al. (2007) to model various molecular emission lines, such as those of the CO ladder (e.g. see Ward et al. 2003, Panuzzo et al. 2010, Rangwala et al. 2011). RADEX only requires 3 inputs: the kinetic temperature (T_{kin}), the molecular gas density (n_{H_2}) and the column density of the molecular tracer, in our case CO ($N(CO)$). For each set of inputs, the code will output fluxes for each CO transition, along with the corresponding optical depth.

While radiative transfer analysis is possible with only a few (~ 4) ^{12}CO and/or ^{13}CO transitions (e.g. see Zhu et al. 2003), a more statistically realistic solution is possible with more CO transitions (≥ 5). By coupling RADEX with a likelihood code, it is possible to statistically determine the most likely physical parameters of a molecular region (Ward et al., 2003; Panuzzo et al., 2010; Naylor et al., 2010a). Ground based RADEX models are limited by the atmospheric opacity to a few CO transitions. While the $J = 1 - 0$, $J = 2 - 1$ and $J = 3 - 2$ are readily available via ground based instruments, the $J = 4 - 3$, $J = 6 - 5$ and $J = 7 - 6$ transitions are partially blocked by the atmosphere and as such difficult to observe (e.g. see Harris et al. 1991, Ward et al. 2003 or

Mao et al. 2000a). Many previous radiative transfer models were limited to the lower CO transitions, typically coupled with transitions of the isotopologue ^{13}CO (e.g. Zhu et al. 2003). In nearby CO bright galaxies, such as the starburst galaxy M82, in which the $J = 6 - 5$ and $J = 7 - 6$ transitions are observable with ground based instruments, a much more complete likelihood analysis is possible (Ward et al., 2003). While it is possible to perform a likelihood analysis with only the lower transitions, including the higher J CO lines can help identify to multiple components of molecular gas, such as cold, warm and hot components of molecular gas, along with the physical state of these components (e.g. see Panuzzo et al. 2010). Furthermore, by studying the warm molecular gas, we can further understand the necessary mechanisms necessary to heat the molecular gas (e.g. see Rangwala et al. 2011).

1.3.1 Radiative transfer models in NGC4038/39

By combining observations of ^{12}CO $J = 1 - 0$ and $J = 3 - 2$ emission lines with ^{13}CO $J = 2 - 1$ and $J = 3 - 2$ emission lines, Zhu et al. (2003) modelled the ratios of the CO lines using a Large Velocity Gradient (LVG) radiative transfer model in the two nuclei and in 3 positions of the overlap region where all 4 lines were detected. Even with their limited line sample, Zhu et al. (2003) find that there are likely two components across the galaxy. In the overlap region, this corresponds to a low-density ($n(\text{H}_2) \sim 3 \times 10^3 \text{ cm}^{-3}$) component, and a higher density ($n(\text{H}_2) \gtrsim 1 \times 10^4 \text{ cm}^{-3}$) component. Beyond the two components of molecular gas, they also find that the CO to H_2 conversion

factor (the X factor) may be up to a factor of ~ 10 smaller than the usual value of $10^{20} \text{ cm}^{-2}(\text{K km/s})^{-1}$, or that there is a low optical depth.

Taking advantage of the high and dry *Caltech Submillimeter Observatory*, Bayet et al. (2006) mapped numerous galaxies, including the Antennae, in the $^{12}\text{CO } J = 2 - 1, 3 - 2, 4 - 3, 6 - 5$ and $7 - 6$ transitions along with the $^{13}\text{CO } J = 3 - 2$ transition. These observations suffer, however, from large error bars due in part to atmospheric interference, but are still more than adequate for radiative transfer analysis. While only performing a single component fit, Bayet et al. (2006) found that the molecular gas in the nucleus of NGC 4038 is cooler ($T_{kin} \sim 40 \text{ K}$) and denser ($n_{\text{H}_2} \sim 4 \times 10^5$) than in overlap region, where the gas is warmer ($T_{kin} \sim 150 \text{ K}$) and less dense ($n_{\text{H}_2} \sim 8 \times 10^3$). Furthermore, they were unable to fit the lower J lines well, and suggest that a two-component fit is necessary in both regions.

1.4 Herschel Space Observatory

Launched in May of 2009, the Herschel Space Observatory (*Herschel*) is a single dish submillimeter space telescope. Taking advantage of the lack of atmosphere, *Herschel* explores a largely unobserved portion of the electromagnetic spectrum from $55 - 671 \mu\text{m}$ (Pilbratt et al., 2010). On-board *Herschel* are 3 separate and unique instruments: the Photodetector Array Camera and Spectrometer (PACS, Poglitsch et al. (2010)), the Spectral and Photometric Imaging REceiver (SPIRE, Griffin et al. (2010)) and the Heterodyne Instrument for the Far Infrared (HIFI, de Graauw et al. (2010)). Both PACS and SPIRE are equipped with imaging photometers and spectrometers, with PACS

covering a total spectrum range from $60\ \mu\text{m}$ to $210\ \mu\text{m}$ (140 GHz to 500 GHz), and SPIRE covering a total spectral range from $194\ \mu\text{m}$ to $671\ \mu\text{m}$ (~ 450 GHz to ~ 1545 GHz). HIFI, on the other hand, is a single pixel high resolution spectrometer.

SPIRE's imaging spectrometer is a Fourier transform spectrometer (FTS) (Naylor et al., 2010b) of a Mach-Zender design (Ade et al., 1999). The major benefit to using a spectrometer of a Mach-Zender design is that the Optical Path Difference (OPD) of the two interfering beams is 4 times the distance travelled by the spectrometer centre mirrors (Ade et al., 1999). This helps limit the overall size of the FTS without limiting the performance. The imaging is achieved by two bolometric arrays covering overlapping spectral ranges of $194 - 313\ \mu\text{m}$ (SSW) and $303 - 671\ \mu\text{m}$ (SLW). The bolometers themselves are arranged in a honeycomb pattern (see Figure 1.2), whilst the number of unvignetted detectors is different between the SLW (7) and SSW (17 working). In addition to this, the beam varies in both size and shape not only between the two arrays, but also at different wavelengths of the arrays (e.g. see Figure 1.3). The beam size of the SLW varies from $\sim 29''$ to $\sim 43''$, while in the SSW the beam size varies from $\sim 17''$ to $\sim 22''$ (see Figure 1.3 or Swinyard et al. 2010).

The highest spectral resolution available is $0.048\ \text{cm}^{-1}$, corresponding to 1.4 GHz (Griffin et al., 2010). Even though emission and absorption lines are typically unresolved at these wavelengths, the total flux of the spectral lines is recovered. This, coupled with the large spectral range of the imaging FTS, provides the perfect opportunity to perform line surveys across the entire

FTS band. These line surveys could benefit from further followups using instruments with higher spectral resolutions (i.e. HIFI) to map the line shape. The FTS data also provide ample opportunity for radiative transfer analysis using either a large portion of the CO ladder from $J = 4 - 3$ to $J = 13 - 12$ (e.g. see Panuzzo et al. 2010 or Rangwala et al. 2011), or a combination of molecular species.

1.5 Summary

The primary goal of this thesis is to determine the physical characteristics across the Antennae, particularly in both the nucleus of NGC 4038 and the overlap region, along with determining possible heating mechanisms of the molecular gas in the Antennae. Throughout this thesis, I describe the study of the molecular gas in this particular system using the SPIRE FTS data supplemented by data from the James Clark Maxwell Telescope (JCMT) using the radiative transfer code RADEX. In Chapter 2, I describe the creation of CO integrated intensity maps from the SPIRE FTS data and briefly discuss the JCMT data, including the data reduction process, the line fitting method and the convolution of the various CO maps. I also present the complete spectra in the nucleus of NGC 4038 and the overlap region, along with the integrated intensity maps. In Chapter 3, I describe my use of the non-LTE code RADEX, and discuss the likelihood code used. I then present fits using this likelihood code to the CO spectral line energy distributions (SLEDs) in the nucleus of NGC 4038 and the overlap region, along with the physical parameters from these fits. In Chapter 4, I describe my results, including the

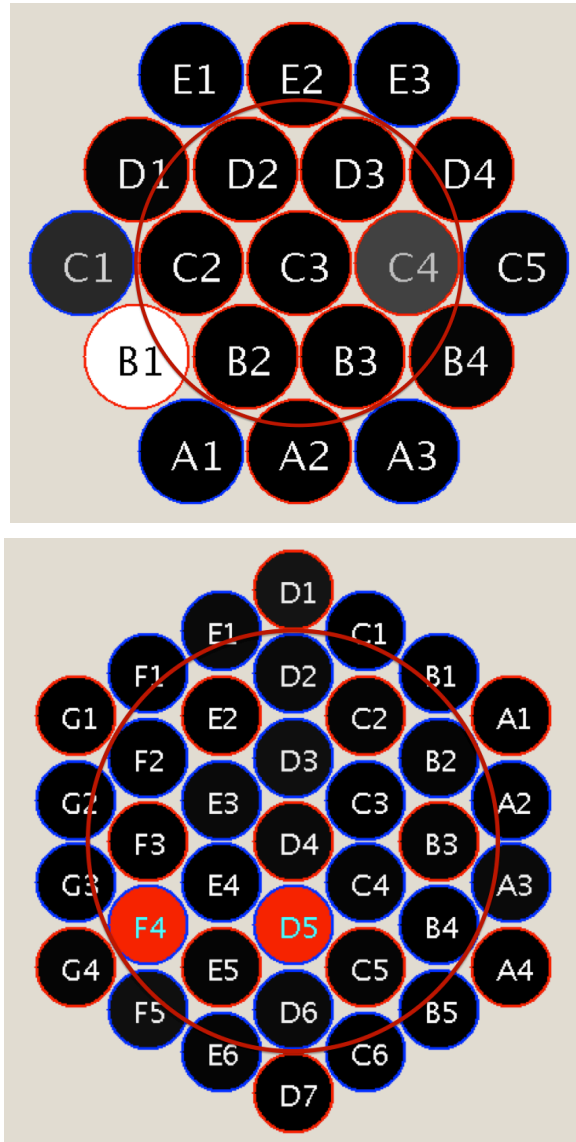


Figure 1.2: Arrangement of the bolometric array for the SLW (*top*) and SSW (*bottom*) (SPI, 2011c). The unvignetted detectors are those found within the red circles, (7 for the SLW, 19 for the SSW), and are the detectors used for science. In addition, 2 of the detectors in the SSW (F4 and D5) are dead and are no longer used for science.

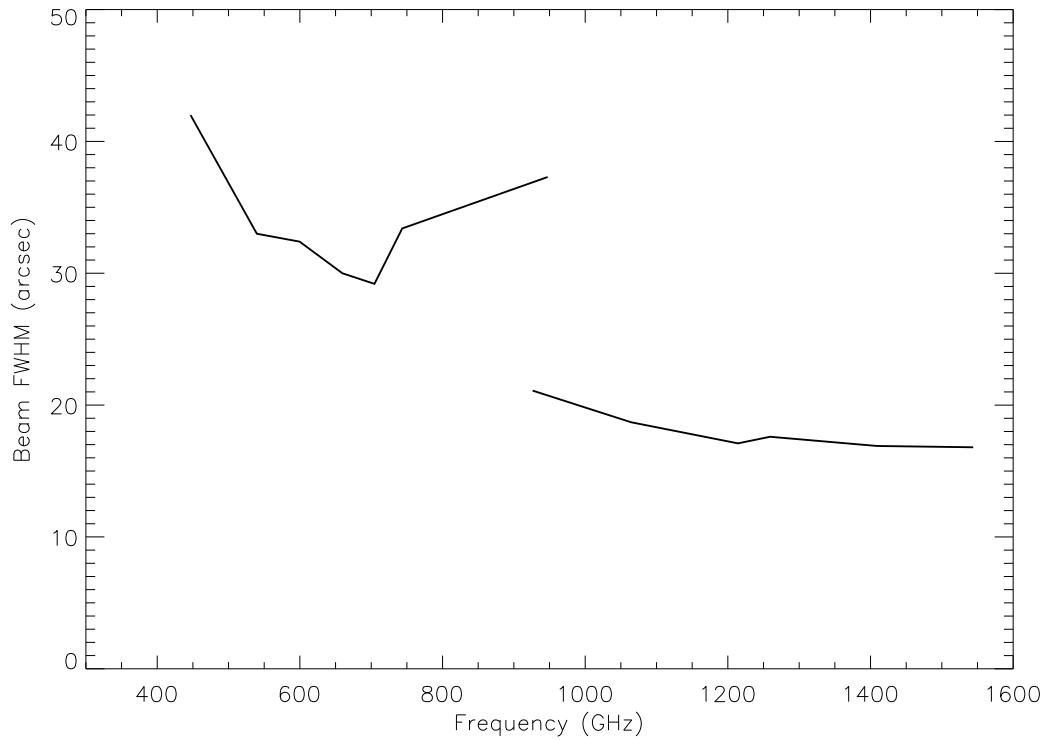


Figure 1.3: Plot demonstrating the varying beam sizes of the SLW (*left*) and SSW (*right*) from Swinyard et al. (2010). Notice that the size of the SSW beam varies considerably less than that of the SLW beam.

integrated intensity maps and the RADEX results, comparing both to previous studies. I also discuss the possible heating mechanisms of the molecular gas in the Antennae. Finally, in Chapter 5, I present conclusions based upon these data and results, along with potential future work. In Appendix A, I present in more detail the data reduction process, and provide examples of the scripts used. In Appendix B, I present my custom line fitting code in detail, along with providing the script used for the line-fitting process.

Chapter 2

Data and Data Reduction

2.1 Observations

FTS data for NGC 4038 was acquired in two separate observations, both on December 12th, 2010 using the SPIRE FTS in high spectral resolution (FWHM = 0.048 cm^{-1}), fully-sampled mode. The total integration time for each observation was 17843 seconds, for a total integration time of 35686 seconds (~ 10 hours). Both observations were processed in the same manner using the Spectrometer Mapping user's script provided with Herschel Interactive Processing Environment (HIPE) version 8.0 build 929. Various versions of the data reduction pipeline and process are detailed in Fulton et al. (2010) and Swinyard et al. (2010); however we have used the most current and up to date version of the script and it is described in Appendix A.

The standard mapping pipeline assumes that the source is extended and uniform, and outputs a spectrum in units of $\text{W m}^{-2} \text{ Hz}^{-1} \text{ sr}^{-1}$. Our source, however, is not truly extended and we need to apply a point source flux conversion correction to account for this. After the correction we obtain a spectrum

in the more natural units of Jy/beam. Currently, the necessary correction is only known for a set of co-aligned detectors in both the SLW and SSW (a total of 7 detector pairs, see Table A.1 and Figure 1.2), however in the future the correction for the other 10 detectors in the SSW will be available. While this set includes all of the unvignetted detectors in the SLW, it only includes 7 of the 17 total operational detectors in the SSW. The remaining 10 detectors are not used to create the SSW map and we are left with very poor spatial coverage. After applying the point source correction, the data were combined into a single level 2 data cube with 15" pixels for the SLW and 10" for the SSW. These pixel sizes were determined empirically to be the ideal compromise between pixel coverage and resolution. Figure 2.1 shows one slice of the SLW spectral cube centred at ~ 458.7 GHz, while figure 2.4 shows one slice of the SSW spectral cube centred at ~ 1453.4 GHz. Figures 2.2 and 2.5 show spectra of the nucleus in the SLW and SSW, respectively, while Figures 2.3 and 2.6 show the same for the overlap region.

2.2 CO Integrated Intensity Maps

A custom script was written to extract the line fluxes for all the CO lines and the [CI] lines in the SLW across the entire level 2 map (see Appendix B). The script works by extracting the complete spectrum at each point in the map. For each spectrum, the continuum is removed by fitting a high order polynomial (19th) to the continuum and subtracting it. Then, starting with

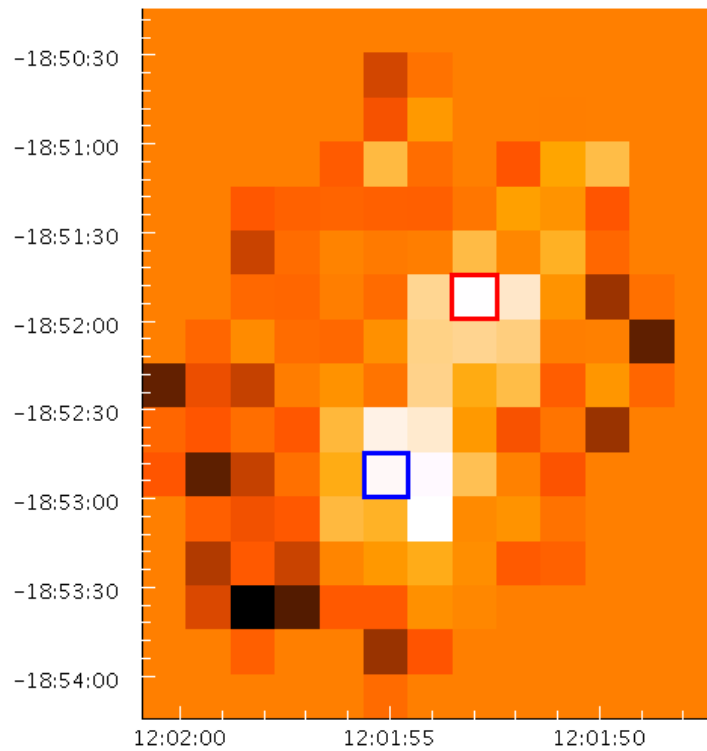


Figure 2.1: Slice of the SLW data cube at ~ 458.7 GHz. The red box identifies the pixel representing the nucleus of NGC 4038, while the blue box identifies the pixel representing the overlap region.

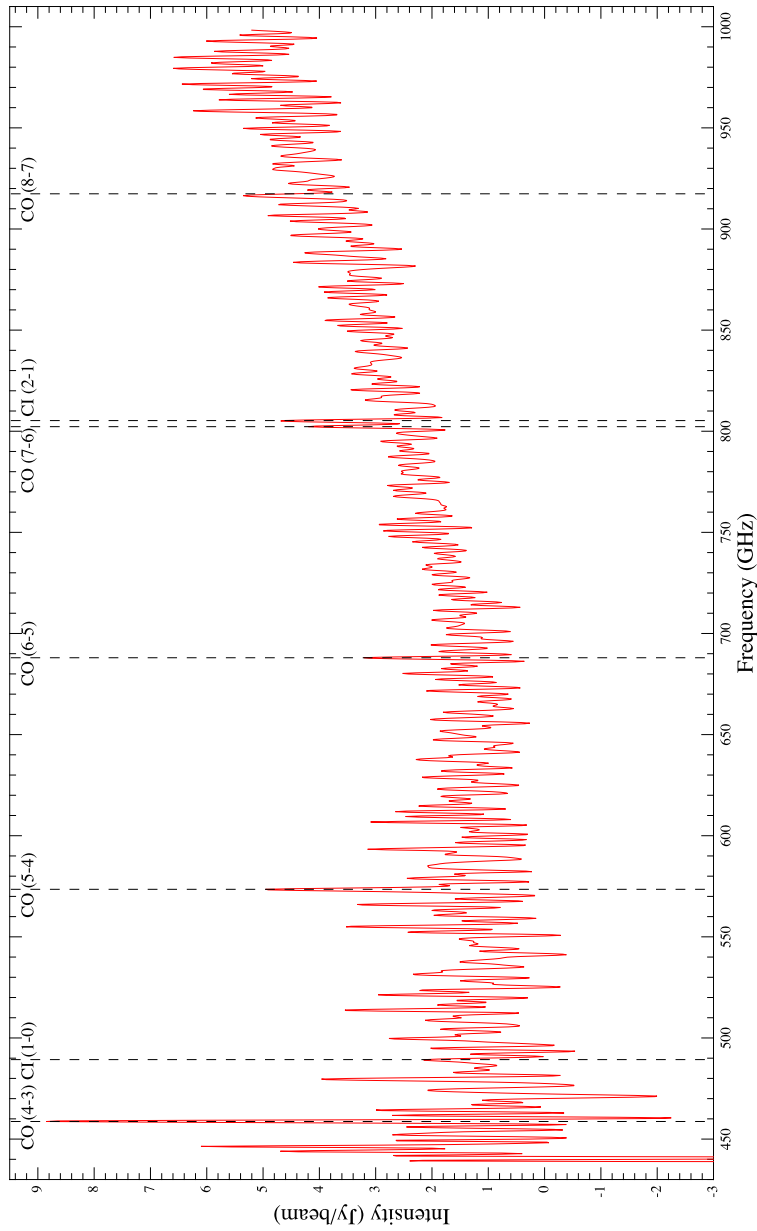


Figure 2.2: SLW spectrum for brightest region of nucleus of NGC 4038 corresponding to the red box in Figure 2.1. I have identified 5 CO lines and both [CI] lines. There are still lines to be identified in this spectrum.

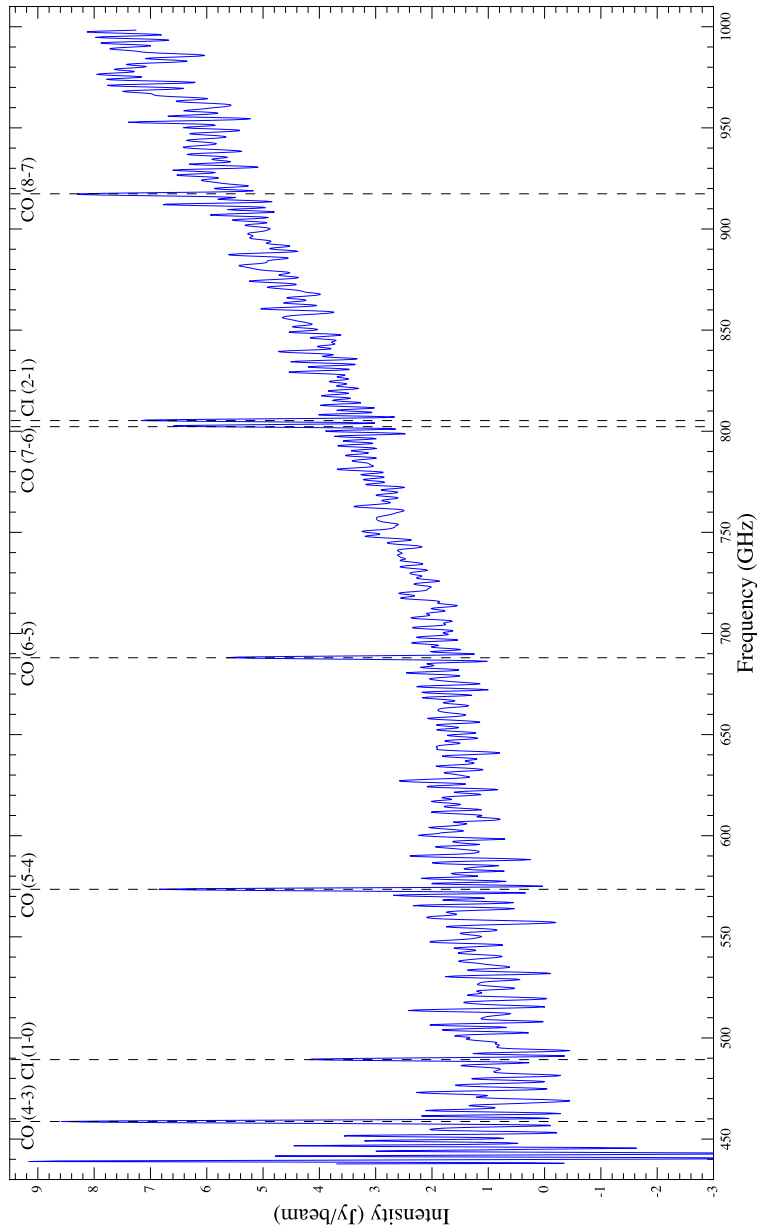


Figure 2.3: SLW spectrum for brightest region of the overlap region corresponding to the blue box in Figure 2.1. I have identified 5 CO lines and both [CI] lines. There are still lines to be identified in this spectrum.

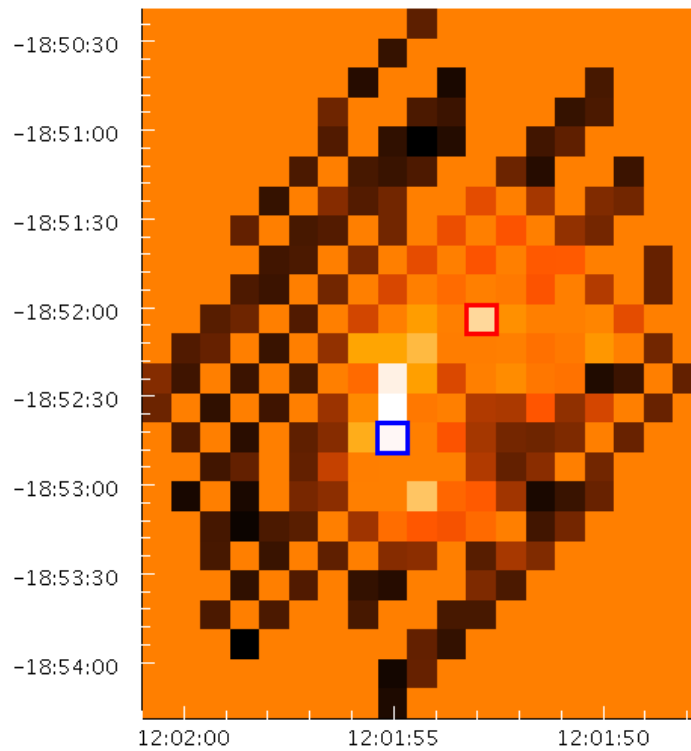


Figure 2.4: Slice of the SSW data cube at ~ 1453.4 GHz. The red box identifies the pixel representing the nucleus of NGC 4038, while the blue box identifies the pixel representing the overlap region.

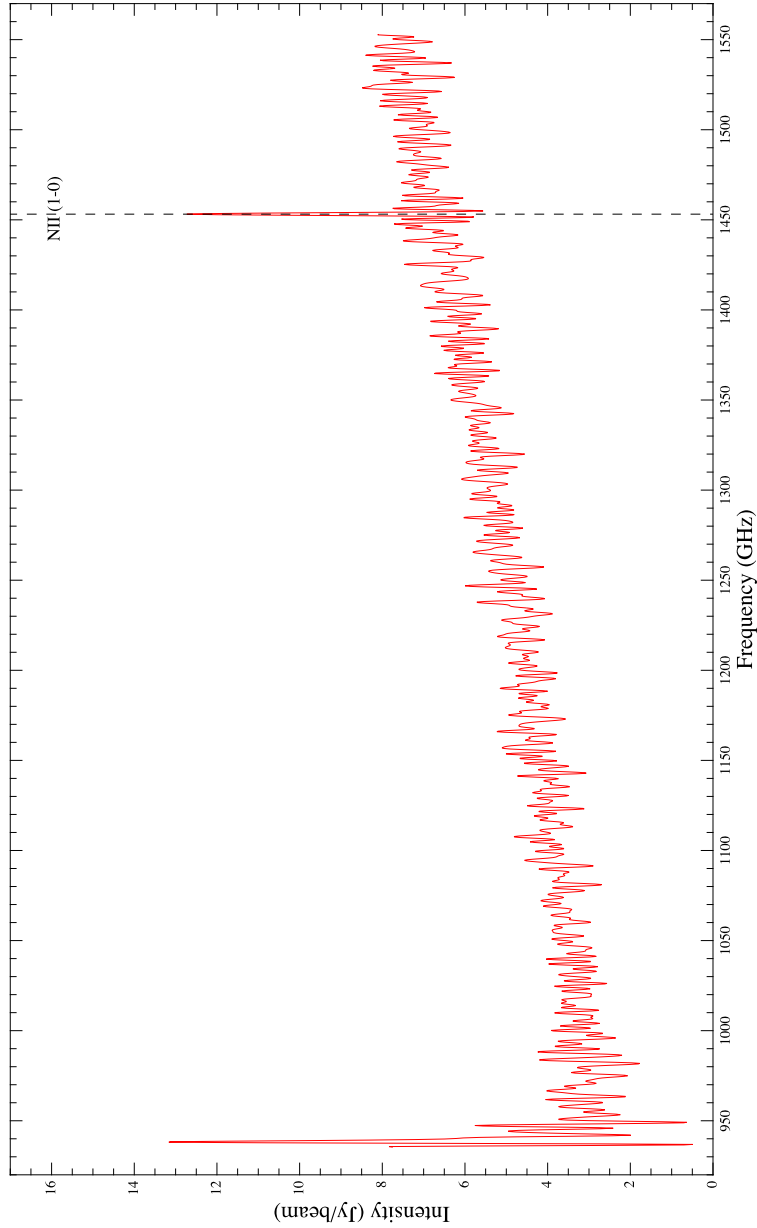


Figure 2.5: SSW spectrum for brightest region of nucleus of NGC 4038 corresponding to the red box in Figure 2.4. Only the [NII] line at ~ 1460 GHz has been identified so far; however there are numerous potential candidates for other lines throughout the spectrum.

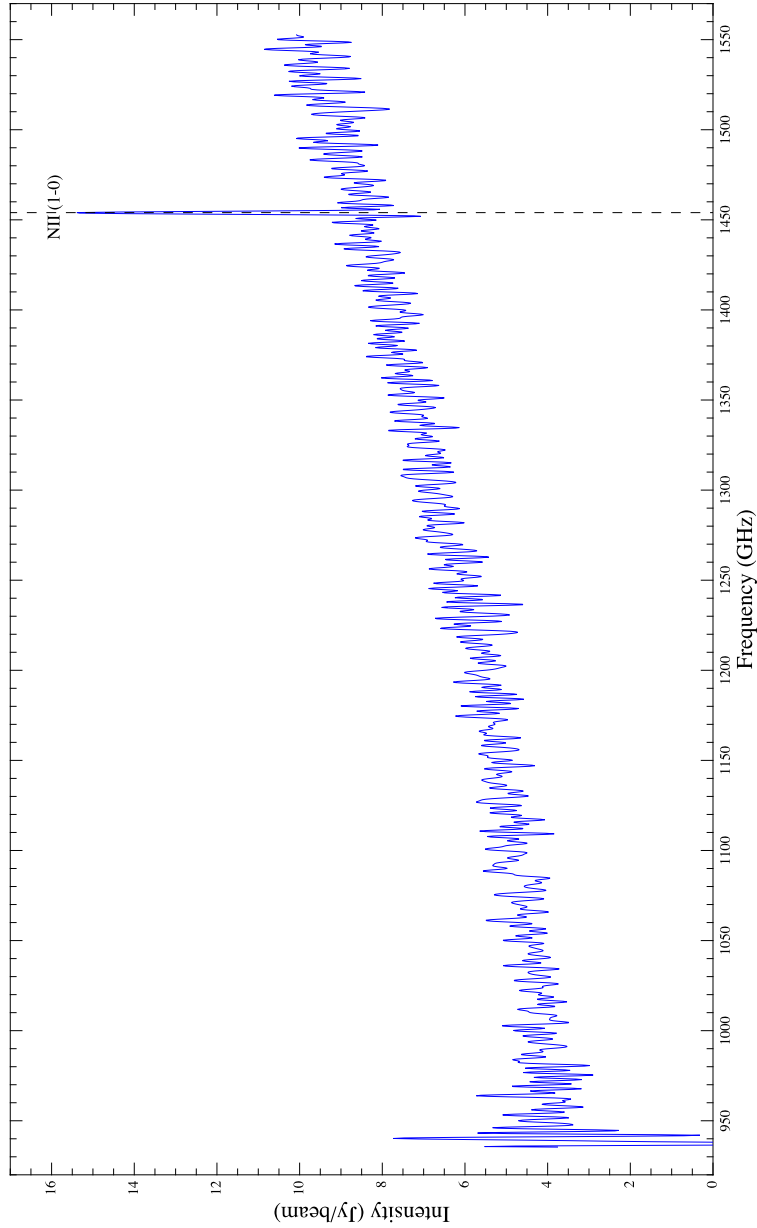


Figure 2.6: SSW spectrum for brightest region of the overlap region corresponding to the blue box in Figure 2.4. Only the [NII] line at ~ 1460 GHz has been identified so far; however there are numerous potential candidates for other lines throughout the spectrum.

the CO $J = 4 - 3$ line and working up in frequency, each line is fit with a sinc function of the form

$$f(\nu) = A \operatorname{sinc}\left(\frac{\nu - \nu_0}{\Delta\nu}\right) \quad (2.1)$$

where A is the amplitude of the line, ν is the frequency of the line and $\Delta\nu$ is the line width in GHz. Equivalently, in velocity units, the sinc functions are of the form

$$f(v) = A \operatorname{sinc}\left(\frac{v - v_0}{\Delta v}\right) \quad (2.2)$$

$\Delta\nu$ is related to Δv via

$$\Delta v = \frac{\Delta\nu}{\nu_0} c \quad (2.3)$$

where c is the speed of light in km/s and Δv is the line width in km/s. When two lines are partially blended, both lines are fit simultaneously with sinc functions. The lines are fit using either a Levenberg-Marquardt fitter or, in the case of the CO $J = 5 - 4$ line, an Amoeba fitter (SPI, 2011b), both of which return values and standard deviations for all of the fit parameters.

The integrated intensity of each emission line in units of Jy km/s is calculated by integrating the sinc function

$$I(\text{mol}) = \int_{-\infty}^{\infty} A \operatorname{sinc}\left(\frac{v - v_0}{\Delta v}\right) \quad (2.4)$$

$$= A\pi\Delta v \quad (2.5)$$

$$= \frac{Ac\pi\Delta\nu}{\nu_0} \quad (2.6)$$

The standard deviation of the integrated intensity is calculated via

$$\sigma_{I^2(\text{mol})} = I(\text{mol})^2 \left[\left(\frac{\sigma_A}{A}\right)^2 + \left(\frac{\sigma_{\Delta\nu}}{\Delta\nu}\right)^2 + \left(\frac{\sigma_{\nu_0}}{\nu_0}\right)^2 \right] \quad (2.7)$$

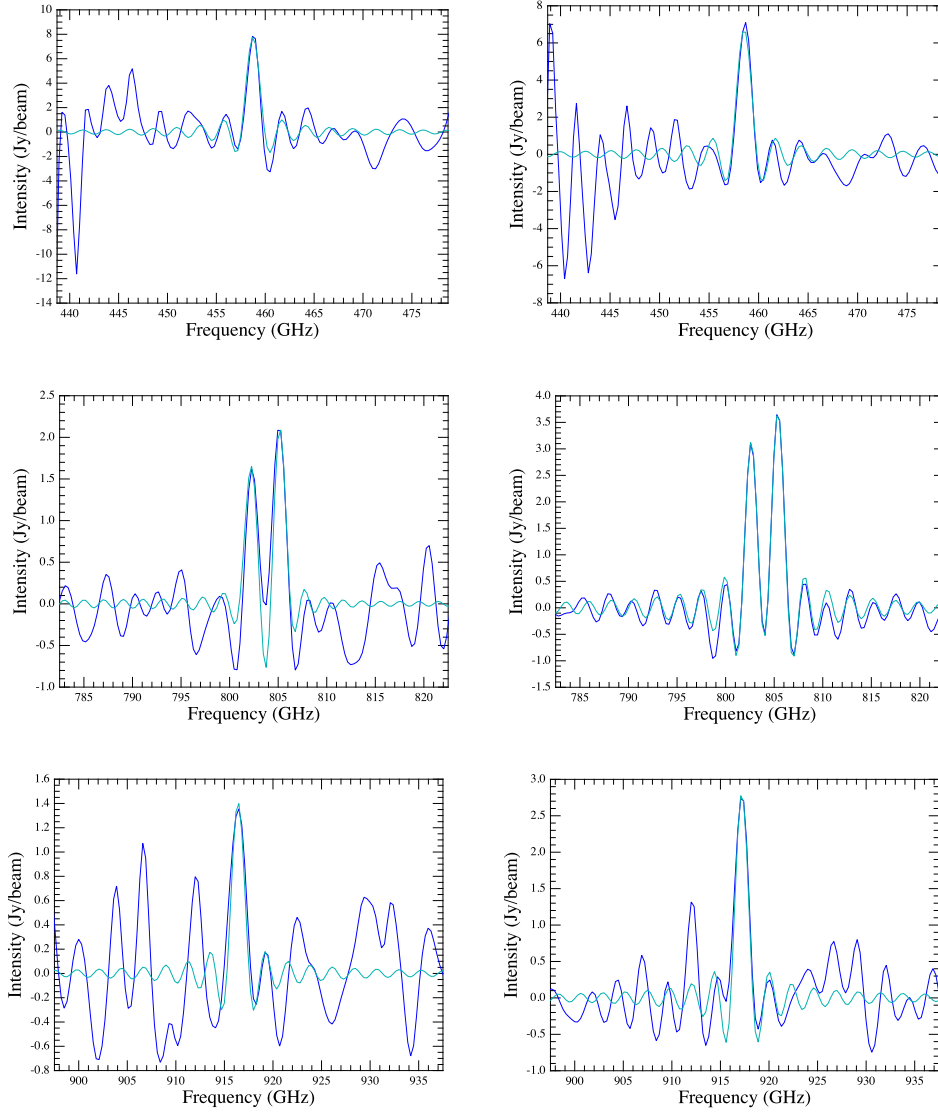


Figure 2.7: Line fits for the nucleus of NGC 4038 (*left*) and overlap region (*right*). The fits are for the (from top to bottom) the $J = 4 - 3$ transition, the CO $J = 7 - 6$ and [CI] $J = 2 - 1$ doublet, and the CO $J = 8 - 7$ transition.

2.2.1 FTS beam correction

Since the FTS beam size and shape varies with frequency across both the SLW and the SSW (Swinyard et al., 2010), we need to convolve the individual $I(\text{CO})$ maps to match the beams. The raw 2-dimensional beam profile data were fit with numerous different functions in order to properly assess the beam: 2-dimensional Gaussian and Airy functions by G. Makiwa, and a series of 6 Hermite polynomials by M. Ferlet. In the end, it was decided that the best fit to the beam was that using the Hermite polynomials. Using these fits, unique convolution kernels to convolve the $J = 5 - 4$, $6 - 5$, $7 - 6$, and $8 - 7$ CO integrated maps to match the beam of the CO $J = 4 - 3$ integrated map were created by G. Bendo using the method described in Bendo et al. (2010). The convolution was performed using the *Kappa*, *Convert* and *Gaia* from the Starlink Project (Wilson et al., 2009). The resulting maps were renormalized by dividing by the ratio of the beam areas so that the total flux in the map remained constant after the convolution process.

2.2.2 Jy/beam km/s to K km/s conversion

The convolved integrated intensity maps were converted from units of Jy/beam km/s to K km/s by the following equation

$$I_{\text{CO}} = S_{\text{CO}} \left[0.0109 \left(\frac{\nu}{115 \text{ GHz}} \right)^2 \sigma^2 \right]^{-1} \quad (2.8)$$

where I_{CO} is the integrated intensity in K km/s, S_{CO} is the integrate intensity in Jy/beam km/s, ν is the line centre in GHz and σ is the beamsize in arcseconds. Since all of the maps have been convolved to match a beamsize of

43.4", this is the beamsize used in this equation. The resulting maps can be seen in Figures 2.8, 2.9, 2.10, 2.11, and 2.12.

2.3 JCMT CO $J = 3 - 2$ Map

The JCMT observations were provided by C. Wilson in the form of both a spectral cube and an integrated intensity map. The pixel size of the map is 7.27". The integrated intensity map was convolved to match the beam size and shape of the FTS $J = 4 - 3$ map assuming a gaussian beam. Using the full spectral cube, I calculated the line width in the nucleus of NGC 4038 and the overlap region by fitting the spectral line with a gaussian. The line widths are 110 km/s for the nucleus of NGC 4038 and 190 km/s for the overlap region. The CO $J = 3 - 2$ map can be seen in Figure 2.13.

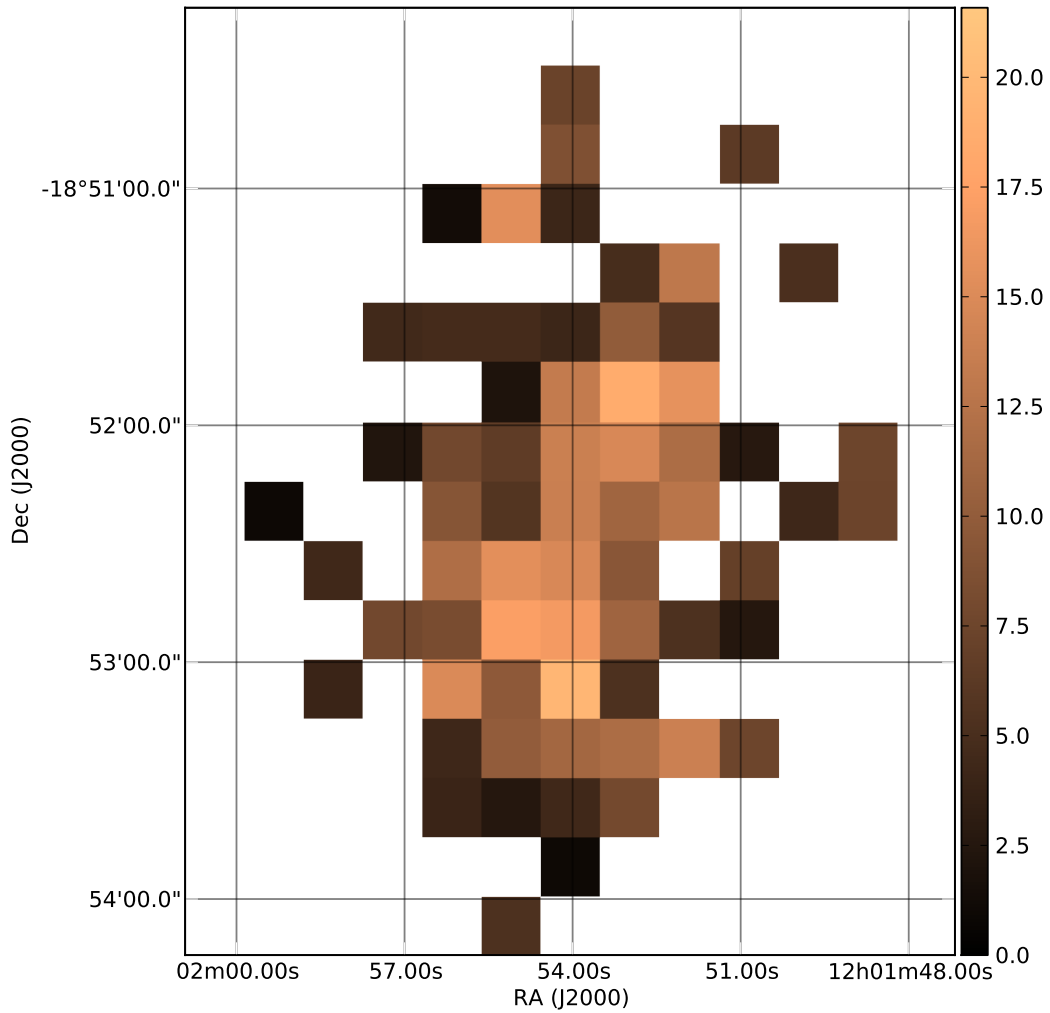


Figure 2.8: Integrated intensity map for CO $J = 4 - 3$ in units of K km/s.

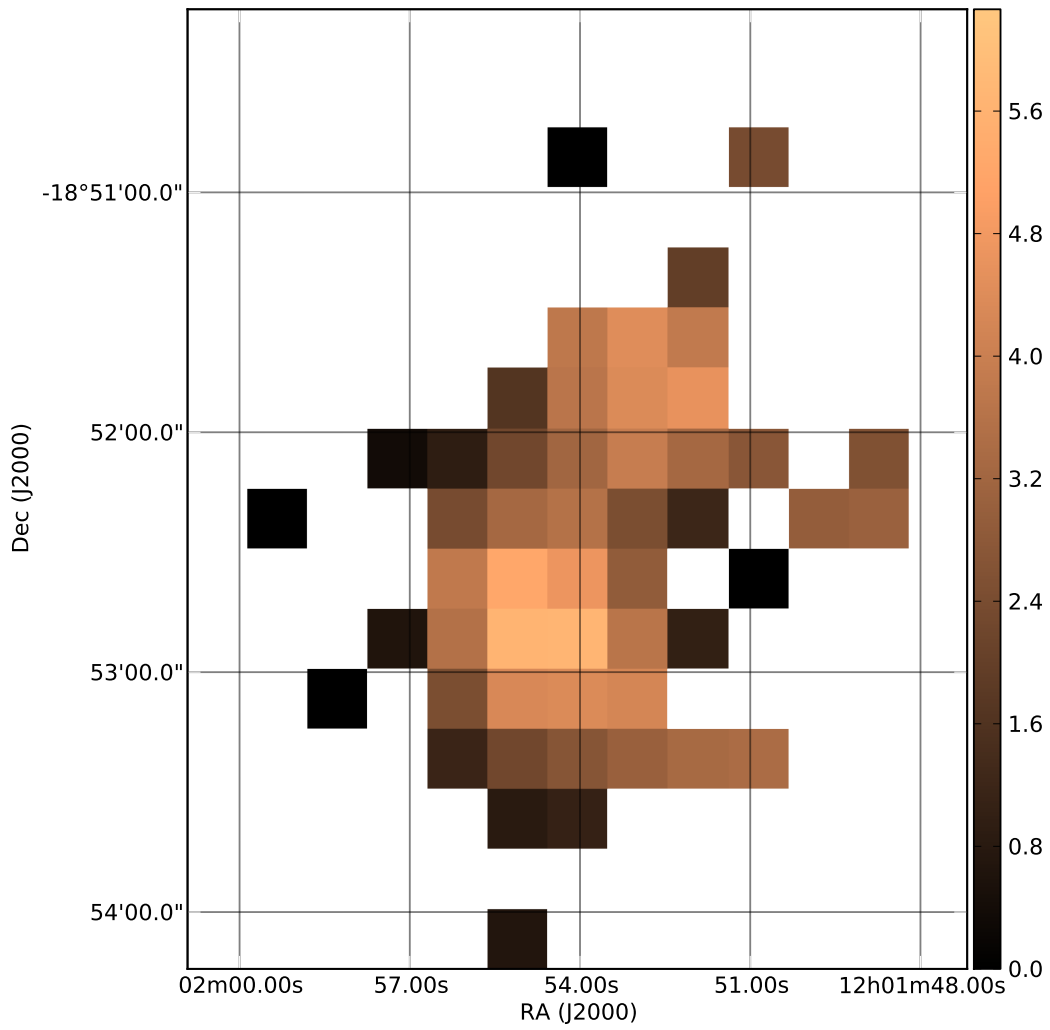


Figure 2.9: Integrated intensity map for CO $J = 5 - 4$ in units of K km/s.

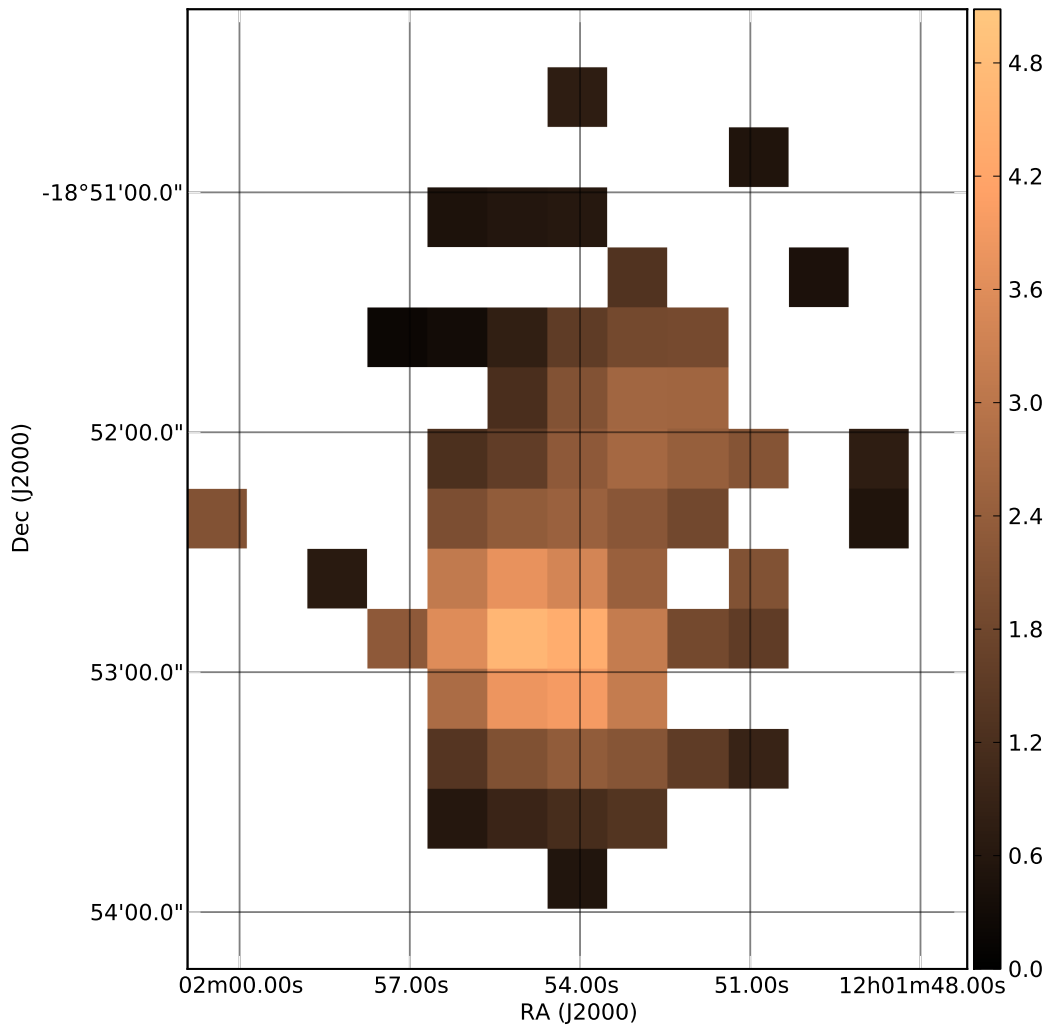


Figure 2.10: Integrated intensity map for CO $J = 6 - 5$ in units of K km/s.

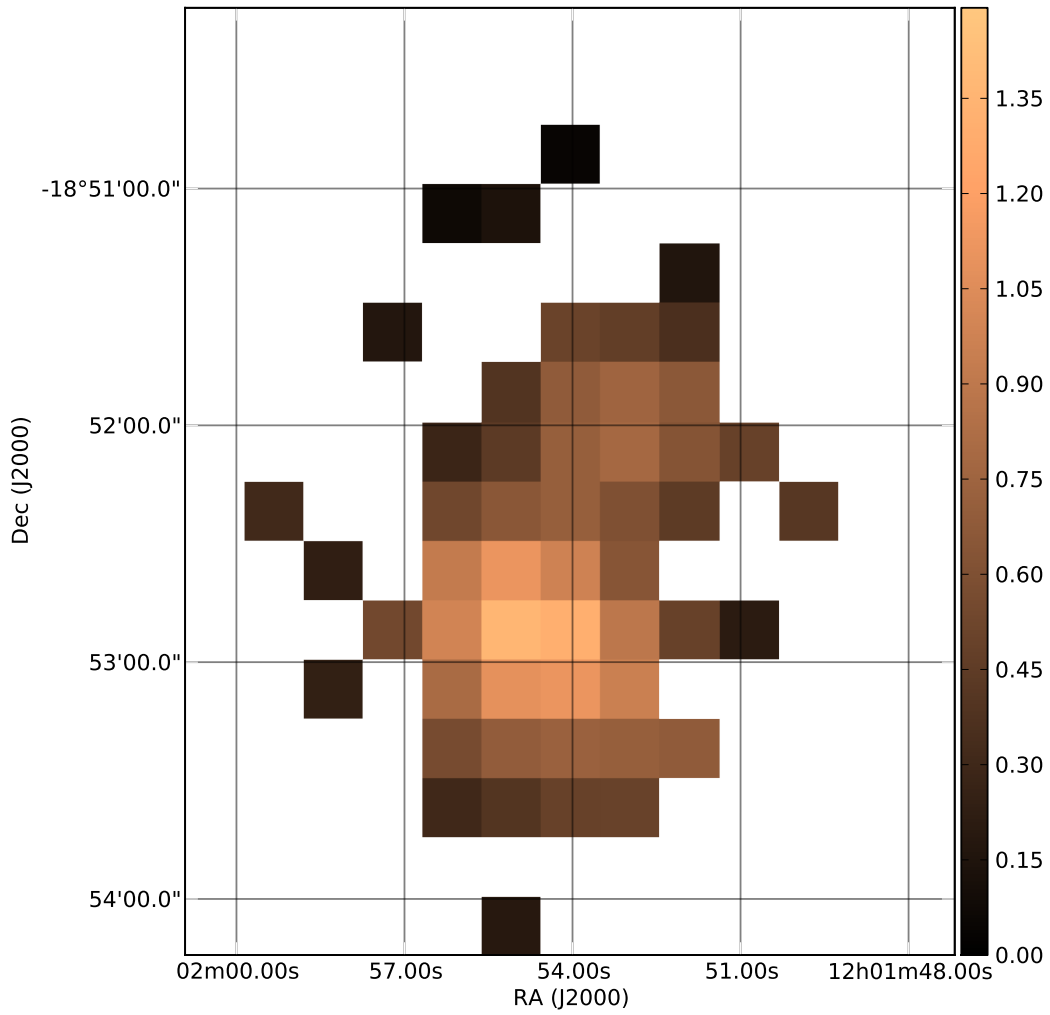


Figure 2.11: Integrated intensity map for CO $J = 7 - 6$ in units of K km/s.

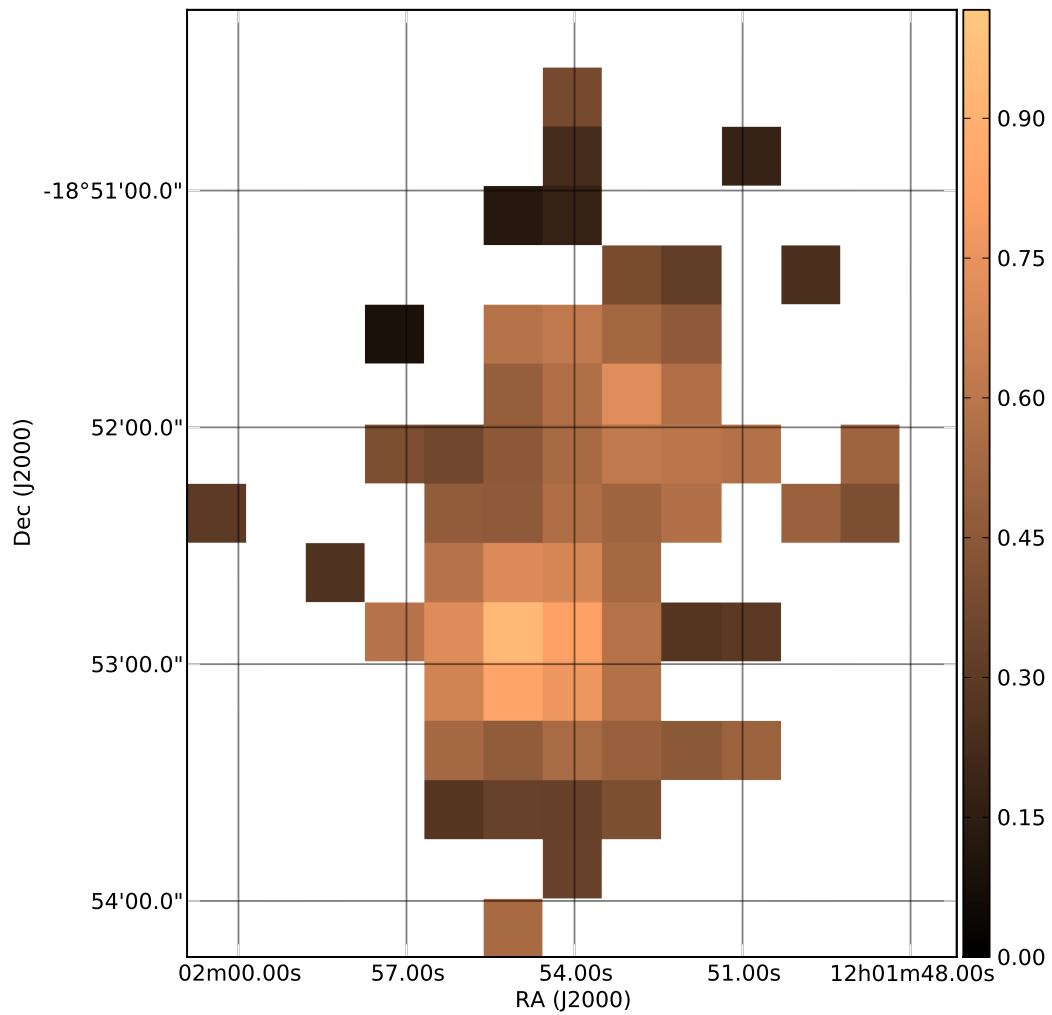


Figure 2.12: Integrated intensity map for CO $J = 8 - 7$ in units of K km/s.

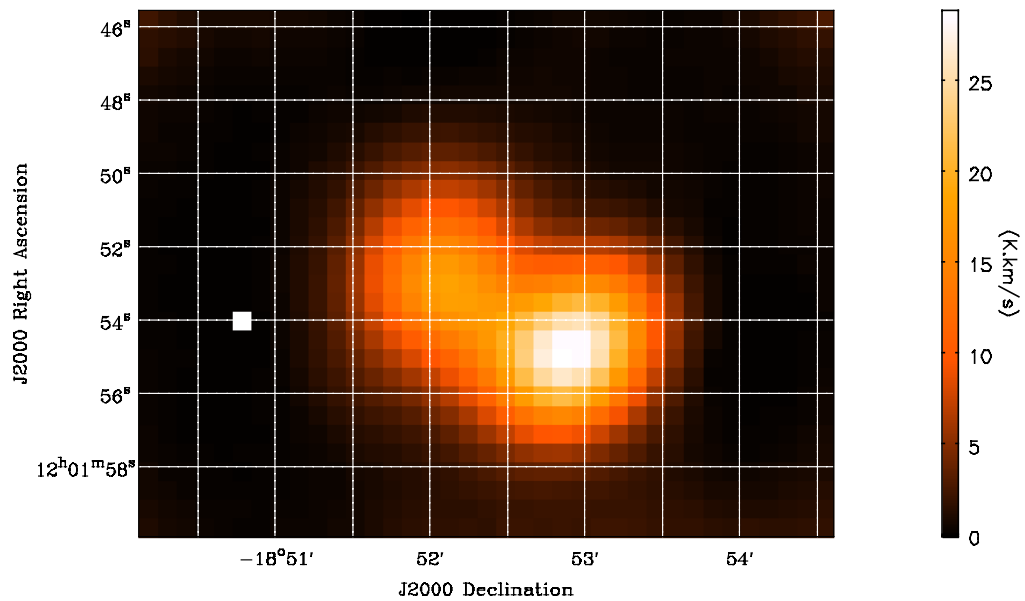


Figure 2.13: Integrated intensity map for CO $J = 4 - 3$ in units of K km/s. Note that the Declination is on the x-axis, and the Right Ascension is on the y-axis.

Chapter 3

Non-Local Thermal Equilibrium Analysis (RADEX)

3.1 RADEX

Analysis of the physical parameters of the molecular gas was performed using the non-LTE radiative transfer code RADEX (van der Tak et al., 2007). I used a modified version of the standard RADEX code by P. Maloney (Panuzzo et al., 2010) with the primary benefit of being optimized to take less time to run. RADEX iteratively solves for statistical equilibrium based upon an input kinetic temperature (T_{kin}), molecular gas density (n_{H_2}) and CO column density per unit line width ($N_{12CO}/\Delta v$). It is able to calculate line fluxes for a set of given physical parameters of any molecular species for which basic molecular data is known. RADEX also requires that the user select one of three options for calculating the escape probability of photons, and the choice is dependent upon the physical conditions of the molecular gas region being modelled (van der Tak et al., 2007). The three options are a uniform sphere, an expanding sphere (LVG) and a plane-parallel slab. For my RADEX models,

I use the expanding sphere, also known as the LVG approximation. For the LVG model, the geometrically-averaged escape probability β_{LVG} is calculated from the optical depth τ by

$$\beta_{LVG} = \frac{1 - e^{-\tau}}{\tau} \quad (3.1)$$

By varying the temperature, gas density and column density, a grid of models with varying line fluxes is calculated. By comparing the measured line fluxes to those calculated by RADEX, it is possible to determine the physical conditions of the molecular gas. This method is best used when you have multiple transitions of the same molecular species. It is possible to perform radiative transfer calculations for multiple molecular species; however one must be careful when combining molecules which trace vastly different densities and temperatures of molecular gas, as they may trace a completely different component of the molecular gas. Even across the CO ladder there can exist multiple components to the molecular gas, especially with the higher J CO transitions (see e.g. Rangwala et al. 2011). I perform a likelihood analysis to compare RADEX results to the 5 CO lines in the SLW along with the CO $J = 3 - 2$ data from the JCMT.

3.2 Likelihood analysis

In order to perform the likelihood analysis, I use an updated version of the likelihood code used by Ward et al. (2003) and Panuzzo et al. (2010), provided to me by the ZSpec team. The code assumes Bayes' theorem

$$P(\mathbf{a}|\mathbf{M}, \sigma) = \frac{P(\mathbf{a})P(\mathbf{M}|\mathbf{a}, \sigma)}{\int d\mathbf{a}P(\mathbf{a})P(\mathbf{M}|\mathbf{a}, \sigma)} \quad (3.2)$$

Here, \mathbf{a} is a set of RADEX inputs, \mathbf{M} is a set of n measured line intensities, and σ is the set of measurement uncertainties of \mathbf{M} . The $P(\mathbf{M}|\mathbf{a}, \sigma)$ probability density is calculated assuming that the measured line intensities have Gaussian distributed random errors (Ward et al., 2003). It takes the form

$$P(\mathbf{M}|\mathbf{a}, \sigma) = \prod_{i=1}^n \frac{1}{\sqrt{2\pi}\sigma_i} \exp\left(-\frac{1}{2} \left[\frac{M_i - T_i(\mathbf{a})}{\sigma_i}\right]^2\right) \quad (3.3)$$

where $T_i(\mathbf{a})$ are the calculated line intensities from a set of input parameters \mathbf{a} , and σ_i is the random error associated with the measured line M_i . $P(\mathbf{a})$ is the prior for a set of parameters \mathbf{a} .

3.2.1 Priors

Two priors have been previously implemented into the likelihood code to eliminate unphysical solutions in our RADEX analysis. These priors are binary in a sense that they are either 1 or 0; if the prior is violated, $P(\mathbf{a}) = 0$, otherwise $P(\mathbf{a}) = 1$. The first prior places a limit on the beam-averaged CO column density, defined as the column density times the area filling factor ($\langle N(\text{CO}) \rangle = N(\text{CO})\Phi_A$). This differs from Panuzzo et al. (2010) as they place the same limit on the column density as calculated by RADEX, and not the beam-averaged column density. $\langle N(\text{CO}) \rangle$ is prevented from exceeding the theoretical limit of the column density calculated from the dynamical mass

(M_{dyn}), the CO abundance (x_{CO}), and the area of the CO region (A_{CO}) (Panuzzo et al., 2010).

$$\langle N(\text{CO}) \rangle < \frac{M_{dyn} x_{CO}}{\mu m_{\text{H}_2} A_{CO}} \quad (3.4)$$

The values for each of the parameters for both the nucleus of NGC 4038 and the overlap region can be found in Table 3.1, and constitute an upper limit of $\langle N(\text{CO}) \rangle < 1.5 \times 10^{19} \text{ cm}^{-2}$ for the nucleus of NGC 4038, and $\langle N(\text{CO}) \rangle < 5.2 \times 10^{19} \text{ cm}^{-2}$ for the overlap region.

The second prior prevents the column length from exceeding the length of the molecular region (L). The column length is calculated by dividing the column density by the square root of the source filling factor (Φ_A), the CO abundance and the density of molecular hydrogen (n_{H_2}), yielding the relation (Panuzzo et al., 2010)

$$\frac{N(\text{CO})}{\sqrt{\Phi_A} x_{CO} n_{\text{H}_2}} \leq L \quad (3.5)$$

For the nucleus of NGC 4038, I used a length of $L = 1700 \text{ pc}$ (Wilson et al., 2000). For the overlap region, there are 5 large SGMCs as opposed to one molecular region. For the prior on the column density, I used the length of the largest SGMC in the overlap region, which is $L = 1400 \text{ pc}$ (Wilson et al., 2000).

3.3 Results

I calculated a grid of models using RADEX and the parameters detailed in Table 3.2. The line intensities and fitting uncertainties for the $J = 4 - 3$ to $J = 8 - 7$ transitions were extracted from the maps calculated in Chapter 2 using

Table 3.1: Parameters used to calculate priors

Parameter	Nucleus of NGC 4038	Overlap region
Source size (")	14	21
Line width (km/s)	110	190
CO abundance	3×10^{-4}	3×10^{-4}
Distance (Mpc)	24.9	24.9
Length (pc)	1700	1400
Dynamical mass (M_{\odot})	1.3×10^9	3.0×10^9
Angular scale (pc/")	121	121

pixel 5,5 (R.A. = $12^h01^m55^s.1$, decl = $-18^{\circ}52'51.3''$) for the overlap region, and pixel 9,7 (R.A. = $12^h01^m53^s.0$, decl = $-18^{\circ}51'51.7''$) for the nucleus of NGC 4038, while the CO $J = 3 - 2$ line intensity was extracted from the JCMT map (Table 3.3). A 15% calibration error was added in quadrature to the $J = 3 - 2$ lines, while a 20% calibration error (SPI, 2011c) was added to the $J = 4 - 3$ to $J = 8 - 7$ lines (not shown in table). It is important to note that the column density $N(\text{CO})$ and Φ_A are somewhat degenerate, and cannot be well constrained individually. Their product, $\langle N(\text{CO}) \rangle$ can, however, be constrained and is the more physically relevant parameter.

Table 3.2: RADEX model grid parameters

	Range	Number of points
$T_{kin}[\text{K}]$	20 – 1500	152
$n_{\text{H}_2}[\text{cm}^{-3}]$	$10^{2.0} - 10^{6.0}$	171
$N(\text{CO})/\Delta v[\text{cm}^{-2}(\text{km/s})^{-1}]$	$10^{13.0} - 10^{18}$	221

For each set of line fluxes, the likelihood code will output three solutions. The first is the median solution, calculated from the 1-dimensional distributions for each of the parameters. The second is the 1-dimensional maximum (1DMax) solution. This solution is calculated independently for each param-

Table 3.3: Measured line intensities and measurement uncertainties

Transition	Nucleus (K km/s)	Overlap (K km/s)
3 – 2	17.7 ± 0.3	28.8 ± 0.4
4 – 3	18.7 ± 1.4	17.3 ± 1.0
5 – 4	4.4 ± 0.7	5.7 ± 0.3
6 – 5	2.6 ± 0.2	4.7 ± 0.1
7 – 6	0.75 ± 0.11	1.36 ± 0.05
8 – 7	0.72 ± 0.05	0.94 ± 0.06

eter, and it is where the probability distribution is at its maximum. Finally, there is the 4-dimensional maximum (4DMax) solution, which is calculated as the maximum of the 4-dimensional probability distribution generated by the T_{kin} , n_{H_2} , $N(\text{CO})$ and Φ_A parameters. The remaining parameters, such as pressure, are taken to be their 1DMax solutions. Because the $N(\text{CO})$ and Φ_A parameters are anti-correlated, the 1DMax and median solutions do not always fit the SLED. Therefore, the most physically relevant solution is the 4DMax solution.

Two separate cases for each of the nucleus of NGC 4038 and the overlap region were run through the likelihood code: one with all 6 CO transitions ($J = 3 - 2$ to $8 - 7$), and one with the $J = 4 - 3$ to $8 - 7$ transitions. I consider these two cases as a means of investigating the possibility of two or more components of the molecular gas. In cases where there are multiple components to the molecular gas, the bulk of the lower J emission arises from the cold component, while the warm/hot component is responsible for the higher J transitions (e.g. see Panuzzo et al. 2010 or Rangwala et al. 2011). The most probable solutions from both the 1-dimensional and 4-dimensional probability distributions, along with the 1 sigma range, can be seen in Tables

3.4 and 3.5 for the nucleus of NGC 4038, and Tables 3.6 and 3.7 for the overlap region, while the measured and most probable SLEDs for all 4 of the cases are seen in Figure 3.1. The probability distributions for the various variables are shown in Figures 3.2 and 3.4 for the nucleus of NGC 4038 and Figures 3.3 and 3.5 for the overlap region.

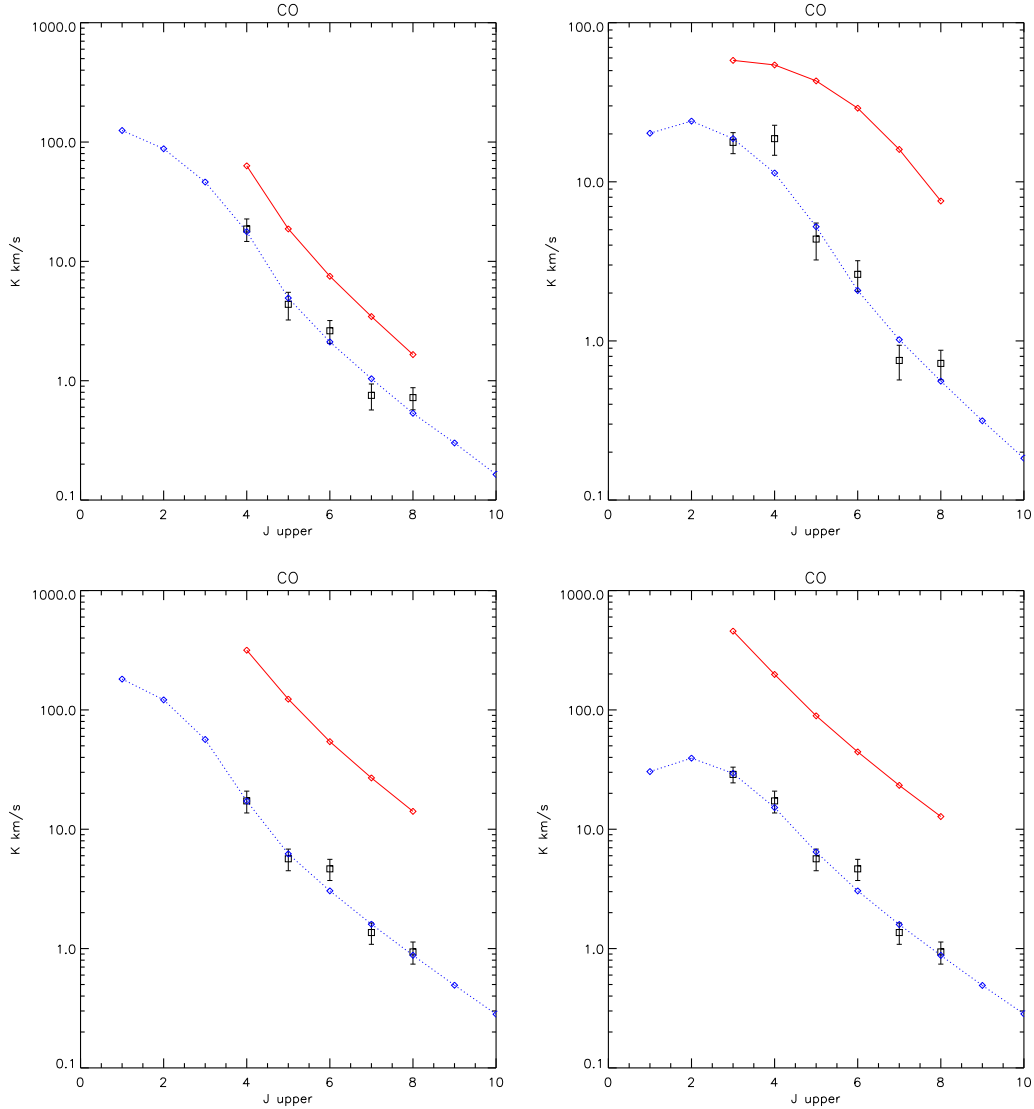


Figure 3.1: CO spectral line energy distributions for nucleus of NGC 4038 (*top*) and overlap region (*bottom*). The calculations were performed with the CO $J = 4 - 3$ to $8 - 7$ lines (*left*) and the CO $J = 3 - 2$ to $8 - 7$ lines (*right*). The solid red line is the CO SLED as calculated by RADEX from the 1DMax parameters, while the blue dashed line is as calculated by RADEX from the 4DMax parameters. The 4DMax solution provides a superior fit as it accounts for the degeneracy of $N(\text{CO})$ and Φ_A .

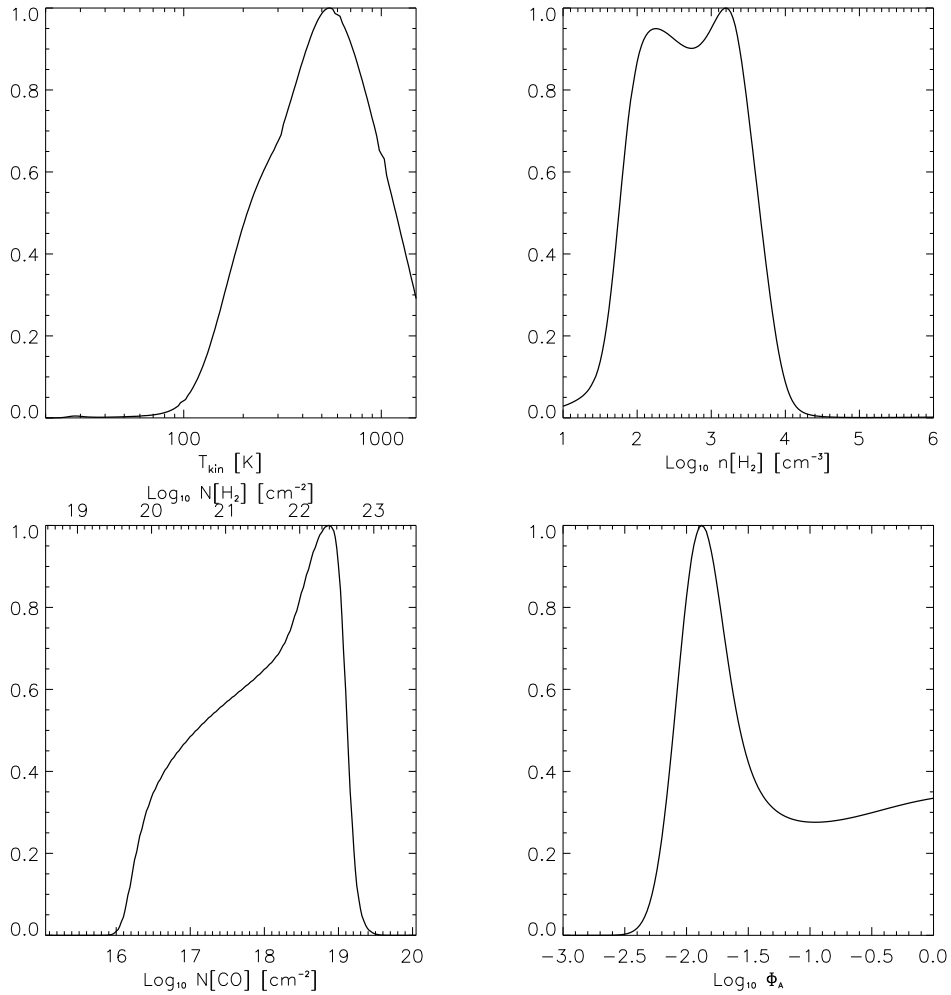


Figure 3.2: Normalized likelihood distributions for the nucleus of NGC 4038 for the kinetic temperature (*top left*), gas density (*top right*), CO column density (*bottom left*) and source filling factor (*bottom right*). The CO emission lines measured from the FTS SLW and the JCMT ($J = 3-2$ to $8-7$) were included in these calculations.

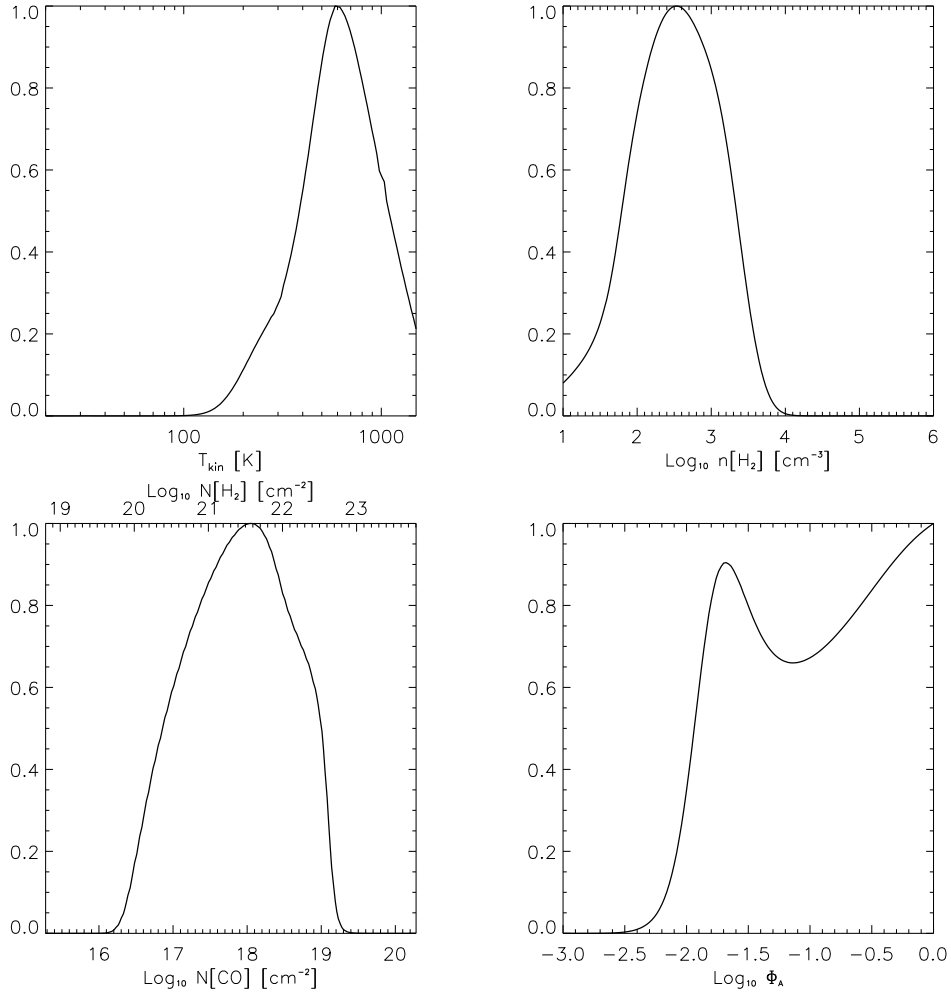


Figure 3.3: Normalized likelihood distributions for the overlap region of the Antennae for the kinetic temperature (*top left*), gas density (*top right*), CO column density (*bottom left*) and source filling factor (*bottom right*). The CO emission lines measured from the FTS SLW and the JCMT ($J = 3 - 2$ to $8 - 7$) were included in these calculations.

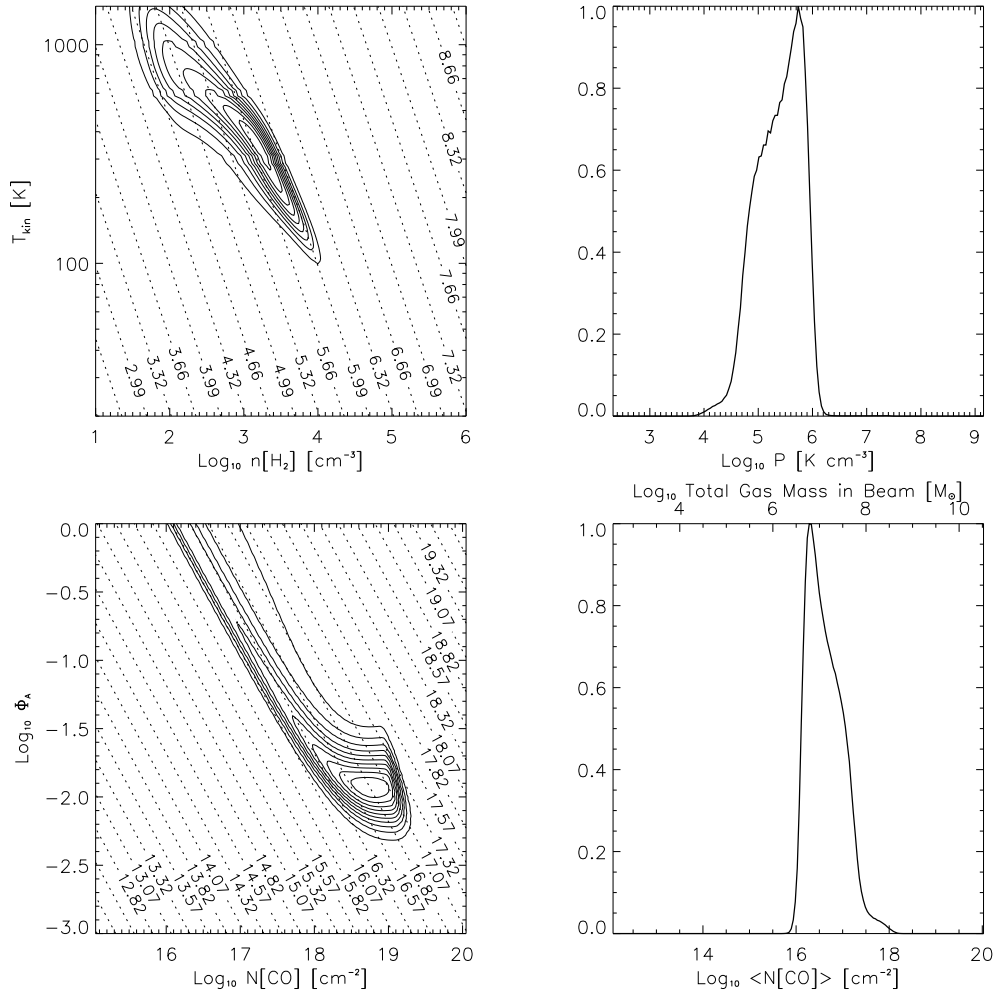


Figure 3.4: Normalized 1-D (*right*) and 2-D (*left*) likelihood distributions for the nucleus of NGC 4038. The 2-D contour plots are for the kinetic temperature and gas density (*top left*), and filling factor and CO column density (*bottom left*). The 1-D distributions are for the pressure (*top right*) and beam average column density (*bottom right*). The dotted lines in the 2-D contour plots correspond to the pressure (*top left*) and the beam average column density (*bottom left*). The CO emission lines measured from the FTS SLW and the JCMT ($J = 3 - 2$ to $8 - 7$) were included in these calculations.

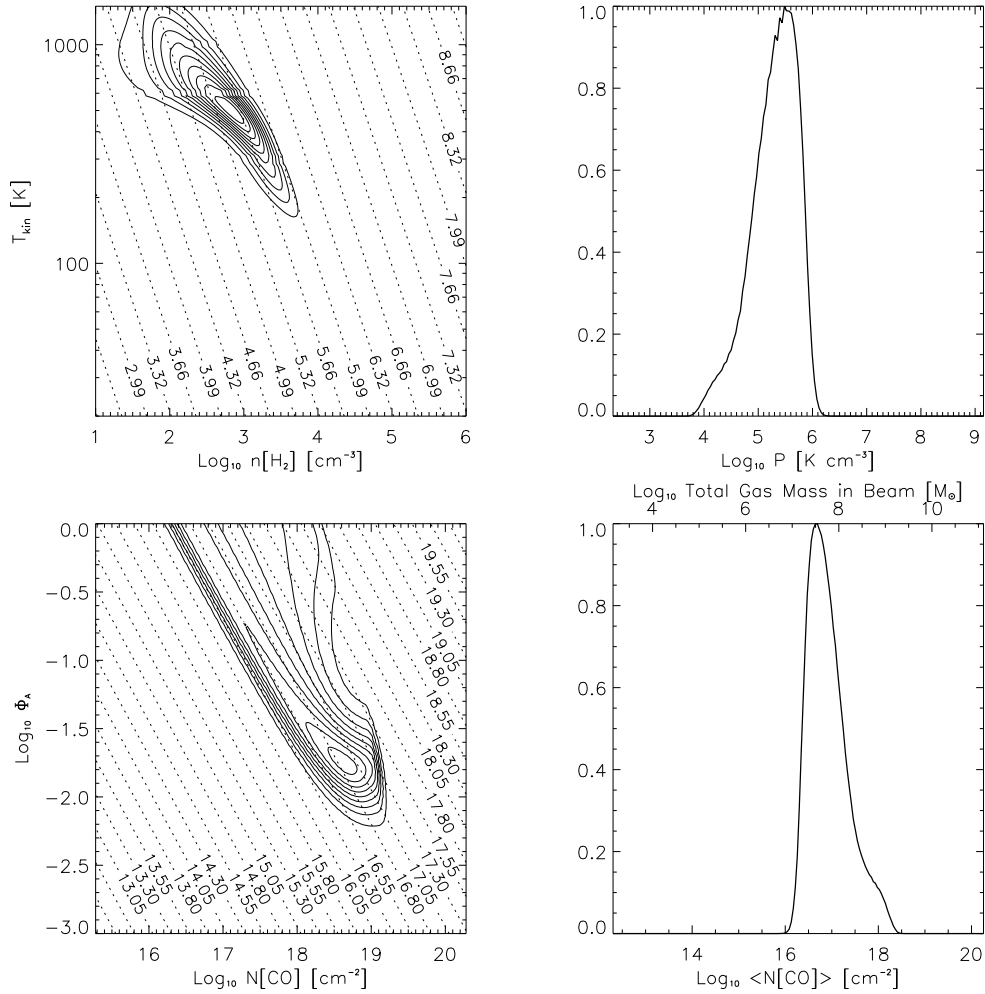


Figure 3.5: Normalized 1-D (*right*) and 2-D (*left*) likelihood distributions for the overlap region. The 2-D contour plots are for the kinetic temperature and gas density (*top left*), and filling factor and CO column density (*bottom left*). The 1-D distributions are for the pressure (*top right*) and beam average column density (*bottom right*). The dotted lines in the 2-D contour plots correspond to the pressure (*top left*) and the beam average column density (*bottom left*). The CO emission lines measured from the FTS SLW and the JCMT ($J = 3 - 2$ to $8 - 7$) were included in these calculations.

Table 3.4: Nucleus of NGC 4038: CO $J = 4 - 3$ to $8 - 7$

	1 Sigma Range	1D Max	4D Max	
T_{kin}	195 – 555	370	465	[K]
$n(\text{H}_2)$	$10^{1.53} - 10^{2.94}$	$10^{1.91}$	$10^{1.26}$	$[\text{cm}^{-3}]$
N_{co}	$10^{17.48} - 10^{18.86}$	$10^{18.75}$	$10^{19.10}$	$[\text{cm}^{-2}]$
Φ_{A}	$10^{-1.51} - 10^{-0.29}$	$10^{-0.58}$	$10^{-0.94}$	
P	$10^{4.02} - 10^{5.40}$	$10^{4.80}$	$10^{4.80}$	$[\text{K cm}^{-2}]$
$\langle N_{\text{co}} \rangle$	$10^{16.68} - 10^{18.14}$	$10^{17.62}$	$10^{17.62}$	$[\text{cm}^{-2}]$
Total Mass in Beam	$10^{7.18} - 10^{8.64}$	$10^{8.12}$	$10^{8.12}$	$[\text{M}_{\odot}]$

Table 3.5: Nucleus of NGC 4038: CO $J = 3 - 2$ to $8 - 7$

	1 Sigma Range	1D Max	4D Max	
T_{kin}	236 – 897	551	673	[K]
$n(\text{H}_2)$	$10^{2.01} - 10^{3.37}$	$10^{3.21}$	$10^{2.27}$	$[\text{cm}^{-3}]$
N_{co}	$10^{16.97} - 10^{18.83}$	$10^{18.87}$	$10^{18.78}$	$[\text{cm}^{-2}]$
Φ_{A}	$10^{-1.98} - 10^{-0.48}$	$10^{-1.88}$	$10^{-1.92}$	
P	$10^{4.90} - 10^{5.79}$	$10^{5.74}$	$10^{5.74}$	$[\text{K cm}^{-2}]$
$\langle N_{\text{co}} \rangle$	$10^{16.22} - 10^{17.02}$	$10^{16.28}$	$10^{16.28}$	$[\text{cm}^{-2}]$
Total Mass in Beam	$10^{6.72} - 10^{7.51}$	$10^{6.78}$	$10^{6.78}$	$[\text{M}_{\odot}]$

Table 3.6: Overlap region: CO $J = 4 - 3$ to $8 - 7$

	1 Sigma Range	1D Max	4D Max	
T_{kin}	298 – 844	506	601	[K]
$n(\text{H}_2)$	$10^{1.67} - 10^{3.29}$	$10^{2.47}$	$10^{1.26}$	$[\text{cm}^{-3}]$
N_{co}	$10^{17.17} - 10^{18.75}$	$10^{18.62}$	$10^{19.03}$	$[\text{cm}^{-2}]$
Φ_{A}	$10^{-1.75} - 10^{-0.28}$	$10^{-0.36}$	$10^{-0.86}$	
P	$10^{4.44} - 10^{5.87}$	$10^{5.48}$	$10^{5.48}$	$[\text{K cm}^{-2}]$
$\langle N_{\text{co}} \rangle$	$10^{16.29} - 10^{17.86}$	$10^{16.69}$	$10^{16.69}$	$[\text{cm}^{-2}]$
Total Mass in Beam	$10^{7.14} - 10^{8.71}$	$10^{7.54}$	$10^{7.54}$	$[\text{M}_{\odot}]$

Table 3.7: Overlap region: CO $J = 3 - 2$ to $8 - 7$

	1 Sigma Range	1D Max	4D Max	
T_{kin}	369 – 959	583	635	[K]
$n(\text{H}_2)$	$10^{1.91} - 10^{3.10}$	$10^{2.53}$	$10^{2.53}$	$[\text{cm}^{-3}]$
N_{co}	$10^{17.12} - 10^{18.61}$	$10^{18.05}$	$10^{18.53}$	$[\text{cm}^{-2}]$
Φ_{A}	$10^{-1.70} - 10^{-0.26}$	$10^{0.00}$	$10^{-1.70}$	
P	$10^{4.85} - 10^{5.69}$	$10^{5.48}$	$10^{5.48}$	$[\text{K cm}^{-2}]$
$\langle N_{\text{co}} \rangle$	$10^{16.49} - 10^{17.33}$	$10^{16.69}$	$10^{16.69}$	$[\text{cm}^{-2}]$
Total Mass in Beam	$10^{7.34} - 10^{8.18}$	$10^{7.54}$	$10^{7.54}$	$[\text{M}_{\odot}]$

Chapter 4

Discussion

In this Chapter, I discuss the integrated intensity maps created in Chapter 2, along with the observed CO distribution across the galaxy. I then discuss the RADEX results from Chapter 3. Of particular interest is the warm molecular gas found in my RADEX solutions. I will then investigate the possible heating mechanisms of the warm molecular gas.

4.1 Line intensity maps

The CO line intensity maps presented in Chapter 2 do not show any odd behaviour in the distribution of the CO emission across the galaxy, agreeing with previous single dish and interferometric observations of lower J CO lines, such as those of Wilson et al. (2003) or Zhu et al. (2003). With the exception of the $J = 4 - 3$ intensity map, the overlap region is brightest region in the entire galaxy. In the case of the $J = 4 - 3$ CO line, the pixel representing the nucleus of NGC 4038 is the brightest region.

In the overlap region, the measured CO SLED peaks at the $J = 3 - 2$ transition, with the intensity decreasing as the upper J increases. This is

fairly typical of a single component CO SLED; however it does not eliminate the possibility of multiple components (e.g. see Ward et al. (2003), Panuzzo et al. (2010)). In the nucleus of NGC 4038, the CO SLED appears similar to that of the overlap region, except that it peaks at the $J = 4 - 3$ transition, which is in agreement with Bayet et al. (2006). This could be due to the existence of multiple components of the molecular gas, such as a warm and a cool component (e.g. see Rangwala et al. 2011). Since the excitation temperature of CO transitions increases with J , the majority of the $J = 1 - 0$ to $J = 3 - 2$ emission would be from the cool component, while the majority of the $J = 5 - 4$ and higher CO emission would be from the warm component. Both components would contribute significantly to the $J = 4 - 3$ emission, leading to an apparent enhancement in its emission with respect to the other transitions.

4.2 Radiative transfer analysis

Using the radiative transfer code RADEX coupled with a likelihood code, I calculated the physical characteristics of both the overlap region and the nucleus of NGC 4038. The results of the analysis were presented in Section 3.3. In all 4 cases the CO SLEDs are fit best by the 4DMax solution, with the 1DMax solution significantly overestimating the intensities of all of the lines. This is not unexpected, as only the 4DMax produces a self-consistent solution across all of the parameters.

For both the overlap region and nucleus of NGC 4038, the $J = 4 - 3$ to $8 - 7$ solution overestimates the $J = 3 - 2$ line intensity significantly (see Figure 3.1).

In the nucleus of NGC 4038, the $J = 3 - 2$ to $8 - 7$ solution underestimates the $J = 4 - 3$ line flux. Finally, using the results of Zhu et al. (2003), I calculated an approximate CO $\frac{J=3-2}{J=1-0}$ line ratio across both the nucleus of NGC 4038 and the overlap region by averaging their line ratios across a $43.4''$ beam. For the nucleus of NGC 4038, I calculated a ratio of 0.62 ± 0.23 , which corresponds to an intensity of 29 ± 11 K km/s. For the overlap region, I calculated a ratio of 0.66 ± 0.28 , corresponding to an intensity of 44 ± 19 K km/s. In both cases, the $J = 4 - 3$ to $8 - 7$ solution over estimates the $1 - 0$ line intensity considerably, while the $J = 3 - 2$ to $J = 8 - 7$ solution underestimates it, evidence that neither solution is self consistent across the entire molecular region. The lack of a fully self-consistent solution is evidence that there are multiple components of the molecular gas, and not one uniform region. We would expect in such a situation that the bulk of the lower J CO emission is due to the cold molecular gas, while the higher J emission would originate directly from the warm component observed.

Both solutions for the nucleus suggest that there is warm, lower-density molecular gas. Since the excitation temperature of the highest observed J CO line ($8 - 7$) is ~ 199 K, finding warm molecular gas in the system is not surprising. Furthermore, both solutions suggest that the warm gas is $\sim 1 - 2$ orders of magnitude less dense than the cool molecular components from Zhu et al. (2003) ($3.5 \times 10^3 \text{ cm}^{-3}$) or Bayet et al. (2006) ($3.5 \times 10^5 \text{ cm}^{-3}$). Similarly, both solutions in the overlap region suggest that there is warmer, lower-density molecular gas than found by Zhu et al. (2003). In particular, the density of our warm component is once again $\sim 1 - 2$ orders of magnitude less than the cool gas modelled by Zhu et al. (2003) ($\sim 3.0 \times 10^3 \text{ cm}^{-3}$). In comparison, Bayet

et al. (2006) model a warmer component $T_{kin} = 145$ K, but their density is higher than Zhu et al. (2003) and orders higher than ours ($8.0 \times 10^3 \text{ cm}^{-3}$).

The comparison of our warm component to previously modelled cool components is in contrast to the two-component model of the overlap region by Zhu et al. (2003), as they found that the warmer component corresponds to the dense gas. Similarly, two-component radiative transfer models using CO lines across the entire FTS band of the ULIRG Arp 220 found that their warm component also corresponds to the denser gas, however to a lesser extreme (Rangwala et al., 2011). It is not uncommon, however, to find that the warm component is less dense than the cool component (e.g. see Ward et al. 2003; Schulz et al. 2001). Further investigation into this discrepancy would be possible by including $J = 2 - 1$ and $J = 1 - 0$ data into our LVG analysis, as this would increase our line total to 8 lines. Furthermore, ^{13}CO transitions could also be included in conjunction with ^{12}CO transitions to further increase the number of lines in the analysis. With 8 or more lines, it would be possible to perform a two-component fit to our CO SLED; one for the cool component, the other for the warm. Especially in the case of the nucleus of NGC 4038, where the $J = 4 - 3$ is the brightest line in our set, it would possible to determine the total contributions from both the cool and warm components to the overall intensity of each line, including the aforementioned CO $J = 4 - 3$ line.

4.3 Heating mechanism

For there to be a warm component to the molecular gas, there must be accompanying heating processes to increase the temperature of the cool molecu-

lar gas. Typically, the gas is heated by one (or more) of four different processes: heating by x-ray photons, heating by UV photons, heating by cosmic rays and finally mechanical heating. Here, I discuss the possible heating mechanisms in both the nucleus of NGC 4038 and the overlap region of the Antennae.

4.3.1 X-ray dominated regions

X-ray dominated regions (XDRs) are regions in which the primary mechanism for heating is the absorption of x-ray photons by the molecular gas. In both the nucleus of NGC 4038 and the overlap region, it is highly unlikely that the heating is occurring in an XDR for a number of reasons. First, XDRs require an x-ray source, such as an active galactic nucleus (AGN), supernova remnants or shocks, or embedded massive stars (Maloney et al., 1996). While there does exist strong x-ray emission in the two nuclei due in large part to x-ray emitting black hole binaries (Fabbiano et al., 2001), there is no published evidence for an AGN in either nucleus. Moreover, the x-ray emission in the overlap region is weak, suggesting few x-ray sources.

Secondly, in XDRs, the higher J CO lines are typically stronger in intensity than we have observed (Meijerink et al., 2007). If there were a strong XDR, we would expect to observe the intensity of CO to increase with J , possibly up to $J = 8 - 7$ (van der Werf & Spaans, 2009). In the overlap region, the CO emission peaks either with the $J = 3 - 2$ line, or with one of the two lower, unobserved lines, none of which would suggest an XDR. In the nucleus, the emission peaks with the $J = 4 - 3$ line within our set of lines, but it is far more likely that the emission peaks with either the $2 - 1$ line (Schulz et al., 2007) or

the $1 - 0$ line (Zhu et al., 2003). Regardless, there is no evidence for an XDR, or for x-rays to be the dominant form of heating in either the nucleus of NGC 4038 or the overlap region.

4.3.2 Photodissociation regions

Photodissociation regions (PDRs), or photon-dominated regions, are regions illuminated by strong FUV emission with energies ranging from $6 \text{ eV} \leq h\nu < 13.6 \text{ eV}$, below the energy required to ionize the neutral HI (Tielens & Hollenbach, 1985). Typically, this FUV radiation originates from the OB stars in massive star forming regions (Wolfire, 2010), and can have a profound impact on the heating and chemistry of the surrounding regions. PDRs are not uniform clouds of gas, with the state and chemistry of the gas dependent upon the depth; in the shallower regions of the clouds ($A_V \lesssim 8$), FUV radiation prevents any O not already tied up in CO from combining with C to form the molecule.

There have been numerous attempts at modelling PDRs in various galaxies (e.g. see Rangwala et al. 2011 or Mao et al. 2000b). While LVG models dependent on there being a constant temperature for each component modelled, PDR models rely on a temperature gradient to calculate the theoretical CO fluxes, and as such will calculate different CO fluxes. Schulz et al. (2007) analyzed the possibility of PDRs in both nuclei of the Antennae along with the overlap region by modelling the $J = 1 - 0$ to $J = 3 - 2$ ^{12}CO and $J = 1 - 0$ to $J = 2 - 1$ ^{13}CO transitions with a PDR model. Beyond fitting these lines, they also predicted a $\frac{4-3}{1-0}$ ratio of $0.2 - 0.3$ across the overlap region. If we

assume the previously calculated $\frac{3-2}{1-0} = 0.66 \pm 0.28$ from Zhu et al. (2003), and calculate $\frac{4-3}{3-2} = 0.60 \pm 0.06$ from our 3 – 2 and 4 – 3 data, we can approximate a $\frac{4-3}{1-0}$ ratio of 0.40 ± 0.17 . While there are large uncertainties associated with this value, it does not fall inside the range calculate by Schulz et al. (2007) and as such, it is unlikely that the PDR model calculated by Schulz et al. (2007) represents the true physical and chemical state of the molecular gas.

There is still widespread evidence for PDRs being a significant source of heating in the overlap region of NGC 4038. Particularly, there, the previously observed young massive star clusters (Whitmore et al., 1999) would contain OB stars to produce the necessary FUV emission for PDRs (Schulz et al., 2007). Beyond the existence of such a source, observations of CII emission (Nikola et al., 1998), the near infrared spectrum (Gilbert et al., 2000), and hot dust (Schulz et al., 2007) all provide evidence for the existence of PDRs across the Antennae. Future modelling using all available CO transitions will be necessary to confirm whether PDRs are the primary source of heating, and to determine the physical and chemical properties of such regions.

4.3.3 Cosmic rays

Along with PDRs, Schulz et al. (2007) investigated whether cosmic rays could be a dominant source of heating in the Antennae. They find that, at least in the overlap region, the effects of cosmic rays on the SGMs in this region is difficult to determine, and that cosmic rays are unlikely to be the primary source of heating. No new conclusions can be made in regards to cosmic ray heating from our data.

4.3.4 Mechanical heating

Mechanical heating is typically assumed to either be due to turbulent heating (e.g. see Bradford et al. 2005) or supernovae and stellar winds (e.g. see Maloney 1999). Since the Antennae is an ongoing merger, we expect a certain amount of heating due to turbulent velocities, especially in the overlap region. This does not necessarily imply that turbulent motion is a significant contributor to the overall heating inside of the system. It is possible to calculate the contributions from the turbulent motions to the overall heating of the galaxy by considering the energy injected into the system by the turbulent material. The energy output, and as such injected into the system, by the turbulent motion per unit mass can be calculated from the following equation (Bradford et al., 2005)

$$\frac{L}{M} = 1.10 \left(\frac{v_{rms}}{25 \text{ km s}^{-1}} \right)^3 \left(\frac{1 \text{ pc}}{\Lambda_d} \right) \frac{L_\odot}{M_\odot} \quad (4.1)$$

where v_{rms} is the turbulent velocity and Λ_d is the size scale. While the likelihood code is able to output a velocity gradient, the accuracy of the calculated value is uncertain. We can approximate the maximum turbulent energy from the v_{FWHM} and D from Wilson et al. (2000). If we use the values for the nucleus of NGC 4038, we would obtain a turbulent heating rate of $\sim 0.011L_\odot/M_\odot$. The total observed CO and CII cooling rates in the nucleus of NGC 4038, which are the dominant coolants of the molecular gas, are $\sim 0.003 \pm 0.001L_\odot/M_\odot$ (Bayet et al., 2006) and $\sim 0.066 \pm 0.023L_\odot/M_\odot$ (Nikola et al., 1998) respectively, corresponding to a total cooling rate of $\sim 0.069 \pm 0.023L_\odot/M_\odot$. While the total cooling rate could account for the

turbulent energy injected into the system, it is likely that turbulent energy plays a role in the overall heating of the nucleus of NGC 4038.

In the overlap region, the turbulent heating is approximated by summing up the turbulent heating in the 5 SMGCs in Wilson et al. (2000), yielding a turbulent heating of $\sim 0.07 L_{\odot}/M_{\odot}$. The CO and CII cooling rates in the overlap region are $\sim 0.002 \pm 0.001 L_{\odot}/M_{\odot}$ (Bayet et al., 2006) and $\sim 0.061 \pm 0.020 L_{\odot}/M_{\odot}$ (Nikola et al., 1998) respectively, corresponding to an overall cooling rate of $\sim 0.062 \pm 0.020 L_{\odot}/M_{\odot}$. Since the turbulent heating rate is higher than the overall cooling rate, turbulent heating is contributing to the overall heating of the molecular gas in the overlap region.

The heating rate due to supernova and stellar winds can be calculated using the following equation from Maloney (1999)

$$L_{SN} \sim 3 \times 10^{43} \left(\frac{\nu_{SN}}{1 \text{ yr}^{-1}} \right) \left(\frac{E_{SN}}{10^{51} \text{ erg}} \right) \text{ erg s}^{-1} \quad (4.2)$$

where ν_{SN} is the supernova rate and E_{SN} is the energy released per supernova (10^{51} erg). In the Antennae, the observed global supernova rate is $\nu_{SN} \sim 0.2 - 0.3 \text{ yr}^{-1}$ (Neff & Ulvestad, 2000). There would be a total of $\sim 1.6 \times 10^9 - 2.3 \times 10^9 L_{\odot}$ mechanical energy due to supernovae across the entire galaxy. Assuming that the contribution from stellar winds is similar (Rangwala et al., 2011), the total heating rate from supernova and stellar winds can be approximated to $\sim 3.2 \times 10^9 - 4.6 \times 10^9 L_{\odot}$. The total CII cooling rate across the entire galaxy is $\sim (5.2 \pm 1.6) \times 10^8 L_{\odot}$ (Nikola et al., 1998), while the CO cooling rate from the nucleus of NGC 4038 and the overlap region is $(8.9 \pm 2.7) \times 10^6 L_{\odot}$ (Bayet et al., 2006), which, since NGC 4039 is not as bright as either region, only

slightly underestimates the total CO cooling. Hence, the total cooling rate is $\sim (5.2 \pm 1.6) \times 10^8 L_{\odot}$. The supernova and stellar wind heating is enough to compensate for this cooling rate and therefore, supernova and stellar wind heating is likely to contribute to the overall heating across the entire galaxy, and may be the dominant source of heating throughout the galaxy.

Chapter 5

Conclusion and Future Work

5.1 Conclusions

In this study, I describe the use of CO emission to model the physical parameters in the molecular gas of the Antennae system (NGC 4038/39). I accomplish this using observations from the *Herschel* SPIRE FTS coupled with data from the JCMT HARP instrument and the radiative transfer code RADEX. In this chapter, I present conclusions reached from this study.

1. In the short wavelength spectral range ($194 - 313 \mu\text{m}$), I detected CO emission from the $J = 4 - 3$ transition to the $J = 8 - 7$ transition and both [CI] transitions in numerous pixels across the entire system, including the nucleus of NGC 4038 and the overlap region. Emission from the nucleus of NGC 4039 is blended with the emission from the overlap region due to the very large beam size ($43.4''$). In the SSW, I detected only the [NII] transition at ~ 1460 GHz in numerous pixels across the system. None of the CO lines in the long wavelength spectral range ($303 - 671 \mu\text{m}$) were detected.

2. Integrated intensity maps for the $J = 4 - 3$ to $8 - 7$ CO transitions were constructed by fitting the respective emission lines with sinc functions across the entire SPIRE FTS spectral cube, and convolving them to match the beam sizes and shapes. These observations were supplemented with CO $J = 3 - 2$ observations from the JCMT. I found that for the $J = 5 - 4$ to $8 - 7$ transitions, the brightest emission is in the overlap region, as seen in previous studies on lower J transitions (e.g. Wilson et al. 2003; Zhu et al. 2003; Schulz et al. 2007). The brighter $J = 4 - 3$ transition in the nucleus of NGC 4038 is indicative of multiple components of the molecular gas, such as a warm, low density and a cool, denser component.
3. The CO emission was modelled using the radiative transfer code RADEX and a Bayesian likelihood code in a single pixel for both the nucleus of NGC 4038 and the overlap region. Two different cases were runs for both sets of CO lines: one including all CO lines available to us ($J = 3 - 2$ to $8 - 7$), a second excluding the JCMT data ($J = 4 - 3$ to $8 - 7$). For both the nucleus of NGC 4038 and the overlap region, the second case was found to significantly overestimate the emission of the lower ($1 - 0$ and $3 - 2$) transitions, while the first case underestimates the intensity of the $1 - 0$ transition.
4. In the nucleus of NGC 4038 we find that there is a warm ($T_{kin} > 600$ K), low-density ($n(\text{H}_2) \sim 200 \text{ cm}^{-3}$) component of the molecular gas. This component is both warmer and less dense than any previously observed component. The molecular gas mass of our warm com-

ponent is $\sim 6 \times 10^6 M_{\odot}$, corresponding to $< 1\%$ of the mass of Zhu et al. (2003)'s cool single component. In the overlap region we find a similar warm ($T_{kin} > 600$ K), low density ($n(\text{H}_2) \sim 300 \text{ cm}^{-3}$) component. The molecular gas mass in the overlap region of our warm component is $\sim 3.5 \times 10^7 M_{\odot}$, which is about $\sim 1\%$ of the total molecular gas mass of the cool component in Zhu et al. (2003).

5. There is widespread evidence of there being multiple components of molecular gas throughout the galaxy, such as the brighter $4 - 3$ line in the nucleus of NGC 4038, the overestimation of the $J = 3 - 2$ and $1 - 0$ flux in the model which includes only the $J = 4 - 3$ to $8 - 7$ transitions, the underestimation of the $J = 1 - 0$ flux in the $J = 3 - 2$ to $8 - 7$ model and the vastly warmer temperatures than found in previous studies (e.g. Zhu et al. 2003; Bayet et al. 2006). It is highly probable that there is both a cool component and warm component as in M82 (Panuzzo et al., 2010); however the complex structure of the overlap region may require a 3 or more component fit when ^{13}CO lines are included in the analysis.
6. In both the nucleus of NGC 4038 and the overlap region, I find that x-ray dominated regions, cosmic rays and turbulent heating are likely not the primary sources of heating. I also find that supernova and stellar winds are strong contributors to the overall heating of the galaxy, and may be the dominant source of heating. Finally, there is evidence that photodissociation regions *may* be the primary source of heating in both the overlap region and nucleus of NGC 4038. photodissociation region modelling of our CO spectral line energy distribution will be necessarily

to determine whether photodissociation regions are the dominant source of heating in either (or both) the nucleus of NGC 4038 and the overlap region.

5.2 Future Work

I intend to continue my work on the Antennae by supplementing my current data set with both previous and future observations. Below is a comprehensive, but not exhaustive, list of my planned future work on this source.

1. I plan to continue reducing the data with the latest reduction scripts to further decrease the calibration and fitting random errors. I will then search the SSW of these latest reductions for higher J CO transitions, if they exist.
2. I will identify any unidentified transitions throughout the spectra of the entire system.
3. I will hopefully obtain single dish integrated intensity maps for the lower CO transitions ($1 - 0$ and $2 - 1$), along with any ^{13}CO transitions for which such maps are available (e.g. the $1 - 0$ and $2 - 1$ transitions).
4. I plan to continue my work on radiative transfer modelling by performing the radiative transfer analysis using all ^{12}CO transitions from $J = 1 - 0$ to $J = 8 - 7$, along with any available ^{13}CO transitions across the entire system with both a single component and two component fit.

5. I intend to investigate the use of PDRs as the primary source of heating further by computing PDR models using all available CO lines. This analysis could be accomplished using the same method used in Rangwala et al. (2011), which involves comparing CO line ratios to those calculated by PDR models.
6. Using the same tools, I can perform a similar analysis on more galaxies in our sample and for any galaxies for which the FTS data is public.
7. We have submitted an ALMA proposal to map dense gas throughout the system using the dense gas tracers HCN and HCO⁺. These maps are likely to be useful to determine where dense gas clouds are found throughout the system, and can also be used as a star formation tracer throughout the system.

Appendix A

Data Reduction

FTS observations are available in already reduced form from the Herschel Science Archive; however the pipeline used to reduce these data is not the best and most up to date pipeline, nor has it used the most recent calibration context. Users can download the data and reduce it themselves using any number of scripts provided with the Herschel Processing Environment (HIPE), along with the most recent "calibration context". By using the latest developers build as opposed to the public release of HIPE, we have reduced my data using the very latest pipeline (HIPE version 8.0, build 929) along with the latest calibration context (SPIRE calibration version 7.0). In this chapter, we will outline the reduction process used to reduce the data for NGC 4038. Further details on each of the various tasks and modules can be found in the SPIRE Data Reduction Guide (SPI, 2011a) or the SPIRE Observers Manual (SPI, 2011c). The script used to reprocess these FTS observations is included with every version of HIPE with only minor modifications required for use. Unless otherwise stated, the reduction process outlined in this appendix is the same as in the Spectrometer Mapping User's Script.

A.1 User defined parameters

The user reduction scripts are written to ensure that the average user needs to edit as little of the script as possible. This is to guarantee that the average user is able to quickly and efficiently re-reduce their "observation contexts" if necessary. All modifications required by the user are done in the *User Defined Parameters* section of the script. The user defined parameters for the mapping script include the observation ID, the observation data pool, whether or not the user wishes to apodize the spectrum, the directory in which the resulting data cubes will be saved, and the map pixel size.

A.2 Load observation context

SPIRE FTS data is stored locally inside HIPE in "pools". Both of our observations (one centred on the nucleus of NGC 4038, the other on the overlap region) are stored in separate data pools, and are reduced to Level 1 spectra individually before being combined into a single level 2 data cube. The observation to be reduced is loaded using the *getObservation* task. This task requires both the observation ID and the data pool name as input, and outputs the entire observation context into a single HIPE variable. All of the data relevant to the observation itself is stored in the observation context, including the calibration and auxiliary contexts. If the observation pool was obtained from the Herschel Science Archive, the calibration products attached to the observation context will not be the most up to date calibrations.

A.3 Load calibration and auxiliary products

Observations downloaded from the Herschel Science Archive do not contain the latest calibration context. The most up-to-date calibration context is stored on the local hard disk (SPIRE calibration 7.0), and is loaded using the *spireCal* task. The latest calibration context is attached to the observation context and the calibration products necessary for reducing the data are extracted from the context.

Calibration data unique to the observation are stored as part of the observation context in the form of auxiliary products and the necessary auxiliary products are extracted from the observation context: the Herschel Pointing Product (HPP), the Spacecraft Instrument Alignment Matrix (SIAM) and the Herschel Housekeeping Product (HK). The HPP and SIAM contain information relevant to the pointing of the spacecraft, while the HK contains the telescope temperature timelines necessary for the removal of the telescope's contribution from the overall measured emission.

A.4 Process Level 0.5 observation

The observation context is made up of Spectrometer Mechanism (SPEC) scan building blocks, each of which accounts for a single jiggle position on the sky, giving a total of 16 building blocks for a fully sampled observation corresponding to the 16 jiggle positions. Each building block is processed individually, in part to limit the computer memory required, and each is processed in the same manner. To begin, the Spectrometer Detector Timeline (SDT), Nominal House Keeping Timeline (NHKT), Spectrometer Mechanism Time-

line (SMECT) and Beam Steering Mechanism Timeline (BSMT) are extracted from the observation context.

The SDT contains the various measurements record by all the detectors, and it contains the data for all scans at a single jiggle position. Since no assumption is made about the linearity or speed of the central mirror as it moves along its track, the time at which each measurement is recorded is stored in the SMECT. The NHKT contains various products related to the housekeeping of the telescope, such as the start and end positions of the Spectrometer Mechanism (SMEC) for the various scans. Finally, the BSMT contains the raw data on the beam steering mirror, which is required to calculate the position of each detector at each jiggle position in world coordinates.

A.4.1 First level deglitching

First level deglitching is done early in the data reduction process to remove the effects of high energy cosmic rays hitting the detectors, which are the primary culprit in producing glitches in the detectors. First level deglitching is done using the *waveletDeglitcher* task, which uses a wavelet method for detecting and removing glitches. The task requires as input the SDT, and will output a deglitched SDT. This module operates on the SDT for each detector individually. As it uses both the SDT as input and output, it operates in the voltage-time domain. It works by first detecting glitches in the SDT. When a glitch is found, it will repair and reconstruct the signal around the glitch. It is necessary to reconstruct any gaps in the signal in order to perform the proper Fourier transform on the interferogram later in the data reduction process.

There are numerous optional parameters which can be set by the user; we do not alter the parameters from the script. In order to not damage the centre burst (i.e. see figure A.1) during the deglitching process, the parameters used by the script are conservative. As such, some smaller glitches may be missed during this first deglitching process, but may be caught by a second deglitching process later in the pipeline.

A.4.2 Non-linearity and temperature drift correction

The next step is to correct for the non-linear response of the bolometric detectors and the temperature of the bolometric detectors, with the former being performed first. The *specNonLinearityCorrection* task is used for the non-linearity correction. The *specNonLinearityCorrection* task operates on the SDT in voltage-time space. The linearized voltage is calculated for each detector using the formula

$$V_{linearized} = K_1 * (V - V_o) + K_2 * \ln(V - K_3) - K_2 * \ln(V_o - K_3) \quad (\text{A.1})$$

where the values for the constant parameters (V_o , K_1 , K_2 , and K_3) are stored in the calibration product under calibration product `SCalSpecNonLinCorr`, and are unique for each detector. The only user defined parameter is the version of `SCalSpecNonLinCorr`, which was taken from the SPIRE Calibration Product version 7.0 for my reductions.

The *temperatureDriftCorrection* task is used to correct for the temperature drift. The thermistors are used in conjunction with the calibration product `tempDriftCorr` to determine the effects of the operating temperature on the

bolometric responses. The effect is determined from empirical calculations of the relations between the thermistors and the detectors. The user can define a smoothing timespan, for which the default value of 5 seconds was used in my reduction. As the thermistors are no longer required after this step, they are removed from the SDT in order to conserve memory, as the reduction process can consume a significant amount of memory. The thermistors and resistors are all removed using the *filterChannels* task, from which we recover a slimmer SDT.

A.4.3 Clipping correction

Clipping can occur when observing a bright source, causing local extrema in the SDT in the signal to become clipped. This saturation can be corrected using the *clippingCorrection* task. It requires only the SDT as input, and it outputs a corrected SDT. When a clip is detected, an 8th degree polynomial is fitted to the 5 points before the clip and 5 points after the clip. The user can change the number of points before and after to which the 8th degree polynomial is fit to an integer between 3 and 10; however we use the default number of 5.

A.4.4 Time domain phase correction

There is a time delay and slight distortion in the thermal response of the detectors and read-out electronics which must be accounted for. This phase shift is characterized by comparing the forward and reverse scans, and is cor-

rected for using the *timeDomainPhaseCorrection* task. It requires as input the SDT, and will output a phase corrected SDT. The NHKT, which contains the telemetry parameters, can also be input but is not required. Finally, two calibration products are required as input: the Spectrometer Low Pass Filter Parameters and the Spectrometer Detector Time Constants. The Phase Correction Limits can also be input as a calibration product.

A.4.5 Add pointing information

Where a given detector is pointing on the sky is dependent upon three factors and all of these factors must be accounted for when calculating the pointing information. The three factors are where the telescope is pointing, the angular offset due to the location of the detector in the bolometric array, and the angular offset due to the beam steering mirror. First, we determine the offset due to the beam steering mirror (BSM) using the *calcBsmAngles* task. Either the BSMT or NHKT is used as input, where we use the BSMT as input. The BSM position table from the calibration context is also required, as it contains the necessary conversion factors from the raw input provided by the BSMT to the angular offset on the sky. Both contain the necessary time samples and corresponding BSM sensor signals required to calculate the angular offset. The output is the BSM angles timeline (BAT), which contains the BSM angular offset with respect to time.

Following the calculation of the BAT data product, a SPIRE Pointing product (SPP) is created to store the pointing information. The inputs are the Herschel Pointing Product (HPP), the Spacecraft Instrument Alignment

Matrix (SIAM), and the previously calculated BAT. The HPP contains the necessary pointing data for the telescope itself, while the SIAM contains the angular offsets between the Herschel line-of-sight and the SPIRE spectrometer apertures. The Detector Angular Offset calibration product is also required as input, and contains the detector offset data relevant for the non-central detectors. The total angular offset is calculated by adding the HPP, SIAM and detector angle offset and subtracting the BAT for each detector. The resulting SPP contains the pointing for each detector for the current jiggle position.

A.4.6 Create interferogram

After the SPP has been created, we can then combine it with the SMECT and the SDT to form an interferogram, using the *creatIfgm* task. The task requires both the SDT and SMECT as input, along with the SPP which contains the necessary pointing information for each detector. The NHKT, which contains the necessary housekeeping products for the SMEC while it is scanning, is also required as input. We also pass 3 calibration products to the task: the Zero Path Difference, the Spectrometer Channel Time Offset, and the Optical Encoder to Optical Path Difference.

There are two major steps to the creation of the interferogram. The SMECT is inherently non-uniform in position, and the first step is to interpolate it so that it is uniform in position to match the SDT. Secondly, the SDT and SMECT are merged together to create an interferogram for each scan of each pixel. The resulting data product is the Spectrometer Detector

Interferogram (SDI), which will be in units of Volts and centimetres. This is also called a Level 1 Interferogram (i.e. figures A.1 and A.2).

A.5 Process Level 1 Interferogram

A.5.1 Adjust optical path difference ranges

The interferograms may require truncation depending upon the resolution of the observation, so that all of the interferograms are of the same length, and as such the same commanded resolution. This is done using the *makeSameOpds* task. The SDI is the input, and a truncated SDI is output. We input the OPD limits as a calibration product, which specified the OPD ranges for each resolution. The length of the interferograms is dependent on the resolution of the observation; higher resolution observations will have longer interferograms.

A.5.2 Interferogram baseline correction

Before further corrections can be applied, the interferogram baseline must be removed as it is dependent upon the system temperature at the time of the scan. Removal of the baseline prior to applying the Fourier transform on the interferogram also reduces the amount of spectral artifacts introduced into the spectrum. The baseline itself generally has close to a quadratic shape due to vignetted effects. The baseline removal is done using the *baselineCorrection* task, which will either fit a polynomial to the interferogram baseline and

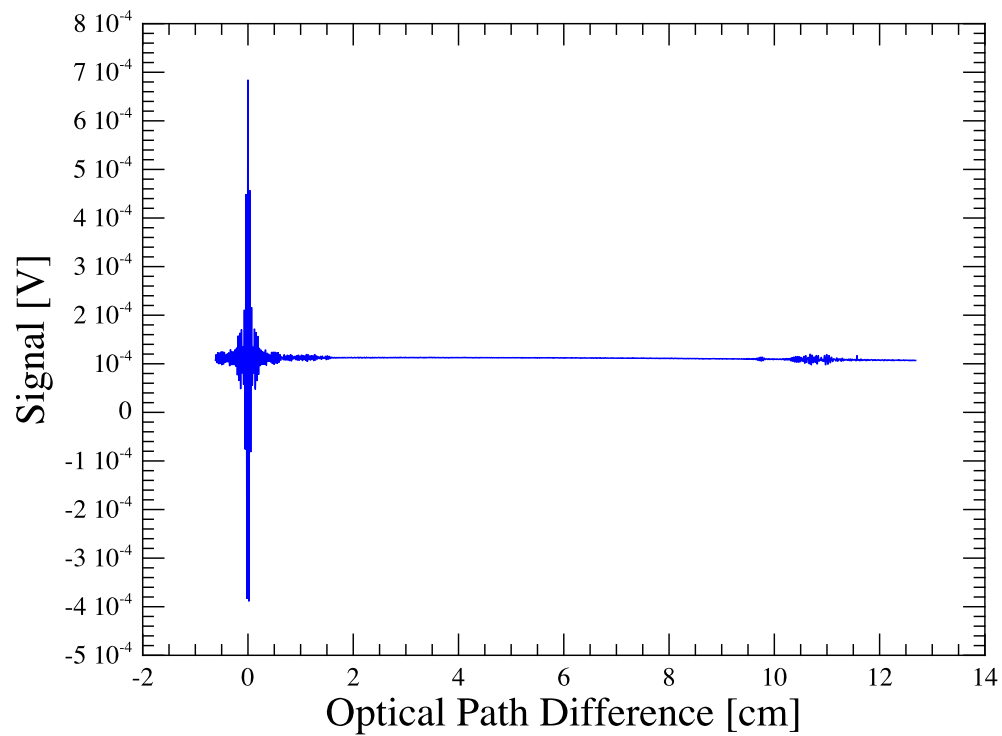


Figure A.1: Example interferogram taken from the reduction of the observation of the nucleus of NGC 4038. This interferogram has had no corrections applied to it. Note that the centre burst is not located in the centre of the interferogram, and that the baseline is non-zero.

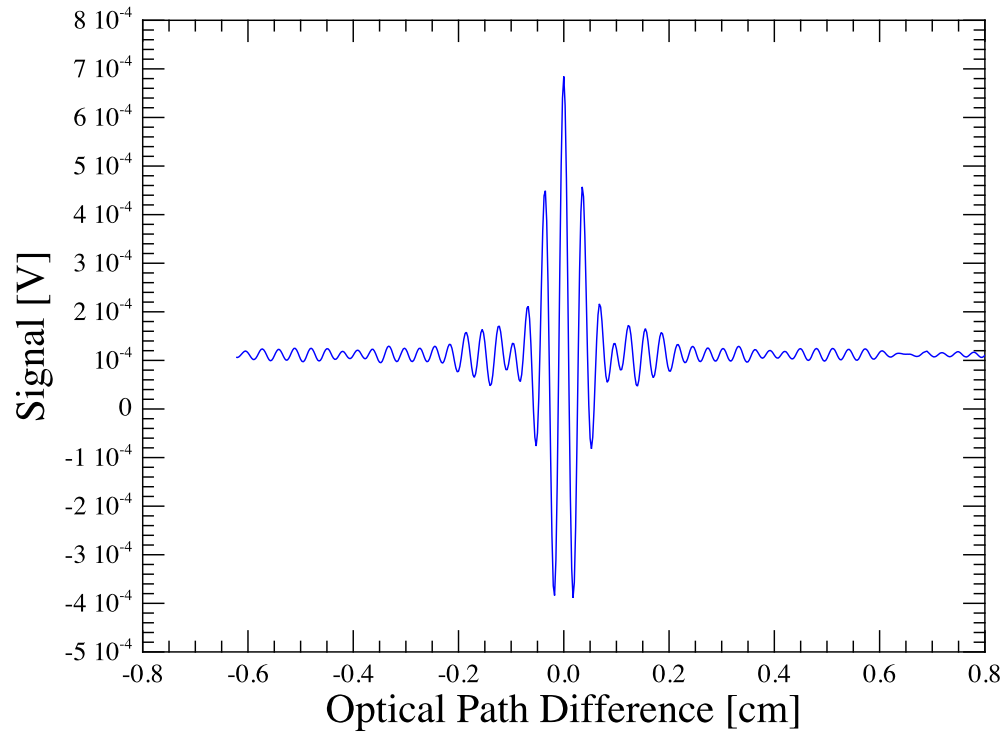


Figure A.2: Zoom in around centre burst of the same interferogram in figure A.1.

subtract or apply a Fourier filtering method. Fourier filtering is the default option, and is what we have used for our data reduction. Sinc-like artefacts may be introduced when using the Fourier filtering option, but many, if not all, of these artefacts will be removed with second level deglitching. The *baselineCorrection* task requires as input the SDI, and will output a baseline subtracted SDI. We have used Fourier filtering as our method of baseline subtraction with a threshold of 4 cm^{-1} . The input and output SDI can be seen in figure A.3.

A.5.3 Second level deglitching

FTS observations consist of multiple forwards and backwards scans, each representing the mirror moving from one end of its track to the other. Second level deglitching assumes that, for a given detector and jiggle position, each scan should be identical. We use the *deglitchIfgm* task to apply the 2nd level deglitching to our interferograms. The SDI is used as input, and a deglitched SDI is output, with no calibration products required as input. The standard approach used by the task is to determine outliers from the median of the spectral data in each scan, which is what we do for our reduction. Even though the "windowed" mode of detecting glitches tends to perform better for observations with few scans (2 to 10), it has issues identifying glitches which have been smeared out. The Fourier filtering method of baseline removal, which we have previously used in our reduction, has a tendency to smear out glitches, which is why we opt to use the standard standard deglitching option.

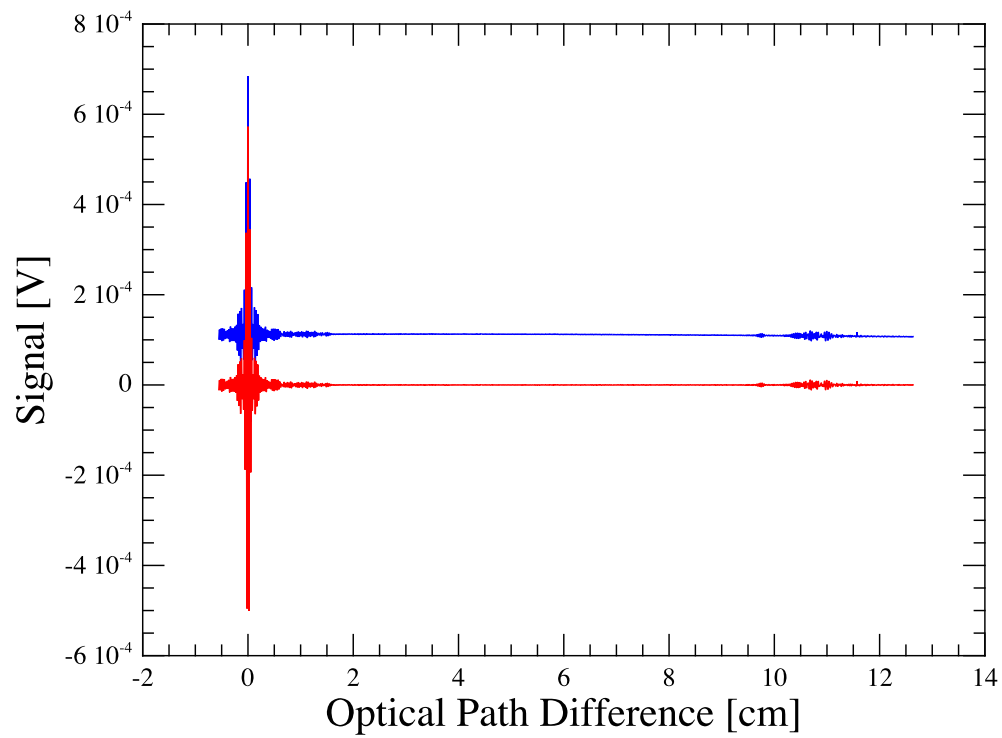


Figure A.3: Spectrometer Detector Interferogram before (*blue line*) and after (*red line*) interferogram baseline correction. The interferograms are from the reduction of the nucleus of NGC 4038.

A.5.4 Interferogram Phase Correction

A phase correction must be applied to the interferogram to correct for asymmetries in the interferogram, since these asymmetries can have damaging effects on the spectrum after the Fourier transform is applied to the interferogram. The correction itself requires numerous steps to process. First, a copy of the SDI is averaged over all the scans with the *averageInterferogram* task. This averaged interferogram is used strictly for calculating and applying the phase correction, and the correction itself is applied to the original SDI. The *averageInterferogram* task takes an SDI with multiple scans as input, and outputs an SDI with only one interferogram; the average of the input SDI scans. The averaged SDI is converted to a low resolution SDI by truncating the interferogram using the *makeSameOpds* as done previously for all of our interferograms. This low resolution SDI is double-sided, and should theoretically be symmetric about the zero-path difference. This symmetry is required for calculating the phase difference. A *SpectrometerDetectorSpectrum* is created to store the phase corrected spectrum (not interferogram).

Next, the phase correction is applied to the original SDI using the *phaseCorrection* task. This task calculates the phase correction from the low resolution averaged SDI and then applies the correction to the SDI in the spectral domain. Both the SDI and the low resolution averaged SDI previously calculated are used as input. Output are the phase corrected SDI along with a low resolution Spectrometer Detector Spectrum (SDS). The phase corrected and uncorrected SDIs can be seen in figure A.4.

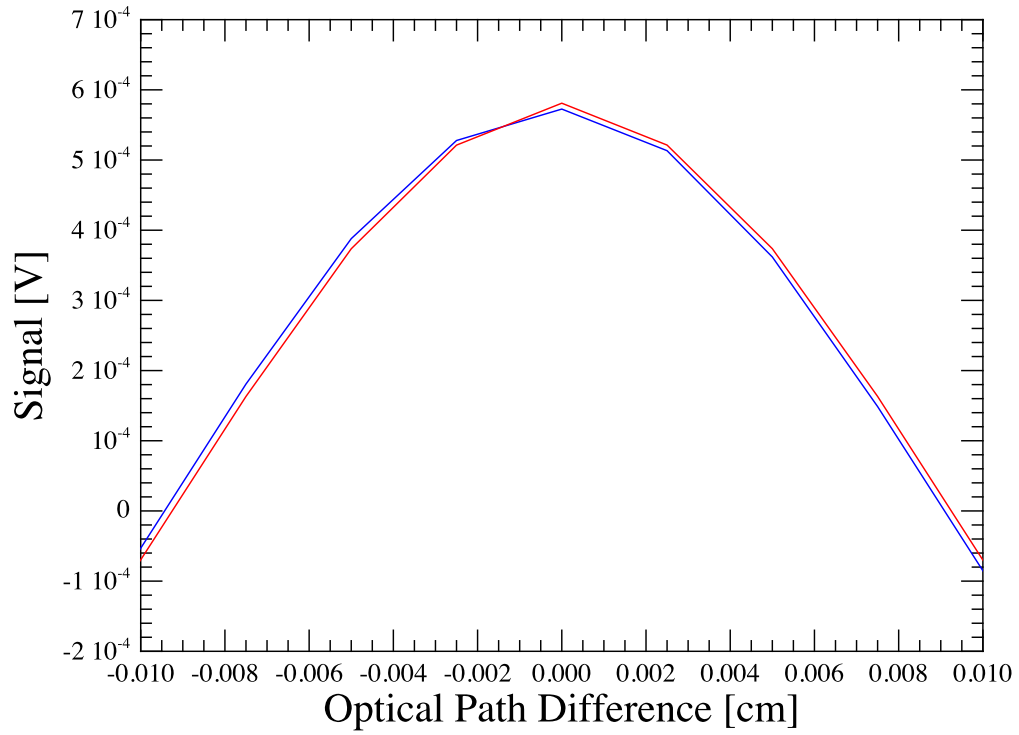


Figure A.4: Zoom in on centre burst of Spectrometer Detector Interferogram before (*blue line*) and after (*red line*) interferogram phase correction. The interferograms are from the reduction of the nucleus of NGC 4038. Notice that in this particular case, very little phase correction is required.

At this point, if one so chooses, the *apodizeIfgm* task can be applied to the interferogram to produce an apodized spectrum when the Fourier transform is applied. We do not apodize our spectrum, preferring to work with the unapodized spectrum. We apply the Fourier transform to the interferogram using the aptly named *fourierTransform* task. It only has the processed SDI as input, and in our case outputs a high resolution SDS. There are two parameters for the *fourierTransform* task; their type is determined by when the phase correction is applied. Since the phase correction was applied before the Fourier transform, we run the task in *postPhaseCorr* mode. In this mode, only the portion of the interferogram which is greater than the zero-path difference is used to compute the SDS (as opposed to the entire interferogram in *prePhaseCorr* mode). The second option is whether or not to zero-pad the interferogram prior to the Fourier transform. For our reduction, this option is set to *none*, and thus we do not zero-pad the interferogram. The resulting SDS will be in units of $V \cdot \text{cm}$ and cm^{-1} , and can be seen in figure A.5.

A.6 Process Level 1 Spectra

A.6.1 Removal of out of band data

The resulting SDS will include data points which extend beyond the frequency range of the FTS. These data points are generally approximately equal to (or very close to!) zero, and do not represent real data. We remove these data points using the *removeOutOfBand* task, which requires the SDS as in-

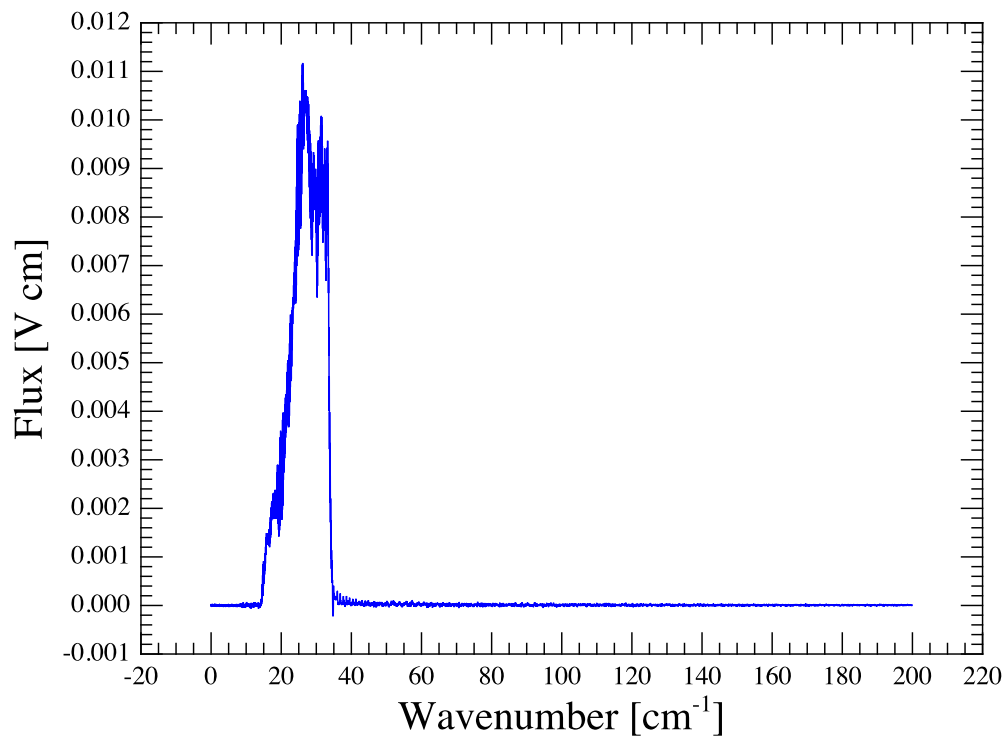


Figure A.5: Example of an initial level 1 unapodized spectra. This spectrometer detector spectrum has not yet had any corrections applied. Notice that the spectrum extends far beyond the bandwidth of the SLW (14.6 cm to 33.3 cm)

put. It also requires as input the bandEdge calibration product, which defines the edge of the two bands (SSW and SLW). It outputs a trimmed SDS.

A.6.2 Correcting for instrument emission

The total emission measured by the spectrometer bolometers is a sum of the source, telescope and instrument emissions modelled by

$$\text{Measurement} = R_{Source}B_{Source} + R_{Telescope}B_{Telescope} + R_{Instrument}B_{Instrument} \quad (\text{A.2})$$

where R_X is the corresponding Relative Spectral Response Function (RSRF) and B_X are the corresponding intensities (SPI, 2011c). Therefore, proper subtraction of both the telescope and instrument emission from the spectrum is necessary in order to recover the true spectrum of our source. The instrument emission depends upon the temperature of the enclosure, which is similar to a black body. The instrument temperature varies from operation day to operation day by up to 4 to 5 Kelvin, and will also vary slightly throughout an observation from scan to scan. Because of this, each scan needs to be corrected for instrument emission prior to averaging all of the scans together. This correction is applied using the *instCorrection* task. It requires as input the SDS from which the instrument emission will be removed, and the NHKT from the observation, from which the temperature measurements taken throughout the observation are extracted. Finally, the RSRF of the instrument, which characterizes the spectral response of the instrument, is also included as a calibration product. Output is an SDS which has been corrected for instrument emission.

A.6.3 Applying the extended source flux conversion

After the instrument correction is applied, but before the telescope emission is subtracted from the spectra, the spectra are converted from units of volts per wavenumber to flux per Hz per Sr. The flux conversion is performed using the *specFluxConversion* task and is performed assuming a uniform and fully extended source. This is the default flux conversion mode for the pipeline, and a correction will need to be made later on in the reduction process to account for the fact that our source is not truly extended on the scale assumed. The task requires the SDS as input, and the flux converted SDS is the output. The necessary conversion factors are stored in the telescope RSRF calibration product, which in our case is the default telescope RSRF as extracted from the standard calibration context.

A.6.4 Removal of telescope emission

The telescope itself is also a source of considerable emission measured by the instrument which must be removed from the SDS, and once the instrument emission has been accounted for in equation A.2, it remains as the only source of radiation besides the source itself. While the telescope temperature does not vary substantially over the course of an observation day, it does vary over the lifetime of the telescope. The ideal method by which to correct for the telescope emission is to acquire a dark sky observation on the day of the observation and to subtract the dark sky emission from the observation. This requires considerable telescope time, especially for intermediate and fully-sampled observations and is typically not performed for such observations.

Instead, the telescope emission is modelled from a library of darks and the housekeeping data from the day of the observation which contains all the necessary telescope temperature timelines from which to create such a timeline.

The telescope emission is modelled and then subtracted from the SDS using the *telescopeCorrection* task. It requires only the SDS and the housekeeping product as input. The housekeeping product is extracted from the observation context. The task outputs a telescope subtracted SDS, which will at this point begin to look like the spectrum of the galaxy. The resulting SDS is then saved to the local hard disk using the *simpleFitsWriter* task. There will be one file for each jiggle position, for a total of 16 files, each containing a set of SDS for all the detectors.

A.7 Level 2 Maps

A level 2 map is a data cube in which reduced intermediate and fully sampled observations are stored, with the typical RA and Dec axes, along with a third axes in units of wavenumber (cm^{-1}). The standard mapping reduction script contains the necessary code to produce level 2 extended calibrated maps from a single observation. Not only is our source not truly extended, but we also need to combine both observations into a single level 2 map. A custom script is used to apply both the flux conversion and to create the level 2 maps. Currently, the beam parameter files necessary for the point source flux conversion exist only for a set of 7 co-aligned detectors (Table A.1). Since the *specFluxConversion* task will only apply a point source flux conversion to the pair of central pixels (SLWC3 for the SLW, and SSWD4 for the SSW) of

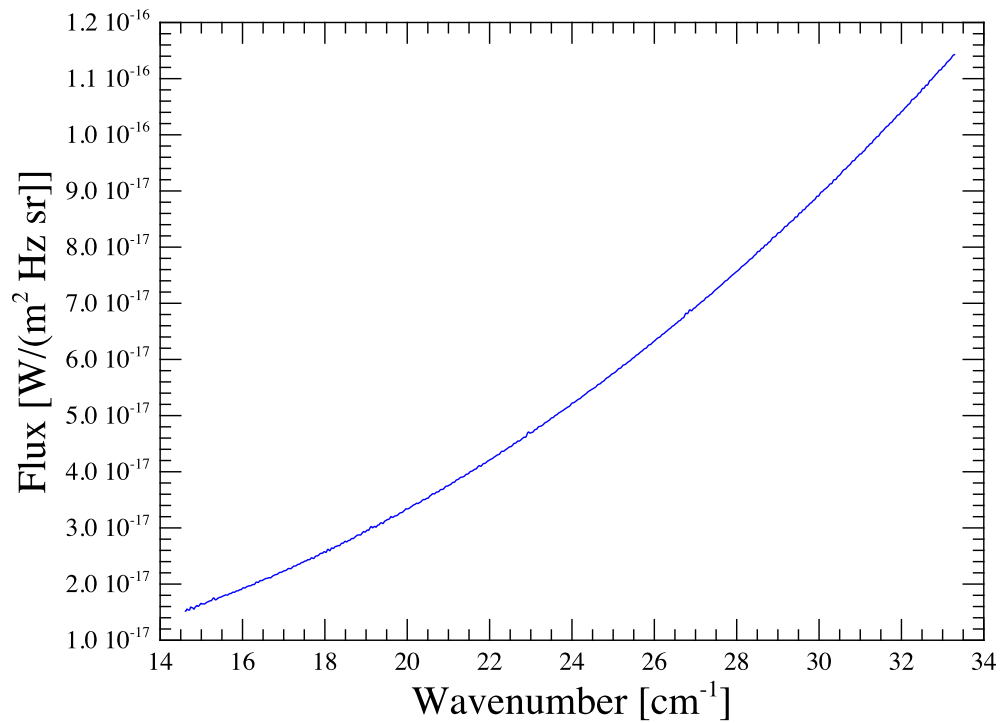


Figure A.6: SDS prior to the removal of the telescope emission. Most of the signal is the blackbody emission from the telescopes primary mirror.

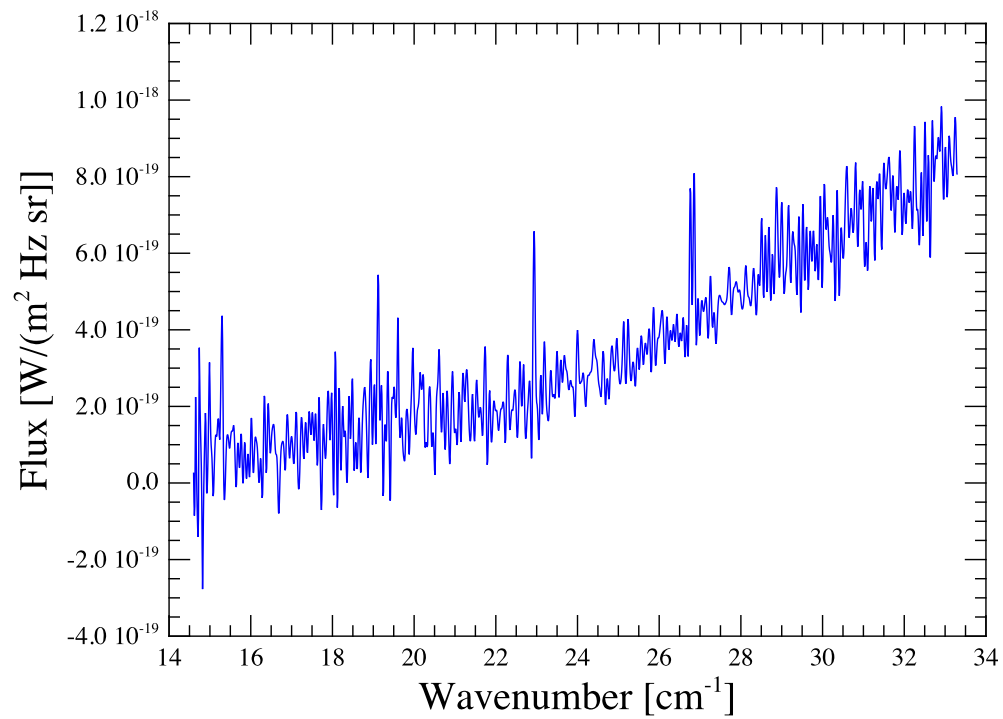


Figure A.7: Representative final level 1 spectrum from the reduction of the nucleus of NGC 4038 after subtraction of the telescope emission.

any jiggle position, for each set of co-aligned detectors we must first filter out all other detectors from our new SDS, move the co-aligned detectors to the central pixel position, load in a unique *beamParam* file, apply the point source calibration and then move the detectors back to their original position.

Table A.1: Co-aligned detectors

SLW	SSW
SLWC3	SSWD4
SLWB2	SSWE5
SLWD2	SSWE2
SLWC2	SSWF3
SLWB3	SSWC5
SLWC4	SSWB3

A.7.1 Point source calibration

First, a single *SpireMapContext* is created to store all of the SDS as the point source flux conversion is applied to both the nucleus and overlap observations. In the following, I will describe how the point source calibration is applied for one pair of co-aligned detectors from a single jiggle position of one of the observations. The process is the same for all co-aligned detectors, jiggle positions and both observations.

The Level 1 spectra for the given jiggle position which were saved at the end of the reduction are loaded using the *simpleFitsReader* task in the form of an SDS. We then create a copy of the SDS, from which we filter out all of the spectrometer channels except for the co-aligned pair (1 detector each in the SSW and SLW) using the *filterchannels* task. A custom routine named

moveChansToCentral is used to move the co-aligned pairs to the position of the central detectors, the SLWC3 and SSWD4 detectors for the SLW and SSW respectively. The beam parameter file for the current co-aligned pair is loaded using another custom routine *getBeamParamFile*.

We apply the point source calibration to the new centre pixels with the *specFluxConversion* task. We input the SDS, and the *beamParam*, and set the parameter *APPLY_POINT_SOURCE* to *TRUE*. Finally, the co-aligned pair of detectors are moved back to their original position using the custom routine *moveChansFromCentral*. The detectors are added to a new SDS variable. When all of the co-aligned pairs are processed for a single jiggle observation, this new SDS is added to the *SpireMapContext*.

A.7.2 Level 2 map creation

The standard mapping reduction script contains the necessary code to produce level 2 maps from a single observation. We have, however, two separate observations from which to create such a map and I have written a custom script to combine both observations to create a single map. This custom script is based on the code for creating a level 2 map from a single observation from the standard script with some modification. There are two possible tasks which can be used to create the data cubes. The *nearestNeighbourProjection* task works by assigning to each pixel the spectrum from the nearest detector from all of the jiggle positions. While this task is fast, there are two noticeable problems with it. The first is that, especially near the edges of the map, there can be multiple pixels which use the spectra from the same detector, leading

to pixels which are exactly the same. Secondly, for larger pixel sizes, it may be true that not all of the detectors will be used to create the map.

The task which we use is the *naiveProjection* task. It works by averaging all of the detectors which overlap the pixel. Unfortunately, if a pixel has no detectors which overlap the pixel, it will not have a spectrum assigned to it. This occurs near the edges of the map; however there can also be dead pixels scattered throughout the map, and discretion must be used when choosing pixel sizes to have adequate pixel coverage. We choose a pixel size of 15" for the SLW.

The process for creating the SLW and SSW maps is exactly the same. First, we create a pre-processed cube using the *spirePreprocessCube* task. It requires as input the spire mapping context. The user needs to set the *arrayType* (SLW or SSW) and whether or not to include vignetted detectors, which we do not. Next, we set up the grid in world coordinates covering the entire area of our observations using the *SpireWcsCreator.createWcs* task. We input the pre-processed cube and the grid spacing in degrees, and it outputs the grid. Finally, we use the *naiveProjection* task to create the map, using the pre-processed cube and the world coordinate grid as input, and creating the level 2 map as output. Examples of slices of level 2 maps can be seen in figures 2.1 (SLW) and 2.4 (SSW)

A.7.3 Point source correction and level 2 map script

```
#####
```

```
#
# This script comes in two parts.  The first part of the script
# involves applying a point source correction to the co-aligned detectors.
# This portion of the script was provided by T. Fulton.
#
# The second part of the script is the actual creation of the
# level 2 maps.  This portion of the script is based upon the
# standard mapping pipeline script provided with HIPE.  It has been
# altered to accomodate the fact that the observations of NGC 4038
# need to be combined into a single level 2 map.  This was
# written by M. Schirm
#####

#Preamble for the corrections.  By T. Fulton

def moveChansToCentral(sds):
    for scan in sds.getScanNumbers():
        thisScan = sds.getScan(scan)
        for chan in thisScan.getChannelNames():
            channel = thisScan.removeChannel(chan)
            if String(chan).startsWith("SLW"):
                channel.setChannelName("SLWC3")
            if String(chan).startsWith("SSW"):
                channel.setChannelName("SSWD4")
        thisScan.setChannel(channel)
```

```
        pass
        sds.setScan(thisScan)
    return sds
pass

def moveChansFromCentral(sds, chanPair):
    for scan in sds.getScanNumbers():
        thisScan = sds.getScan(scan)
        for chan in chanPair:
            if String(chan).startsWith("SLW"):
                channel = thisScan.removeChannel("SLWC3")
            if String(chan).startsWith("SSW"):
                channel = thisScan.removeChannel("SSWD4")
            channel.setChannelName(chan)
            thisScan.setChannel(channel)
        pass
        sds.setScan(thisScan)
    return sds
pass

def getBeamParamFile(calPath, chanPair, res):
    calFile = \
    "SCalSpecBeamParam_%s_unapod_v7_0_0_%s_%s.fits\
    "%(res, chanPair[0], chanPair[1])
    beamParam = FitsArchive().load("%s%s"%(calPath, calFile))
```

```
        return beamParam
pass

"""
A list of the co-aligned detector pairs.
"""
chanPairs = [ \
    ["SLWC3", "SSWD4"], \
    ["SLWB2", "SSWE5"], \
    ["SLWD2", "SSWE2"], \
    ["SLWC2", "SSWF3"], \
    ["SLWB3", "SSWC5"], \
    ["SLWD3", "SSWC2"], \
    ["SLWC4", "SSWB3"]]
pass

##Here we start to work with the old script.  Written by M. Schirm

myObsidOverlap = "1342210859"
myObsidNucleus = "1342210860"
apodName = "unapod"

#From home
outdirOverlap = \
"/Users/mschirm/Documents/Grad/Herschel/Reprocessing/NGC4038/8.0/Overlap/Outdir/"
```

```
outdirNucleus = \  
"/Users/mschirm/Documents/Grad/Herschel/Reprocessing/NGC4038/8.0/Nucleus/Outdir/"  
outdirCombined = \  
"/Users/mschirm/Documents/Grad/Herschel/Reprocessing/NGC4038/8.0/Combined/Outdir/"  
  
raster = 0  
SLWpixsize = 15 #Pixel size for SLW data  
SSWpixsize = 10 #Pixel size for SSW data  
gridSpacing = {"SSW": SSWpixsize / 3600.0, "SLW": SLWpixsize / 3600.0}  
jiggList = [0,1,2,3,4,5,6,7,8,9,10,11,12,13,14,15]  
#jiggList = [0]  
calPath = \  
"/Users/mschirm/Documents/Grad//Herschel/Reprocessing/Calibration/HCSS_7_0_0/"  
res = "HR"  
#jiggId = 4  
  
sdsList = SpireMapContext()  
  
#Here is where we load the data one file at a time. This section of the  
#code is written by T. Fulton, while M. Schirm has modified it only  
#in the sense to implement it into this script.  
  
for jiggId in jiggList:  
    print raster,jiggId
```

```
sds = simpleFitsReader("%s%s_spectrum_HR_%s_%i_%i.fits"%(outdirOverlap, \
                    myObsidOverlap, apodName, raster, jiggId))
sdsCopy = sds.copy()
firstTime = 1
for chanPair in chanPairs:
    sds = sdsCopy.copy()
    sdsFilter = filterChannels(bbp=sds, \
        keepChannels=String1d(chanPair))
    sdsFilter = moveChansToCentral(sdsFilter)
    beamParam = getBeamParamFile(calPath, chanPair, res)
    sdsFilter = specFluxConversion(sds=sdsFilter, \
        beamParam=beamParam, APPLY_POINT_SOURCE=Boolean.TRUE)
    sdsFilter = moveChansFromCentral(sdsFilter, chanPair)
    if firstTime == 1:
        firstTime = 0
        newSds = sdsFilter.copy()
        continue
    pass
    for scan in newSds.getScanNumbers():
        thisScan = newSds.getScan(scan)
        thisScan.setChannel(sdsFilter[scan].getChannel(chanPair[0]))
        thisScan.setChannel(sdsFilter[scan].getChannel(chanPair[1]))
    pass
pass
sdsList.setProduct("%d"%(sdsList.refs.size()), newSds)
```

```
for jiggleId in jiggleList:
    sds = simpleFitsReader("%s%s_spectrum_HR_%s_%i_%i.fits"%(outdirNucleus, \
        myObsidNucleus, apodName, raster, jiggleId))
    sdsCopy = sds.copy()
    firstTime = 1
    for chanPair in chanPairs:
        sds = sdsCopy.copy()
        sdsFilter = filterChannels(bbp=sds, keepChannels=StringId(chanPair))
        sdsFilter = moveChansToCentral(sdsFilter)
        beamParam = getBeamParamFile(calPath, chanPair, res)
        sdsFilter = specFluxConversion(sds=sdsFilter, \
            beamParam=beamParam, APPLY_POINT_SOURCE=Boolean.TRUE)
        sdsFilter = moveChansFromCentral(sdsFilter, chanPair)
        if firstTime == 1:
            firstTime = 0
            newSds = sdsFilter.copy()
            continue
        pass
    for scan in newSds.getScanNumbers():
        thisScan = newSds.getScan(scan)
        thisScan.setChannel(sdsFilter[scan].getChannel(chanPair[0]))
        thisScan.setChannel(sdsFilter[scan].getChannel(chanPair[1]))
    pass
pass
```

```
sdsList.setProduct("%d"%(sdsList.refs.size()),newSds)
```

#And finally we create the level 2 map. This was taken almost in its entirety from the standard mapping reduction script, with the modifications by #M. Schirm clearly marked

```
for array in ['SSW','SLW']:  
    if array=='SSW': #M.Schirm  
        pixsize = SSWpixsize #M.Schirm  
    if array == 'SLW': #M.Schirm  
        pixsize = SLWpixsize #M.Schirm  
    # Create a pre-processed cube (not regularly gridded)  
    preCube = spirePreprocessCube(context=sdsList, \  
arrayType=array, UNVIGNETTED=True)  
    # Set up the grid - covering the  
    #RA and Dec of observed points using specified gridSpacing  
    wcs = SpireWcsCreator.createWcs(preCube, \  
gridSpacing[array], gridSpacing[array])  
    # Regrid the data  
    cube = naiveProjection(spc = preCube, wcs = wcs)  
    # Save the cube  
    simpleFitsWriter(cube, "%sNGC4038_%s_%s_%s_cube.fits"%(outdirCombined, \  
array, apodName, pixsize)) # (Modified by M. Schirm)
```

Appendix B

Line Fitting

B.1 Description

Extraction of the CO emission lines from our spectral cube was performed using a custom line fitting script I wrote in HIPE. In this Appendix I present the line-fitting script in detail. The script consists of 3 major components. First, the baseline is removed by fitting a polynomial to the entire spectrum and subtracting it. Secondly, sinc functions are fit to the baseline subtracted spectrum for each of the CO and CI lines. Finally, the sinc functions are integrated analytically and integrated intensity maps are created for each of the CO lines. All three steps are performed across the entire SLW map. Currently, this script is limited to fitting the CO lines in the SLW spectrum, but it can be easily modified to fit any lines in either the SLW or SSW.

The script begins by loading in the level 2 data cube using the *simpleFitsReader* task. It creates a two dimensional array for each line which it will to fit, which are the CO $J = 4 - 3$, $5 - 4$, $6 - 5$, $7 - 6$, and $8 - 7$ transitions. For each pixel in the cube, the spectrum and measurement errors are extracted

from the pixel. The baseline can then be fit using either the *smoothBaseline* task, or a custom polynomial fitting routine, *BasePolyFit*.

The *BasePolyFit* fitting routine is a custom routine which fits a polynomial of any order to a spectrum. It is based on a built-in fitter provided with HIPE. The custom routine requires as input the frequency vector, the spectrum to be fit, and the spectrum weights, along with the order of the polynomial we wish to fit to the baseline. The routine returns the baseline along with the baseline subtracted spectrum. In this study, I opt for this routine for the baseline subtraction.

Alternatively, the *smoothBaseline* task can be used to fit the baseline of the spectrum. The task first requires that the user remove fringes in the spectra using the *FitFringeData* task (HCS, 2011). The fringe-removed spectra is then input into the *smoothBaseline* task as the only require input. There are numerous parameters which the user can set. The first is the *midcycle* parameter which is the cycle frequency used for smoothing (Her, 2011), which we set to $7 \times 10^4 \mu\text{m}^{-1}$. The second parameter is the *plot* parameter, which determines whether to plot the results or not. Lastly, the *box* is the size of the box used to determine outliers, which is set 5 times the number of midcycles. The task will first mask out any spectral features and outliers using the criteria assigned to the parameters and then calculates the baseline based on the masked data. The baseline calculated by the *smoothBaseline* task is subtracted from the spectrum to create the baseline subtracted spectrum to which the sinc functions will be fit.

The script requires three initial guesses for each spectral line: The amplitude of the line, the centre of the line, and the line width. The guess for the centre of the line is determined by calculating the observed frequency from the emitted frequency based on the redshift of the galaxy. The initial guess for the line widths is $\Delta\nu = 0.3$ GHz. The initial guess for the amplitude is determined by finding the intensity in the spectrum at the initial guess frequency for a given line and will vary from pixel to pixel.

The spectral lines are fit using a custom routine written specifically to fit sinc functions to spectral lines, the *SincFit* routine. The inputs of the routine are the frequency vector, the baseline subtracted spectrum and the spectrum weights, along with the initial guesses and which fitter to use. The sinc function fitter routine uses either a Levenberg-Marquardt fitter through the *LevenbergMarquardtFitter* task or an Amoeba fitter through the *AmoebaFitter* task, and fits over a 30 GHz (1 cm^{-1}) frequency range centred on the guess for the frequency. The task will return the parameters of best fit along with the standard deviation in the fits.

After the fit, the *SincFit* routine checks to see if the fitted line frequency is within 600 km/s of the original line, as the line centre will not deviate from the guess by more than this. If the fitted line frequency does deviate by more than this amount, the routine will attempt to fit the line again, this time by holding the amplitude constant. Finally, before output, the line is subtracted from the baseline subtracted spectrum to create the line subtracted spectrum. The *SincFit* routine outputs the fitted parameters for the amplitude, frequency

and width of the emission line, the line subtracted spectrum and the standard deviation of the fitted parameters.

Each CO line is fit in succession using the *SincFit* routine. The CO $J = 7 - 6$ and *CI* $J = 2 - 1$ doublet is fit simultaneously, and the parameters for the CO line is extracted. The integrated intensity and standard deviation is calculated by equations (2.6) and (2.7) using the custom *intrSinc* routine. If the fitted amplitude is less than 0, or the line width is greater than 300 km/s, the fit is treated as a non-detection.

The baseline is over plotted on the spectrum, and each line fit is over plotted on the baseline subtracted spectrum, all of which are saved to file. By combining the integrated intensities for each pixel, the script creates maps for each of the 5 CO lines. The error is the fitting error calculated from the standard deviation. Pixels with non-detections are set as blank. Examples of fits are shown in Figure 2.7, and examples of integrated intensity maps are displayed in Figures 2.8, 2.9, 2.10, 2.11, and 2.12. The script itself is presented below, in Section B.2.

B.2 Script

```
def BasePolyFit(freq,int,intw,order):
    iFit = freq.where(freq>400)
    baselineModel = PolynomialModel(order)
    baselineFitter = Fitter(freq[iFit],baselineModel)
    baselineFitter.fit(int[iFit],intw[iFit])
```

```
baseline=baselineModel(freq)
intBS = int-baseline
return baseline,intBS

def SincFit(freq,int,intBSw,guesses,ft):
    sz=guesses.size/3
    lineModel = SincModel()
    while sz>1:
        lineModel+=SincModel()
        sz = sz-1
    if guesses[1] < 200:
        lineModel += PolynomialModel(1) #Try adding a linear background
        guesses.append(0)
        guesses.append(0)
    ifreq = freq.where((freq>guesses[1]-10).and(freq<guesses[1]+10))
    lineModel.setParameters(guesses)
    if ft == "AM":
        lineFitter = AmoebaFitter(freq[ifreq], lineModel)
    if ft == "LM":
        lineFitter = LevenbergMarquardtFitter(freq[ifreq], lineModel)
    lineFitter.fit(int[ifreq],intBSw[ifreq])
    int_linesub = int-lineModel(freq)
    stdev = lineFitter.getStandardDeviation()
    diff = abs(lineModel.getParameters()[1]-guesses[1])
    jfreq = \
```

```

freq.where((freq>guesses[1]-600/c*guesses[1]).\
and(freq<guesses[1]+600/c*guesses[1]))
imax = int.where(int==max(int[ifreq]))
ampdiff = abs(lineModel.getParameters()[0]-int[imax][0])
if (diff>600/c*guesses[1]):
    if ampdiff>0.5:
        try:
            lineModel.setParameters(guesses)
            lineModel.keepFixed(Int1d([1]), [guesses[0]])
            if ft == "AM":
                lineFitter = AmoebaFitter(freq[ifreq], lineModel)
            if ft == "LM":
                lineFitter = LevenbergMarquardtFitter(freq[ifreq], lineModel)
            lineFitter.fit(int[ifreq],intBSw[ifreq])
            int_linesub = int-lineModel(freq)
            stdev = lineFitter.getStandardDeviation()
        except:
            lineModel = "Bad!"
    return lineModel,int_linesub,stdev

def intgrSinc(param,stdev): #Used to calculate II and IIerr
    dv = abs((param[2]*c)/param[1])
    stddv = abs(param[2]*SQRT(((stdev[1]/param[1])**2+(stdev[2]/param[2])**2)))
    II = param[0]*Math.PI*dv
    IIerr = II*SQRT(((stdev[0]/param[0])**2+(stddv/dv)**2))

```

```
    if II<0:
        II = Double.NaN
        IIerr = Double.NaN
    if (abs(dv)>300):
        II = Double.NaN
        IIerr = Double.NaN
    return II, IIerr

from herschel.ia.numeric.toolbox.basic import Square
from herschel.ia.toolbox.spectrum.standingwaves import FitFringeData
from herschel.ia.toolbox.spectrum.standingwaves import SmoothBaseline
from herschel.share.fltdyn.math import *

#Some Constants
c = 299792.458 #in km/s
array = "SLW"
pixsize = 15
doplot = 1
sBaseline = 0
if sBaseline == 1:
    baseType = "smooth"
else:
    baseType = "poly"

outdirCombined = \
"/Users/mschirm/Documents/Grad/Herschel/Reprocessing/NGC4038/8.0/Combined/Outdir/"
```

```
saveDir = \  
"/Users/mschirm/Documents/Grad/Herschel/Reprocessing/NGC4038/8.0/Images/"  
figDir = \  
"/Users/mschirm/Documents/Grad/Thesis/Figures/"  
saveName = "NGC4038"  
apodName = "unapod"  
line43 = "C04-3"  
line54 = "C05-4"  
line65 = "C06-5"  
line76 = "C07-6"  
line87 = "C08-7"  
corrected = ""  
  
#  
cube = simpleFitsReader("%sNGC4038_%s%s_%s_%s_cube.fits"\  
%(outDirCombined, corrected, array, apodName, pixsize))  
  
#  
###This first part was put in here to test loading data and plotting.  
###Load in a level2 cube  
  
#  
freq = cube["ImageIndex"]["DepthIndex"].data*29.98  
frequnit = "GHz"  
  
#Get the size of the image to loops through  
xsize = cube.image[1,:,1].size  
ysize = cube.image[1,1,:].size
```

```
#Now let's start our loop

II43 = Double2d(xsize,ysize)
IIerr43 = Double2d(xsize,ysize)

II54 = Double2d(xsize,ysize)
IIerr54 = Double2d(xsize,ysize)

II65 = Double2d(xsize,ysize)
IIerr65 = Double2d(xsize,ysize)

II76 = Double2d(xsize,ysize)
IIerr76 = Double2d(xsize,ysize)

II87 = Double2d(xsize,ysize)
IIerr87 = Double2d(xsize,ysize)

for i in range(0,xsize):
for j in range(0,ysize):
int = cube.image[:,i,j]
intw = cube.weight[:,i,j]
intf = Int1d(int.size)
try:
if sBaseline ==1:
    swData = FitFringeData(freq,int,intf,intw)
```

```
baseline = smoothBaseline(data=swData,midcycle=7.e4, \
plot=False,box=5)
intBS = int-baseline
else:
baseline,intBS = BasePolyFit(freq,int,intw,19)
intBSHold = intBS
Guess43 = Double1d([1,458.7,0.3])
Guess54 = Double1d([1,573.5,0.3])
Guess65 = Double1d([1,688,0.3])
Guess76 = Double1d([1,802.5,0.3,1,805.3,0.3])
Guess87 = Double1d([1,917.5,0.3])
dfreq = freq[2]-freq[1]
ifreq43 = freq.where((freq<Guess43[1]+5*dfreq).\
and(freq>Guess43[1]-5*dfreq))
ifreq54 = freq.where((freq<Guess54[1]+5*dfreq).\
and(freq>Guess54[1]-5*dfreq))
ifreq65 = freq.where((freq<Guess65[1]+5*dfreq).\
and(freq>Guess65[1]-5*dfreq))
ifreq76 = freq.where((freq<Guess76[1]+5*dfreq).\
and(freq>Guess76[1]-5*dfreq))
ifreq76a = freq.where((freq<Guess76[4]+5*dfreq).\
and(freq>Guess76[4]-5*dfreq))
ifreq87 = freq.where((freq<Guess87[1]+5*dfreq).\
and(freq>Guess87[1]-5*dfreq))
Guess43[0] = max(intBS[ifreq43])
```

```
Guess54[0] = max(intBS[ifreq54])
Guess65[0] = max(intBS[ifreq65])
Guess76[0] = max(intBS[ifreq76])
Guess76[3] = max(intBS[ifreq76a])
Guess87[0] = max(intBS[ifreq87])
int43 = intBS
Model43,intBS,stdev=SincFit(freq,intBS,intw,Guess43,"LM")
if Model43 == "Bad!":
    II43[i,j],IIerr43[i,j] = 0,0
else:
    II43[i,j],IIerr43[i,j] = intgrSinc(Model43.getParameters(),stdev)
Model54,intBS,stdev=SincFit(freq,intBS,intw,Guess54,"AM")
if Model54 == "Bad!":
    II54[i,j],IIerr54[i,j] = 0,0
else:
    II54[i,j],IIerr54[i,j] = intgrSinc(Model54.getParameters(),stdev)
Model65,intBS,stdev=SincFit(freq,intBS,intw,Guess65,"LM")
if Model65 == "Bad!":
    II65[i,j],IIerr65[i,j] = 0,0
else:
    II65[i,j],IIerr65[i,j] = intgrSinc(Model65.getParameters(),stdev)
Model76,intBS,stdev=SincFit(freq,intBS,intw,Guess76,"LM")
if Model76 == "Bad!":
    II76[i,j],IIerr76[i,j] = 0,0
else:
```

```
    II76[i,j],IIerr76[i,j] = intgrSinc(Model76.getParameters(),stdev)
Model87,intBS,stdev=SincFit(freq,intBS,intw,Guess87,"LM")
if Model87 == "Bad!":
    II87[i,j],IIerr87[i,j] = 0,0
else:
    II87[i,j],IIerr87[i,j] = intgrSinc(Model87.getParameters(),stdev)
if doplot == 1:
plot = PlotXY()
plot.autoBoxAxes=1
layer2 = LayerXY(freq,int43)
layer = LayerXY(freq,Model43(freq))
plot.addLayer(layer2)
plot.addLayer(layer)
plot.xaxis.range=[458.7-20,458.7+20]
plot.saveAsPDF("%sLineFitting/NGC4038C043_%s_%i_%i.PDF"\
%(figDir,baseType,i,j))
plot.removeLayer(layer)
layer = LayerXY(freq,Model54(freq))
plot.addLayer(layer)
plot.xaxis.range=[573.5-20,573.5+20]
plot.saveAsPDF("%sLineFitting/NGC4038C054_%s_%i_%i.PDF"\
%(figDir,baseType,i,j))
plot.removeLayer(layer)
layer = LayerXY(freq,Model65(freq))
plot.addLayer(layer)
```

```
plot.xaxis.range=[688-20,688+20]
plot.saveAsPDF("%sLineFitting/NGC4038C065_%s_%i_%i.PDF"\
%(figDir,baseType,i,j))
plot.removeLayer(layer)
layer = LayerXY(freq,Model76(freq))
plot.addLayer(layer)
plot.xaxis.range=[802.5-20,802.5+20]
plot.saveAsPDF("%sLineFitting/NGC4038C076_%s_%i_%i.PDF"\
%(figDir,baseType,i,j))
plot.removeLayer(layer)
layer = LayerXY(freq,Model87(freq))
plot.addLayer(layer)
plot.xaxis.range=[917.5-20,917.5+20]
plot.saveAsPDF("%sLineFitting/NGC4038C087_%s_%i_%i.PDF"\
%(figDir,baseType,i,j))
basePlot = PlotXY()
basePlot.autoBoxAxes=1
origLayer = LayerXY(freq,int)
baseLayer = LayerXY(freq,baseline)
basePlot.addLayer(origLayer)
basePlot.addLayer(baseLayer)
basePlot.yaxis.range=[-10,10]
basePlot.saveAsPDF("%sLineFitting/NGC4038BaseLine_%s_%i_%i.PDF"\
%(figDir,baseType,i,j))
except:
```

```
II43[i,j] = Double.NaN
IIerr43[i,j] = Double.NaN
II54[i,j] = Double.NaN
IIerr54[i,j] = Double.NaN
II65[i,j] = Double.NaN
IIerr65[i,j] = Double.NaN
II76[i,j] = Double.NaN
IIerr76[i,j] = Double.NaN
II87[i,j] = Double.NaN
IIerr87[i,j] = Double.NaN
```

```
Image43 = SimpleImage()
Image43.setImage(II43)
Image43.setError(IIerr43)
Image43.meta = cube.meta
Image43.setWcs(cube.getWcs())
Sigma43 = SimpleImage()
Sigma43.setImage(II43/IIerr43)
Sigma43.meta=cube.meta
Sigma43.setWcs(cube.getWcs())
```

```
simpleFitsWriter(Image43, "%sNGC4038_%s%s_%s_%s.fits"\
%(saveDir, corrected, pixsize, line43, baseType))
simpleFitsWriter(Sigma43, "%sNGC4038_sigma_%s%s_%s_%s.fits"\
%(saveDir, corrected, pixsize, line43, baseType))
```

```
Image54 = SimpleImage()
Image54.setImage(II54)
Image54.setError(IIerr54)
Image54.meta = cube.meta
Image54.setWcs(cube.getWcs())
Sigma54 = SimpleImage()
Sigma54.setImage(II54/IIerr54)
Sigma54.meta=cube.meta
Sigma54.setWcs(cube.getWcs())
simpleFitsWriter(Image54, "%sNGC4038_%s%s_%s_%s.fits"\
%(saveDir, corrected, pixsize, line54, baseType))
simpleFitsWriter(Sigma54, "%sNGC4038_sigma_%s%s_%s_%s.fits"\
%(saveDir, corrected, pixsize, line54, baseType))

Image65 = SimpleImage()
Image65.setImage(II65)
Image65.setError(IIerr65)
Image65.meta = cube.meta
Image65.setWcs(cube.getWcs())
Sigma65 = SimpleImage()
Sigma65.setImage(II65/IIerr65)
Sigma65.meta=cube.meta
Sigma65.setWcs(cube.getWcs())
simpleFitsWriter(Image65, "%sNGC4038_%s%s_%s_%s.fits"\
```

```
%(saveDir, corrected, pixsize, line65, baseType))
simpleFitsWriter(Sigma65, "%sNGC4038_sigma_%s_%s_%s.fits"\
%(saveDir, corrected, pixsize, line65, baseType))
```

```
Image76 = SimpleImage()
Image76.setImage(II76)
Image76.setError(IIerr76)
Image76.meta = cube.meta
Image76.setWcs(cube.getWcs())
Sigma76 = SimpleImage()
Sigma76.setImage(II76/IIerr76)
Sigma76meta=cube.meta
Sigma76.setWcs(cube.getWcs())
simpleFitsWriter(Image76, "%sNGC4038_%s_%s_%s.fits"\
%(saveDir, corrected, pixsize, line76, baseType))
simpleFitsWriter(Sigma76, "%sNGC4038_sigma_%s_%s_%s.fits"\
%(saveDir, corrected, pixsize, line76, baseType))
```

```
Image87 = SimpleImage()
Image87.setImage(II87)
Image87.setError(IIerr87)
Image87.meta = cube.meta
Image87.setWcs(cube.getWcs())
Sigma87 = SimpleImage()
Sigma87.setImage(II87/IIerr87)
```

```
Sigma87meta=cube.meta  
Sigma87.setWcs(cube.getWcs())  
simpleFitsWriter(Image87, "%sNGC4038_%s_%s_%s.fits"\  
%(saveDir, corrected, pixsize, line87, baseType))  
simpleFitsWriter(Sigma87, "%sNGC4038_sigma_%s_%s_%s.fits"\  
%(saveDir, corrected, pixsize, line87, baseType))
```

Bibliography

2011, HCSS User's Reference Processing

2011, Herschel Data Analysis Guide

2011a, SPIRE Data Reduction Guide

2011b, SPIRE Developers Reference Manual

2011c, SPIRE Observers' Manual

Ade, P. A. R., Hamilton, P. A., & Naylor, D. A. 1999, in *Fourier Transform Spectroscopy: New Methods and Applications* (Optical Society of America), FWE3

Bayet, E., Gerin, M., Phillips, T. G., & Contursi, A. 2006, *A&A*, 460, 467

Bendo, G. J., Wilson, C. D., Warren, B. E., Brinks, E., Butner, H. M., Chaniai, P., Clements, D. L., Courteau, S., Irwin, J., Israel, F. P., Knapen, J. H., Leech, J., Matthews, H. E., Mühle, S., Petitpas, G., Serjeant, S., Tan, B. K., Tilanus, R. P. J., Usero, A., Vaccari, M., van der Werf, P., Vlahakis, C., Wiegert, T., & Zhu, M. 2010, *MNRAS*, 402, 1409

Bradford, C. M., Stacey, G. J., Nikola, T., Bolatto, A. D., Jackson, J. M., Savage, M. L., & Davidson, J. A. 2005, *ApJ*, 623, 866

Calzetti, D., Armus, L., Bohlin, R. C., Kinney, A. L., Koornneef, J., & Storchi-Bergmann, T. 2000, *ApJ*, 533, 682

Carroll, T. J. & Goldsmith, P. F. 1981, ApJ, 245, 891

Cluver, M. E., Jarrett, T. H., Kraan-Korteweg, R. C., Koribalski, B. S., Appleton, P. N., Melbourne, J., Emonts, B., & Woudt, P. A. 2010, ApJ, 725, 1550

Cutri, R. M. & McAlary, C. W. 1985, ApJ, 296, 90

de Graauw, T., Helmich, F. P., Phillips, T. G., Stutzki, J., Caux, E., Whyborn, N. D., Dieleman, P., Roelfsema, P. R., Aarts, H., Assendorp, R., Bachiller, R., Baechtold, W., Barcia, A., Beintema, D. A., Belitsky, V., Benz, A. O., Bieber, R., Boogert, A., Borys, C., Bumble, B., Caïs, P., Caris, M., Cerulli-Irelli, P., Chattopadhyay, G., Cherednichenko, S., Ciechanowicz, M., Coeur-Joly, O., Comito, C., Cros, A., de Jonge, A., de Lange, G., Delforges, B., Delorme, Y., den Boggende, T., Desbat, J.-M., Diez-González, C., di Giorgio, A. M., Dubbeldam, L., Edwards, K., Eggens, M., Erickson, N., Evers, J., Fich, M., Finn, T., Franke, B., Gaier, T., Gal, C., Gao, J. R., Gallego, J.-D., Gauffre, S., Gill, J. J., Glenz, S., Golstein, H., Goulooze, H., Gunsing, T., Güsten, R., Hartogh, P., Hatch, W. A., Higgins, R., Honingh, E. C., Huisman, R., Jackson, B. D., Jacobs, H., Jacobs, K., Jarchow, C., Javadi, H., Jellema, W., Justen, M., Karpov, A., Kasemann, C., Kawamura, J., Keizer, G., Kester, D., Klapwijk, T. M., Klein, T., Kollberg, E., Kooi, J., Kooiman, P.-P., Kopf, B., Krause, M., Krieg, J.-M., Kramer, C., Kruizenga, B., Kuhn, T., Laauwen, W., Lai, R., Larsson, B., Leduc, H. G., Leinz, C., Lin, R. H., Liseau, R., Liu, G. S., Loose, A., López-Fernandez, I., Lord, S., Luinge, W., Marston, A., Martín-Pintado, J., Maestrini, A., Maiwald, F. W., McCoey, C., Mehdi, I., Megej, A., Melchior, M., Meinsma,

L., Merkel, H., Michalska, M., Monstein, C., Moratschke, D., Morris, P., Muller, H., Murphy, J. A., Naber, A., Natale, E., Nowosielski, W., Nuzzolo, F., Olberg, M., Olbrich, M., Orfei, R., Orleanski, P., Ossenkopf, V., Peacock, T., Pearson, J. C., Peron, I., Phillip-May, S., Piazzo, L., Planesas, P., Rataj, M., Ravera, L., Risacher, C., Salez, M., Samoska, L. A., Saraceno, P., Schieder, R., Schlecht, E., Schlöder, F., Schmülling, F., Schultz, M., Schuster, K., Siebertz, O., Smit, H., Szczerba, R., Shipman, R., Steinmetz, E., Stern, J. A., Stokroos, M., Teipen, R., Teyssier, D., Tils, T., Trappe, N., van Baaren, C., van Leeuwen, B.-J., van de Stadt, H., Visser, H., Wildeman, K. J., Wafelbakker, C. K., Ward, J. S., Wesselius, P., Wild, W., Wulff, S., Wunsch, H.-J., Tielens, X., Zaal, P., Zirath, H., Zmuidzinas, J., & Zwart, F. 2010, *A&A*, 518, L6

Duncan, J. C. 1923, *ApJ*, 57, 137

Fabbiano, G., Zezas, A., & Murray, S. S. 2001, *ApJ*, 554, 1035

Fulton, T. R., Baluteau, J., Bendo, G., Benielli, D., Gastaud, R., Griffin, M., Guest, S., Imhof, P., Lim, T. L., Lu, N., Naylor, D. A., Panuzzo, P., Polehampton, E., Schwartz, A., Surace, C., Swinyard, B. M., & Xu, K. 2010, in *Society of Photo-Optical Instrumentation Engineers (SPIE) Conference Series*, Vol. 7731, Society of Photo-Optical Instrumentation Engineers (SPIE) Conference Series

Gao, Y., Lo, K. Y., Lee, S.-W., & Lee, T.-H. 2001, *ApJ*, 548, 172

Gao, Y. & Solomon, P. M. 2004, *ApJ*, 606, 271

Gehrz, R. D., Sramek, R. A., & Weedman, D. W. 1983, *ApJ*, 267, 551

Genzel, R., Tacconi, L. J., Gracia-Carpio, J., Sternberg, A., Cooper, M. C., Shapiro, K., Bolatto, A., Bouché, N., Bournaud, F., Burkert, A., Combes, F., Comerford, J., Cox, P., Davis, M., Schreiber, N. M. F., Garcia-Burillo, S., Lutz, D., Naab, T., Neri, R., Omont, A., Shapley, A., & Weiner, B. 2010, MNRAS, 407, 2091

Gilbert, A. M., Graham, J. R., McLean, I. S., Becklin, E. E., Figer, D. F., Larkin, J. E., Levenson, N. A., Teplitz, H. I., & Wilcox, M. K. 2000, ApJ, 533, L57

Graciá-Carpio, J., García-Burillo, S., Planesas, P., & Colina, L. 2006, ApJl, 640, L135

Graciá-Carpio, J., García-Burillo, S., Planesas, P., Fuente, A., & Usero, A. 2008, A&A, 479, 703

Griffin, M. J., Abergel, A., Abreu, A., Ade, P. A. R., André, P., Augeres, J., Babbedge, T., Bae, Y., Baillie, T., Baluteau, J., Barlow, M. J., Bendo, G., Benielli, D., Bock, J. J., Bonhomme, P., Brisbin, D., Brockley-Blatt, C., Caldwell, M., Cara, C., Castro-Rodriguez, N., Cerulli, R., Chanial, P., Chen, S., Clark, E., Clements, D. L., Clerc, L., Coker, J., Communal, D., Conversi, L., Cox, P., Crumb, D., Cunningham, C., Daly, F., Davis, G. R., de Antoni, P., Delderfield, J., Devin, N., di Giorgio, A., Didschuns, I., Dohlen, K., Donati, M., Dowell, A., Dowell, C. D., Duband, L., Dumaye, L., Emery, R. J., Ferlet, M., Ferrand, D., Fontignie, J., Fox, M., Franceschini, A., Frerking, M., Fulton, T., Garcia, J., Gastaud, R., Gear, W. K., Glenn, J., Goizel, A., Griffin, D. K., Grundy, T., Guest, S., Guillemet, L., Hargrave,

P. C., Harwit, M., Hastings, P., Hatziminaoglou, E., Herman, M., Hinde, B., Hristov, V., Huang, M., Imhof, P., Isaak, K. J., Israelsson, U., Ivison, R. J., Jennings, D., Kiernan, B., King, K. J., Lange, A. E., Latter, W., Laurent, G., Laurent, P., Leeks, S. J., Lellouch, E., Levenson, L., Li, B., Li, J., Lilienthal, J., Lim, T., Liu, S. J., Lu, N., Madden, S., Mainetti, G., Marliani, P., McKay, D., Mercier, K., Molinari, S., Morris, H., Moseley, H., Mulder, J., Mur, M., Naylor, D. A., Nguyen, H., O'Halloran, B., Oliver, S., Olofsson, G., Olofsson, H., Orfei, R., Page, M. J., Pain, I., Panuzzo, P., Papageorgiou, A., Parks, G., Parr-Burman, P., Pearce, A., Pearson, C., Pérez-Fournon, I., Pinsard, F., Pisano, G., Podosek, J., Pohlen, M., Polehampton, E. T., Pouliquen, D., Rigopoulou, D., Rizzo, D., Roseboom, I. G., Roussel, H., Rowan-Robinson, M., Rownd, B., Saraceno, P., Sauvage, M., Savage, R., Savini, G., Sawyer, E., Scharnberg, C., Schmitt, D., Schneider, N., Schulz, B., Schwartz, A., Shafer, R., Shupe, D. L., Sibthorpe, B., Sidher, S., Smith, A., Smith, A. J., Smith, D., Spencer, L., Stobie, B., Sudiwala, R., Sukhatme, K., Surace, C., Stevens, J. A., Swinyard, B. M., Trichas, M., Tourette, T., Triou, H., Tseng, S., Tucker, C., Turner, A., Vaccari, M., Valtchanov, I., Vigroux, L., Virique, E., Voellmer, G., Walker, H., Ward, R., Waskett, T., Weilert, M., Wesson, R., White, G. J., Whitehouse, N., Wilson, C. D., Winter, B., Woodcraft, A. L., Wright, G. S., Xu, C. K., Zavagno, A., Zemcov, M., Zhang, L., & Zonca, E. 2010, *A&A*, 518, L3

Harris, A. I., Stutzki, J., Graf, U. U., Russell, A. P. G., Genzel, R., & Hills, R. E. 1991, *ApJ*, 382, L75

Herschel, W. 1785, Royal Society of London Philosophical Transactions Series I, 75, 213

Hibbard, J. E. 1997, in American Institute of Physics Conference Series, Vol. 393, American Institute of Physics Conference Series, ed. S. S. Holt & L. G. Mundy, 259–270

Joseph, R. D. & Wright, G. S. 1985, MNRAS, 214, 87

Kennicutt, Jr., R. C. 1998, ApJ, 498, 541

Larson, R. B. & Tinsley, B. M. 1978, ApJ, 219, 46

Lee, J. C., Gil de Paz, A., Tremonti, C., Kennicutt, Jr., R. C., Salim, S., Bothwell, M., Calzetti, D., Dalcanton, J., Dale, D., Engelbracht, C., Funes, S. J. J. G., Johnson, B., Sakai, S., Skillman, E., van Zee, L., Walter, F., & Weisz, D. 2009, ApJ, 706, 599

Leroy, A. K., Walter, F., Brinks, E., Bigiel, F., de Blok, W. J. G., Madore, B., & Thornley, M. D. 2008, AJ, 136, 2782

Maloney, P. R. 1999, Ap&SS, 266, 207

Maloney, P. R., Hollenbach, D. J., & Tielens, A. G. G. M. 1996, ApJ, 466, 561

Mao, R. Q., Henkel, C., Schulz, A., Zielinsky, M., Mauersberger, R., Störzer, H., Wilson, T. L., & Gensheimer, P. 2000a, A&A, 358, 433

—. 2000b, A&A, 358, 433

Meijerink, R., Spaans, M., & Israel, F. P. 2007, A&A, 461, 793

Meurer, G. R. 2000, in *Astronomical Society of the Pacific Conference Series*,
Vol. 211, *Massive Stellar Clusters*, ed. A. Lançon & C. M. Boily, 81–+

Mirabel, I. F., Vigroux, L., Charmandaris, V., Sauvage, M., Gallais, P., Tran,
D., Cesarsky, C., Madden, S. C., & Duc, P.-A. 1998, *A&A*, 333, L1

Mooney, T. J. & Solomon, P. M. 1988, *ApJ*, 334, L51

Mould, J. R., Huchra, J. P., Freedman, W. L., Kennicutt, Jr., R. C., Ferrarese,
L., Ford, H. C., Gibson, B. K., Graham, J. A., Hughes, S. M. G., Illingworth,
G. D., Kelson, D. D., Macri, L. M., Madore, B. F., Sakai, S., Sebo, K. M.,
Silbermann, N. A., & Stetson, P. B. 2000, *ApJ*, 529, 786

Naylor, B. J., Bradford, C. M., Aguirre, J. E., Bock, J. J., Earle, L., Glenn, J.,
Inami, H., Kamenetzky, J., Maloney, P. R., Matsuhara, H., Nguyen, H. T.,
& Zmuidzinas, J. 2010a, *ApJ*, 722, 668

Naylor, D. A., Baluteau, J.-P., Barlow, M. J., Benielli, D., Ferlet, M., Fulton,
T. R., Griffin, M. J., Grundy, T., Imhof, P., Jones, S., King, K., Leeks, S. J.,
Lim, T. L., Lu, N., Makiwa, G., Polehampton, E. T., Savini, G., Sidher,
S. D., Spencer, L. D., Surace, C., Swinyard, B. M., & Wesson, R. 2010b, in
Presented at the Society of Photo-Optical Instrumentation Engineers (SPIE)
Conference, Vol. 7731, *Society of Photo-Optical Instrumentation Engineers*
(SPIE) Conference Series

Neff, S. G. & Ulvestad, J. S. 2000, *AJ*, 120, 670

Nikola, T., Genzel, R., Herrmann, F., Madden, S. C., Poglitsch, A., Geis, N.,
Townes, C. H., & Stacey, G. J. 1998, *ApJ*, 504, 749

Panuzzo, P., Rangwala, N., Rykala, A., Isaak, K. G., Glenn, J., Wilson, C. D., Auld, R., Baes, M., Barlow, M. J., Bendo, G. J., Bock, J. J., Boselli, A., Bradford, M., Buat, V., Castro-Rodríguez, N., Chaniel, P., Charlot, S., Ciesla, L., Clements, D. L., Cooray, A., Cormier, D., Cortese, L., Davies, J. I., Dwek, E., Eales, S. A., Elbaz, D., Fulton, T., Galametz, M., Galliano, F., Gear, W. K., Gomez, H. L., Griffin, M., Hony, S., Levenson, L. R., Lu, N., Madden, S., O'Halloran, B., Okumura, K., Oliver, S., Page, M. J., Papageorgiou, A., Parkin, T. J., Pérez-Fournon, I., Pohlen, M., Polehampton, E. T., Rigby, E. E., Roussel, H., Sacchi, N., Sauvage, M., Schulz, B., Schirm, M. R. P., Smith, M. W. L., Spinoglio, L., Stevens, J. A., Srinivasan, S., Symeonidis, M., Swinyard, B., Trichas, M., Vaccari, M., Vigroux, L., Wozniak, H., Wright, G. S., & Zeilinger, W. W. 2010, *A&A*, 518, L37

Papadopoulos, P. P. 2007, *ApJ*, 656, 792

Papadopoulos, P. P., Thi, W.-F., & Viti, S. 2004, *MNRAS*, 351, 147

Papadopoulos, P. P., van der Werf, P., Isaak, K., & Xilouris, E. M. 2010, *ApJ*, 715, 775

Perrine, C. D. 1922, *MNRAS*, 82, 486

Petitpas, G., Iono, D., Peck, A., Wilson, C., Matsushita, S., Sakamoto, K., Wang, J., Ho, P., Zhang, Q., Rots, A., Wang, Z., Yun, M., & Surace, J. 2007, in *Astronomical Society of the Pacific Conference Series*, Vol. 375, *From Z-Machines to ALMA: (Sub)Millimeter Spectroscopy of Galaxies*, ed. A. J. Baker, J. Glenn, A. I. Harris, J. G. Mangum, & M. S. Yun , 267–+

Pilbratt, G. L., Riedinger, J. R., Passvogel, T., Crone, G., Doyle, D., Gageur, U., Heras, A. M., Jewell, C., Metcalfe, L., Ott, S., & Schmidt, M. 2010, A&A, 518, L1

Poglitsch, A., Waelkens, C., Geis, N., Feuchtgruber, H., Vandenbussche, B., Rodriguez, L., Krause, O., Renotte, E., van Hoof, C., Saraceno, P., Cepa, J., Kerschbaum, F., Agnèse, P., Ali, B., Altieri, B., Andreani, P., Augueres, J.-L., Balog, Z., Barl, L., Bauer, O. H., Belbachir, N., Benedettini, M., Billot, N., Boulade, O., Bischof, H., Blommaert, J., Callut, E., Cara, C., Cerulli, R., Cesarsky, D., Contursi, A., Creten, Y., De Meester, W., Doublier, V., Doumayrou, E., Duband, L., Exter, K., Genzel, R., Gillis, J.-M., Grözinger, U., Henning, T., Herreros, J., Huygen, R., Inguscio, M., Jakob, G., Jamar, C., Jean, C., de Jong, J., Katterloher, R., Kiss, C., Klaas, U., Lemke, D., Lutz, D., Madden, S., Marquet, B., Martignac, J., Mazy, A., Merken, P., Montfort, F., Morbidelli, L., Müller, T., Nielbock, M., Okumura, K., Orfei, R., Ottensamer, R., Pezzuto, S., Popesso, P., Putzeys, J., Regibo, S., Reveret, V., Royer, P., Sauvage, M., Schreiber, J., Stegmaier, J., Schmitt, D., Schubert, J., Sturm, E., Thiel, M., Tofani, G., Vavrek, R., Wetzstein, M., Wieprecht, E., & Wiezorrek, E. 2010, A&A, 518, L2

Rangwala, N., Maloney, P. R., Glenn, J., Wilson, C. D., Rykala, A., Isaak, K., Baes, M., Bendo, G. J., Boselli, A., Bradford, C. M., Clements, D. L., Cooray, A., Fulton, T., Imhof, P., Kamenetzky, J., Madden, S. C., Mentuch, E., Sacchi, N., Sauvage, M., Schirm, M. R. P., Smith, M. W. L., Spinoglio, L., & Wolfire, M. 2011, ArXiv e-prints

Sanders, D. B. & Mirabel, I. F. 1996, ARA&A, 34, 749

- Schulz, A., Güsten, R., Köster, B., & Krause, D. 2001, *A&A*, 371, 25
- Schulz, A., Henkel, C., Muders, D., Mao, R. Q., Röllig, M., & Mauersberger, R. 2007, *A&A*, 466, 467
- Solomon, P. M., Downes, D., & Radford, S. J. E. 1992, *ApJ*, 387, L55
- Solomon, P. M., Sanders, D. B., & Scoville, N. Z. 1979, in *IAU Symposium*, Vol. 84, *The Large-Scale Characteristics of the Galaxy*, ed. W. B. Burton, 35–52
- Stanford, S. A., Sargent, A. I., Sanders, D. B., & Scoville, N. Z. 1990, *ApJ*, 349, 492
- Steinmetz, M. & Navarro, J. F. 2002, *New A*, 7, 155
- Swinyard, B. M., Ade, P., Baluteau, J.-P., Aussel, H., Barlow, M. J., Bendo, G. J., Benielli, D., Bock, J., Brisbin, D., Conley, A., Conversi, L., Dowell, A., Dowell, D., Ferlet, M., Fulton, T., Glenn, J., Glauser, A., Griffin, D., Griffin, M., Guest, S., Imhof, P., Isaak, K., Jones, S., King, K., Leeks, S., Levenson, L., Lim, T. L., Lu, N., Makiwa, G., Naylor, D., Nguyen, H., Oliver, S., Panuzzo, P., Papageorgiou, A., Pearson, C., Pohlen, M., Polehampton, E., Pouliquen, D., Rigopoulou, D., Ronayette, S., Roussel, H., Rykala, A., Savini, G., Schulz, B., Schwartz, A., Shupe, D., Sibthorpe, B., Sidher, S., Smith, A. J., Spencer, L., Trichas, M., Triou, H., Valtchanov, I., Wesson, R., Woodcraft, A., Xu, C. K., Zemcov, M., & Zhang, L. 2010, *A&A*, 518, L4
- Tielens, A. G. G. M. & Hollenbach, D. 1985, *ApJ*, 291, 722

Toomre, A. & Toomre, J. 1972, ApJ, 178, 623

van der Tak, F. F. S., Black, J. H., Schöier, F. L., Jansen, D. J., & van Dishoeck, E. F. 2007, A&A, 468, 627

van der Werf, P. P. & Spaans, M. 2009, in The Next-Generation Infrared Space Mission: SPICA, ed. A. M. Heras, B. M. Swinyard, K. G. Isaak, & J. R. Goicoechea , 3009–+

Ward, J. S., Zmuidzinas, J., Harris, A. I., & Isaak, K. G. 2003, ApJ, 587, 171

Whitmore, B. C. & Schweizer, F. 1995, AJ, 109, 960

Whitmore, B. C., Zhang, Q., Leitherer, C., Fall, S. M., Schweizer, F., & Miller, B. W. 1999, AJ, 118, 1551

Wilson, C. D., Scoville, N., Madden, S. C., & Charmandaris, V. 2000, ApJ, 542, 120

—. 2003, ApJ, 599, 1049

Wilson, C. D., Warren, B. E., Israel, F. P., Serjeant, S., Bendo, G., Brinks, E., Clements, D., Courteau, S., Irwin, J., Knapen, J. H., Leech, J., Matthews, H. E., Mühle, S., Mortier, A. M. J., Petitpas, G., Sinukoff, E., Spekkens, K., Tan, B. K., Tilanus, R. P. J., Usero, A., van der Werf, P., Wiegert, T., & Zhu, M. 2009, ApJ, 693, 1736

Wolfire, M. G. 2010, Ap&SS, 380

Young, J. S. & Scoville, N. Z. 1991, ARA&A, 29, 581

Zhang, H.-X., Gao, Y., & Kong, X. 2010, MNRAS, 401, 1839

M.Sc. Thesis — Maximilien R. P. Schirm — McMaster University - Physics and Astronomy — 2011

Zhu, M., Seaquist, E. R., & Kuno, N. 2003, ApJ, 588, 243